Microscopie et spectroscopie à effet tunnel sur des complexes métallo-organiques : des atomes isolés aux réseaux étendus

Kezilebieke Shawulienu

UNIVERSITÉ DE STRASBOURG

ÉCOLE DOCTORAL PHYSIQUE ET CHIMIE PHYSIQUE

THÈSE présentée par :

Kezilebieke SHAWULIENU

pour obtenir le grade de : **Docteur de l'université de Strasbourg**

Discipline/ Spécialité : Nanophysique

Scanning tunneling microscopy and spectroscopy of metal-organic complexes: from single atoms to extended networks

Soutenue le 24 janvier 2014 devant la commission d'examen :

Prof. Jean-Pierre Bucher	**Directeur de thèse**
Prof. Johannes Barth	**Rapporteur externe**
Dr. Xavier Bouju	**Rapporteur externe**
Dr. Jean Weiss	**Examinateur interne**

Institut de Physique et Chimie des Matériaux de Strasbourg, UMR 7504, France

This thesis is dedicated to
my lovely wife Nurjay
for her infinite love and support

Acknowledgements

I would like to thank my advisor Professor Jean-Pierre Bucher, for giving me the opportunity to perform this challenging research in his group from the Department of Organic Materials of IPCMS and his guidance and support during this work. It has been a great learning experience for me and I really appreciate his valuable advice and guidance.

I want to thank the members of the our group. Special thanks go to Anis Amokrane for his help, not only the scientific discussions but also being a friend and a support during the last two years of my stay in Strasbourg. I will take this opportunity to acknowledge Dr. Mauro Boero for the DFT calculations presented in this thesis. I want to acknowledge Prof. Mathieu Abel for his kind discussion and for exchanging his results and ideals. Special thanks for Nicola for the technical support.

Finally, I would like to thank my parents and my wife for their confidence and support through the difficult times.

Abstract

In the bottom up approach of todays nanoscience, the supramolecular assembly of metal atoms and molecules on surfaces is leading to functional compounds, relevant to many applications in optoelectronics, magnetism, and catalysis. It has been found that in some cases high magnetic spin states and strong magnetic anisotropy appear as a result of electron transfer between ligands, surface and metal atom. The focus of this thesis lies on the self assembling of 1,2,4,5-Tetracyanobenzene (TCNB) and Fe-TCNB coordination nanostructures on the Au(111) surface. The structural formation is directed by the non covalent interactions. Scanning tunneling spectroscopy (STS) reveal that the TCNB molecules are physisorbed on Au(111) surface. By detail analysis of the dI/dV spectra above the TCNB monolayer on the Au(111) surface, we found that the TCNB molecules on Au(111) shows a negligible charge transfer with Au(111) substrate and a small adsorption energy of 0.5 eV per TCNB molecules. STS measurement provide a HOMO−LUMO gap of 3 eV in agreement with DFT calculations. By controling the fabrication parameters, surface coordination nanostructures with different chemical composition or molecular packing have been synthesised. The electronic properties have been characterized by the local dI/dV analysis of the metal centers at different steps of a Fe-$(TCNB)_x$ (x=4, 2) complexes formation. At low temperature deposition, first form an ordered metastable intermediate. STM data yield the bond angle between the Fe-N-C is 120°. The scanning tunneling spectroscopy reveal that Fe atoms and the TCNB molecules keep their identity while the Fe atoms localize the surface-state electrons similar to what they do on the bare Au(111) surface. This result indicates that the TCNB molecules are virtually in the same electronic state as before the Fe adsorption. The situations are different when the deposition performance at room temperature. When the temperature is changed, to room temperature, the original entities transform into the $Fe(TCNB)_4$ monomer complexes with 180° Fe-N-C bond angles. The

STS above the $Fe(TCNB)_4$ complex strongly suggest that the coordination bond had been formed between the Fe atom and the TCNB ligands. DFT calculations support the conclusions and drawn from experimental studies and assist the interpretations of experiment. Further structural complexation is achieved by the synthesis of $Fe(TCNB)_2$ network. The network has a square structure with a regular seperations of the magnetic Fe atoms in the network. The electronic information is gathered from the spectroscopic labeling of FePc to identify some of the resonances of the $Fe(TCNB)_2$ network. There are similar features are found in the dI/dV spectra above the Fe atoms and ligand in both system, indicating that the Fe somehow feels a similar environment from the TCNB ligands in the network and in the FePc molecules. Further analysis of this feature have been disused by means of metal-ligand bond formation.

Keywords: Scanning tunneling microscopy, Scanning tunneling spectroscopy, chirality, reactions at surfaces, TCNB, metal-organic coordination, self-assembly, metastable intermediate

Résumé

La recherche actuelle dans le domaine des nanosciences, l'assemblage supra moléculaire d'atomes métalliques et de molécules sur des surfaces ouvre la voie à des composants fonctionnels, utiles dans une multitude d'applications comme l'Optoélectronique, le magnétisme et la catalyse. Il a été démontré que dans certains cas, l'état de Spin Haut et une forte anisotropie magnétique apparaissent suite à un transfert d'électron entre ligands, surface et atomemé tallique. Le but de cette thése porte sur l'auto-assemblage des 1,2,4,5-tetracyanobenzène (TCNB) et des coordinations nanostructurelles des Fe-TCNB sur une surface d'Au(111). La formation de ces structures est conduite par les interactions non-covalentes. La spectroscopie à effet tunnel (STS) révèle que la molécule de TCNB est physisorbée sur la surface d'Au(111). Une analyse détaillée des spectres dI/dV effectués sur une monocouche de TCNB sur une surface d'Au(111) montre que la molcule de TCNB a un transfert de charge ngligeable sur ce substrat avec une énergie d'adsorption de 0,5 eV par molécule. Les mesures STS révélent un gap HOMO-LUMO de 3 eV, comme le prédit la théorie. En contrôlant les paramétres de fabrication, des composants nanostructurels avec différentes compositions chimiques ou des arrangements moléculaires ont été synthétisés. Les propriétés électroniques ont été caractérisées par une analyse spectroscopique dI/dV locale sur les centres métalliques à différentes étapes de formation des complexes Fe-$(TCNB)_x$ (x=4, 2).

La déposition à trés basse température forme un état intermédiaire métastable. Les données STM montrent que l'angle que forment le triédre Fe-N-C est de 120 °. La spectroscopie tunnel révèle que le Fe et la molécule de TCNB gardent leur identité spectroscopique, le Fe garde ses états de surface de la même faon que s'il avait été déposé seul sur une surface d'Au(111). Ceci indique que les molécules de TCNB sont virtuellement dans le même état électronique qu'avant la déposition du Fe.
La situation change lorsque ce dépôt est effectué à température ambiante.

Une augmentation de température agit sur l'interaction des composants transformant ainsi la formation en un complexe monomère de $Fe(TCNB)_4$ avec un angle Fe-N-C de 180°. La spectroscopie STS sur ce complexe suggère fortement que la liaison de coordination est formée entre le Fe et la molécule de TCNB.

Les calculs DFT soutiennent ces conclusions. Plus loin, une structure a été réalisée par la synthèse d'un réseau $Fe(TCNB)_2$. Ce réseau a une structure carrée avec une séparation régulière entre les atomes de Fe. Les informations électroniques de la structure sont données par la molécule de FePc (où Pc représente la molécule de Phthalocyanine) pour identifier les pics de résonnance du spectre du réseau de $Fe(TCNB)_2$. Une similitude apparait dans les spectres dI/dV effectués sur l'atome de Fe et sur les ligands dans les deux systèmes, indiquant que le Fe ressent un environnement similaire quand il est entouré de TCNB ou quand il est à l'intérieur d'une Phthalocyanine. Une analyse plus détaillée basée sur la formation des liaisons métal-ligands a été discutée.

Mot-clè: Microscopie à effet tunnel, Spectroscopie à effet tunnel, chiralité, Les réactions au niveau des surfaces, TCNB, metal-organic coordination, auto-assemblage, métastable intermédiaire

Résumé étendu

Durant les dernières décennies, les progrès en technologie de l'information et de l'enregistrement on conduit à une réduction considérable de la taille des composants électroniques répondant ainsi à une demande croissante en matière de capacités de stockage et de puissance de calcul. La densitè de stockage des disques durs modernes augmente constamment conduisant à des bits individuels de plus en plus petits, la limite ultime étant déterminée par la stabilité thermique des grains magnétiques. Si les grains sont trop petits, leur aimantation devient thermiquement instable et n'est plus apte à stocker l'information de manière fiable. La taille des transistors dans les circuits intégrés modernes est de l'ordre de 20 nm [27] et continue à décroître. L'industrie des semi-conducteurs utilise des méthodes top-down, qui permettent une fabrication en parallèle à grande échelle des dispositifs. Les méthodes sont celles de la lithographie et les tailles sont donc limitées par la longueur d'onde de la lumière. De gros efforts sont faits actuellement pour développer de nouvelles méthodes de fabrication, elles consistent par exemple à diminuer la longueur d'onde des sources de lumière [57]. Par ailleurs en diminuant la taille des dispositifs, de nouveau effets entre en jeu, tels que des effets quantiques qui dominent alors les propriétés des matériaux et ainsi fixent une limite inférieure à la miniaturisation.

L'introduction de nouveaux matériaux et de nouveau concepts peut aider à surmonter les difficultés décrites plus haut. Comme l'a remarqué R. Feynmann [31], le contrôle de la matière à l'échelle atomique peut conduire à des dispositifs basés sur les effets quantiques, ouvrant la voie à toute une série de nouveau dispositifs. Feynmann envisageait déjà d'utiliser des atomes et des molécules comme unités élémentaires dans des dispositifs électroniques. Les molécules sont petites et la synthèse moléculaire offre alors des possibilités quasi infinies de géométries et de groupes fonctionnels. En fait le transistor à un atome [34] ou à une molécule [108] a déjà été démontré mais beaucoup de chemin reste à parcourir pour arriver à

une réalisation industrielle. Dans cet optique, la croissance de matériaux moléculaires sur des surfaces reste un point clé. Alors que la fabrication contrôlée de nanostructures avec une précision atomique par une approche top-down est difficile à réaliser, l'approche bottom-up présente de nombreux avantages. De nos jours, des techniques de fabrication et de caractérisation puissantes ont été développées, qui permettent d'imager et de manipuler des atomes et des molécules au moyen d'un microscope à effet tunnel ou d'un microscope à force atomique. Le progrès rapide de ces techniques permet aujourd'hui la création de structures atome par atome ou molécule par molécule. La technique reste néanmoins longue et inappropriée pour la fabrication à large échelle. Le processus d'assemblage d'atomes météalliques combinés à des ligands organiques est une approche prometteuse pour le design de nanostructures et permet la croissance de réseaux ordonnés et sans défauts avec des structures et des tailles ajustables [8]. En général, le design de la structure moléculaire est basé sur des interactions non-covalentes avec des liaisons et des géométries spécifiques permettant l'organisation de briques élémentaire. Une classe de matériaux particulièrement intéressante est basée sur la combinaison de métaux de transition et de molécules. Les liaisons métal-ligand sont caractérisées par leurs directionalité [110, 8]. Les complexes de coordinations métalliques et les réseaux sont d'un grand intérêt à cause de la charge et du spin portés par le centre métallique [1, 25, 35]. Les sondes à balayage ont permis une meilleure compréhension des processus chimiques élémentaires en jeu lorsque différentes espèces adsorbées sur une surface réagissent entre elles. Dans cette thèse, on présente une analyse d'un système constitué d'un accepteur 1,2,4,5- tetracyanobenzène (TCNB) et d'un atome de Fe. Ce système est étudié sur une surface métallique par microscopie/spectroscopie à effet tunnel (STM/STS). L'analyse structurale et électronique a été effectuée à basse température. La résolution spatiale élevée du STM combinée avec les mesures de spectroscopie (STS) en fait un outil idéal pour l'étude de systèmes moléculaires sur des surfaces. La thése est organisée de la manière suivante :

Le chapitre 1 donne une introduction générale du processus d'auto-assemblage qui est basé sur un nombre important d'interactions différentes. Ces interactions peuvent être classées en interaction hydrogène, Van der Walls, donneur-accepteur, métal-ligand et covalente. La structure résultante

peut dépendre d'une compétition entre toutes ces interactions. L'utilisation de systèmes hétérogènes consistant en deux espèces (organic/inorganic ou organique/organique) peut alors conduire à des situations complexes. Néanmoins, l'utilisation de constituants avec des propriétés complémentaires peut tourner cette complexité en un avantage. Par exemple, le fait de combiner des espèces moléculaires et métalliques avec différentes propriétés chimiques, en particulier d'énergie d'ionisation et d'affinité chimique, peut conduire à des processus de transfert de charge et à une redistribution de celle-ci. La localisation des charges joue alors un rôle déterminant sur la conductivité [29], le magnétisme organique [28] et la supraconductivitè [19] de tels systèmes. Quelques exemples des ces concepts sont présentés dans ce chapitre.

Le chapitre 2 donne une description détaillée du STM utilisé pour la caractérisation des propriétés électroniques de molécules individuelles et des complexes organo-métalliques sur des surfaces métalliques. Le STM de CreaTech (Berlin) fonctionne à 4.5 K, sous ultravide. En plus de l'imagerie, le STM peut aussi être utilisé pour des mesures de spectroscopie, par exemple afin de déterminer la densité d'état d'un adsorbat de manière locale. Le contexte théorique de la STS ainsi que la réalisation expérimentale de l'acquisition des données sont présentés dans ce chapitre. Les méthodes de préparation des l'échantillons et des pointes sont également présentées. Un exemple de STS est donné afin d'introduire la notion de cartographie de dI/dV. Une introduction sur l'origine de l'état de surface des métaux nobles et sur la localisation des électrons par des impuretés atomiques est également donnée. A la fin du chapitre les dispositifs d'évaporation fabriqués par l'équipe sont brièvement décrits.

Dans le chapitre 3 on décrit l'auto-assemblage de la molécule de 1,2,4,5-Tetracyanobenzène (TCNB) sur la surface de Au(111). L'ensemble des caractéristiques, de la structure cristallographique aux propriété électroniques du TCNB sur la surface de l'Au(111) ont été étudiées par STM/STS. L'analyse détaillée par spectroscopie dI/dV de la monocouche de TCNB sur l'Au(111) montre que le TCNB se trouve dans un état faiblement physisorbé dans lequel la molécule reste neutre et où la structure auto-assemblée est stabilisée par la formation de liaisons hydrogène CN−−H-C. De plus, la molécule de TCNB sur Au(111) montre un transfert de

charge négligeable avec le substrat et une énergie d'adsorption de 0.50 eV par molécule de TCNB. Les mesures de STS donnent un gap HOMO-LUMO de 3 eV en accord avec les calculs de DFT. Ces mesures montrent également que le diplacement de l'état de surface pourrait être dû à un changement du travail de sortie et/ou à un changement du potentiel image. Le caractère accepteur du TCNB semble donc conservé malgré un transfert de charge négligeable de 0.06 e. Le TCNB peut donc se charger suite à une co-adsorption avec un ion métallique qui possède un caractère donneur. Pour toutes ces raisons, le TCNB est un systéme modèle pour l'étude de la liaison de coordination métal-organique sur Au(111).

Le chapitre 4 est dédié à la formation des complexes de coordination Fe-TCNB sur la surface de Au(111). Un soin particulier a été apporté à l'analyse de la structure électronique du centre métallique à différentes étapes de la formation du complexe. A température de dépôt relativement basse, une structure intermédiaire de Fe-$(TCNB)_4$ apparaît sous forme de domaines qui sont enchâssés dans une phase mère de TCNB et doivent s'adapter à des conditions aux bords strictes. A l'intérieur d'un tel domaine de confinement, des unités adjacentes de Fe-$(TCNB)_4$ possèdent la même chiralité, bien que des domaines droite et gauche soient présents dans la même proportion sur la surface. La distance N-Fe est estimée à 2.0 Å à partir des images de STM et l'angle entre les liaisons Fe-N-C est de environ 120°. La spectroscopie tunnel révèle que les molécules de TCNB conservent leur identité alors que les atomes de Fe localisent les électrons de l'état de surface d'une manière semblable à celle observée sur une surface native de Au(111). Le résultat indique que les molécules de TCNB sont dans le même état électronique qu'avant l'adsorption des atomes de Fe. Dans cet exemple, le Fe et le TCNB survivent à une densité surfacique supérieure à celle de la monocouche moléculaire de TCNB sans former de liaison de coordination. On montre que la structure de coordination carré plan du monomère de Fe-$(TCNB)_4$ ne peut pas se développer en prsence de contraintes latérales dues au confinement induit par la croissance. Cette situation change lorsque le dépôt est effectuè à température ambiante. Les entités précédentes se transforment alors en des monomères de $Fe(TCNB)_4$ avec une liaison de coordination de 1.8 Å et un angle entre Fe-N-C de 180°. Les spectres dI/dV au dessus des complexes de $Fe(TCNB)_4$ montrent de nouvelle structures : le gap HOMO-

LUMO est considérablement réduit et passe de 3.0 eV, dans le système précurseur, à 2.0 eV dans le monomère de $Fe(TCNB)_4$. De plus, la signature la plus marquante de la formation du complexe est l'apparition de nouvelles résonances à -0.5 eV et +0.7 eV. Ces deux structures se rapportent à des orbitales moléculaires d possédant une contribution hors du plan, celles mesurées préférentiellement par STM. Des calculs par DFT viennent confirmer les études expérimentales. L'analyse de la redistribution de charges après relaxation dynamique des complexes libres apporte des informations supplémentaires. La coordination d'ordre quatre avec les ligands de TCNB conduit à un transfert de -2 $|e|$ de l'atome de Fe vers les azotes premiers voisins et à une redistribution de charge sur les ligands de TCNB. De ce fait, le Fe devient Fe^{2+}. Ceci est confirmé par une analyse comparative des différentes charges de Mulliken sur les N proches voisins des sites de Fe ; on observe un transfert de -0.28 $|e|$ vers chaque atome d'azote.

Le chapitre 5 est dédié à la formation du réseaux de $Fe(TCNB)_2$ complètement réticulés composés d'atomes de Fe interconnectés par des molécules de TCNB. Le nouveau réseau posède une structure carrée avec une périodicité bien définie des atomes magnétiques de Fe et se distingue clairement d'un assemblage de monomères de $Fe(TCNB)_4$. La formation du réseau est particulièrement sensible à la stoichiométrie. Un excès d'atomes métalliques ou de molécules peut empêcher la formation d'une structure ordonnée et conduire à des phases désordonnées et des défauts atomiques. La longueur de la liaison de coordination de F-N est de 1.8 Å telle que mesurée par STM et l'angle Fe-N-C est proche de 180° comme pour le monomère de $Fe(TCNB)_4$. L'information électronique sur le réseau de $Fe(TCNB)_2$ est obtenue en partie au moyen de l'indexation spectroscopique de la molécule de FePc (Fe-Phthalocyanine) sur Au(111). Des similarités apparaissent dans les dI/dV au dessus du Fe et des ligands de ces deux systèmes. Premièrement, la position du pic dxz/yz à -0.79 V indique que dans les deux systèmes le Fe ressent un environnement similaire de la part des ligands de TCNB dans le réseau et dans la molécule de FePc. L'analyse du mécanisme de formation de la liaison métal-ligand montre que l'apparition de la résonance à -0.79 V est due à la formation d'une liaison métal-ligand commune entre l'orbitale d de l'atome et celle du ligand. Néanmoins, la

molécule de FePc est plus compliquée puisque deux types de liaisons (covalentes et de coordination), existent dans la même molécule. En particulier, le pic dxz/yz, similaire pour les deux systèmes, est une conséquence directe de la liaison de coordination entre les paires d'électrons non partagés dans les deux atomes d'azote de l'isoindole et l'atome de Fe de FePc. Au contraire, l'apparition de l'orbitale dz^2 sur le FePc et non sur le réseau de $Fe(TCNB)_2$ est un résultat de la liaison covalente dans le FePc.

Le chapitre 6 résume les résultats de cette thèse et présente quelques directions de recherches futures.

Contents

1 Context and Motivation **3**

1.1 Introduction 3

1.2 Creating molecular networks using molecular self-assembly 4

1.2.1 Molecule-molecule interactions 6

1.2.2 Molecule-substrate interaction 9

1.3 Tuneable metal−organic coordination networks 11

1.4 Two-dimensional high-spin Fe arrays formed on metal interface 13

1.5 Metal-organic coordination networks on Au(111) with strong acceptor molecules 16

2 Scanning tunneling microscopy and related techniques **19**

2.1 Experimental setup 19

2.1.1 STM in the ultra-high vacuum 19

2.1.2 Cryostat 20

2.1.3 Vacuum chambers 21

2.1.4 Electronics 24

2.1.5 Digital signal processor (DSP) 24

2.1.6 Pre-amplifier 26

2.1.7 High voltage amplifier 26

2.1.8 Principle of scanning tunneling microscope 27

2.1.9 Theoretical background of STM 29

2.1.10 Scanning tunneling spectroscopy 30

2.2 Sample and tip preparation 34

2.2.1 An example of STM and STS 34

2.3 The origin of Shockley surface states 37

2.4 Surface-State Localization by single adatoms 39

2.5 Evaporation techniques 41

2.5.1 Molecular Evaporator 41

2.5.2 Metal Evaporation 43

3 The adsorption structure and electronic properties of 1,2,4,5-Tetracyanobenzene (TCNB) on Au(111) 47

3.1 Introduction 47
3.2 Self-assembling of acceptor TCNB molecules on Au(111) 48
3.3 Conclusions 52

4 Steric and electronic selectivity in the formation of Fe-TCNB complexes on Au(111): from geometric confinement to bond formation 55

4.1 Introduction 55
4.2 Early stage of $Fe(TCNB)_4$ formation on Au(111) 56
4.3 The formation of $Fe(TCNB)_4$ coordination structures on Au(111) at room temperature 60
4.4 Conclusions 68

5 The formation of 2D $Fe(TCNB)_2$ coordination network and comparison with Iron-Phthalocyanine molecule 71

5.1 Two-dimensional Fe-TCNB coordination network on Au(111) 71
5.2 Study of adsorption of single iron phthalocyanine on Au(111) 75
5.3 Spectroscopic identification of the $Fe(TCNB)_2$ coordination network on Au(111) 84
5.4 Conclusions 89

6 Summary and perspectives 91

Bibliography 95

List of Figures

1.1 Supra-molecular self-assembly process on a surface: a molecular beam is directed onto a solid substrate 5
1.2 Crystal field splitting diagrams for the octahedral and Square planar complexes 9
1.3 STM topographic image of the metal−organic network formed by NC−Ph−CN linkers with different length 11
1.4 Tunable 2D window like network composed of Fe-atoms, pyridine and carboxylic acid ligands 12
1.5 Planar supra molecular layers of FeTPA complexes self-assembled on Cu(100) 13
1.6 Circularly polarized X-ray absorption spectra of Fe/Cu(100)(a), $Fe(TPA)_4$(b), and $O_2Fe(TPA)_4$(c) and corresponding element-selective magnetization curves of the Fe centers $Fe(TPA)_4$(d) and $O_2Fe(TPA)_4$(e)respectively (from ref [35]). 14
1.7 STM topographic image of of MnTCNQ networks on Au(111) 15

2.1 A Schematic drawing of the Besocke beetle type STM 20
2.2 Picture of the STM inside the cryostat 21
2.3 Schematic of the cryostat 22
2.4 Perspective view of the UHV system with its components 23
2.5 The main electronics of the LT-STM 25
2.6 The principle of a local probe 28
2.7 Snapshot of control the exact position of the tip with the help of a camera . . . 28
2.8 1D Quantum tunneling of electrons 30
2.9 The working principle of STS with different modes 32
2.10 The STM topographic image of reconstructed Au(111) surface 35
2.11 Surface state detection by STS 36
2.12 Nanostructure fabrication on metal surface by STM 37
2.13 the Shockley surface states of the Cu(111) and Au(111) surface . . . 38
2.14 Surface-State Localization by single adatoms 40

2.15 Our home built molecular evaporator 42
2.16 The temperature as function of the current intensity through the filament 42
2.17 STM topographic image of the monolayer of 2,2'-Bipyrimidine molecules on Au(111) recorded at 77 K 43
2.18 Metal evaporation on surface 44

3.1 The molecular structure of TCNB molecule. 48
3.2 STM topographic image of a self-assembled monolayer of TCNB on Au(111) surface 48
3.3 dI/dV spectra taken on clean Au(111) and TCNB monolayer 49
3.4 The model of density of states of a two-dimensional system (Au(111) surface) and metal/ organic interface 50
3.5 The gas phase DFT calculation of TCNB molecules 52

4.1 STM image of Fe-$(TCNB)_4$ confined phase on Au(111) surface 57
4.2 The formation of $Fe(TCNB)_4$ coordination structures on Au(111) at room temperature 61
4.3 Line profiles of the different $Fe(TCNB)_4$ phases 62
4.4 STS of $Fe(TCNB)_4$ complex with 180 Fe-N-C bond angle and for comparison the Fe-$(TCNB)_4$-unit in the metastable confined phase 63
4.5 Spin density of the $Fe(TCNB)_4$ 66
4.6 Spin-resolved PDOS of $(Fe(TCNB)_4$ 67
4.7 Qualitative molecular orbital diagram 68

5.1 STM image of the formation of $Fe(TCNB)_2$ network on Au(111) . . . 72
5.2 Two equivalent chiral domains of $Fe(TCNB)_2$ network on Au(111) . . 73
5.3 STS of $Fe(TCNB)_2$ network for both, on the Fe in the $Fe(TCNB)_2$ network and with same condition on the ligand (Feedback loop opened at V = -0.7 V, I = 0.2 nA). 73
5.4 The dI/dV spectra for both, on the Fe and ligand of the $Fe(TCNB)_2$ network. 74
5.5 The molecular structure of the metal phthalocyanine. 75
5.6 STM images (63 × 63 nm) of 0.2 ML FePc molecules on Au(111) surface 76
5.7 The relative frequencies of the FePc with three different adsorption configurations on Au(111). 76
5.8 STM topographic images of FePc on Au(111) (2.49 × 2.49 nm) at different biases, noted in the images. 77
5.9 The STS spectra of FePc on Au(111) surface 78

5.10 The constant height dI/dV maps over the FePc (2×2 nm^2). The feedback loop was opened over the Au(111) surface at 0.01 nA and the bias indicated in each map. . 79
5.11 The Kondo signature of two different adsorption of FePc on Au(111) surface 80
5.12 STM topographic images of FePc on Au(111) (a), Cu(111) (b) and Co nanoisland 81
5.13 The formation of a chemical bond in the interaction between an adsorbate state and the s and d band of a transition metal (from [85]). 82
5.14 The position of $d_z{}^2$ orbital of Fe is shifting towards the Fermi level as a function of d band center (the dashed line is a guide for the eyes). 84
5.15 The unit cell of the $Fe(TCNB)_2$ network 85
5.16 The comparison of dI/dV spectra taken on the network and on the FePc molecule on Au(111) surface 86

6.1 (a) STM image of full transformation of Fe-$(TCNB)_4$ monomer to the covalent bond octacyanophthalocyanine after annealing 300 °C. (b, c) high resolution images of octacyanophthalocyanine monomer and structural model. 93

List of Tables

1.1 Classification of basic interactions and processes, with associated energy (barrier) and typical distances relevant when functional molecular species are employed to engineer molecular architectures on metal substrates (from ref [8]). 6

3.1 Different acceptor Cyano families are physisorbed on Au(111) surface. 51

4.1 Equilibrium geometrical parameters, before (only TCNB molecule) and after the formation of the $Fe(TCNB)_4$ complex. 64

4.2 The Mulliken charge distribution and the valence of the main sites of the TCNB and $Fe(TCNB)_4$ complex. Before and after the formation of the coordination bound. The N is correspond to the nearest neighbor Nitrogen atoms of Fe in the complex. The C and C^1 are the nearest neighbor and next neighbor Carbon atoms of Fe atom in the complex 65

5.1 The position of d_{z^2} orbital of Fe in the FePc molecules of different metal surfaces. 82

5.2 The center of the d band is calculated for the most close-packed surface for each of the metals [(111) for fcc, (001) for hcp, and (110) for bcc] [53]. 83

5.3 A summary of all similar peak positions of the network and FePc on Au(111) surface. 87

Chapter 1

Context and Motivation

1.1 Introduction

The famous talk by Richard P. Feynman entitled "There's plenty of room at the bottom"-An invention to enter a new field of physics [32] in December 29th 1959 at the annual meeting of the American Physical Society at California Institute of Technology. In which he had vision to miniaturize machines and computers to atomic scale and to arrange the atoms the way we want. His speech can be considered as a starting point of "Nanotechnology". Nanoscale science and nanotechnology aim at controlling matter on the smallest length scale, then atoms and molecules can be used to build machines or electronic devices at the nanometer scale.
Molecular electronics, sometimes called moletronics, involves the study and application of molecular building blocks for the fabrication of electronic components. This includes both, bulk applications of conductive polymers as well as single-molecule electronic components for nanotechnology, which includes also devices based on ordered array of atoms, atomic chains or individual atoms [16]. By altering size, geometry, and chemistry it is possible to tailor functionalities in unprecedented ways [88].
Scanning tunneling microscopy and spectroscopy (STM/STS) has provided access to the physical properties of single molecules with a sub−molecular resolution. Meanwhile, it is possible to do spin sensitive measurement using spin polarized tips [13, 55]. Nowadays, one of the major challenges in the field of molecular electronics is to create new nano-devices that use the spin of a single molecules or molecular networks as an active element, the reason for that: **1**. The organic molecules are small and flexible typically a few nanometers in width. **2**. Their electronic and magnetic properties can be adjusted by coordination chemistry (the length of the linker and nature of the metal atom can be adjusted). **3**. They can form 2D networks or 1D metal organic

chains on the metal surfaces by self assembly. In particular, magnetic molecules consisting of an atomic center (transition metal atoms) surrounded by non covalently bonded organic ligands are of great interest. However, the realization of such devices requires additional understanding of: **1**. Adsorption geometry of the molecules on metal surfaces **2**. Interactions between molecules and with substrate in order to perceive self assembly **3**. bond nature between the ligands and metal atoms.

1.2 Creating molecular networks using molecular self-assembly

Molecule self-assembling is the spontaneous association of molecules under equilibrium conditions into stable, structurally well-defined aggregates joined by non-covalent bonds [125]. Molecular self-assembly is a key concept in supra molecular chemistry, since the assembling of the molecules is directed mainly through non covalent interactions (e.g., hydrogen bonding, metal coordination, van der Waals forces, $\pi - \pi$ interactions, and/or electrostatic interaction). Molecular self-assembly is also an important aspect of bottom-up approaches in nanotechnology. Self-assembly processes are one of the most promising methods to engineer complex molecular architectures on various substrates. Adsorption, mobility, and intra-or intermolecular interactions, all of which depend on the substrate crystalline lattice, chemical nature, and symmetry [7, 9] are key parameters that govern the formation of molecular architectures. A balancing of lateral molecular and surface interaction is at the origin of the formation of supra molecular order. The self-assembly process was described by Barth (Figure1.1)[8]. The principle of two dimensional supra molecular self-assembled structure formation is explained by a general molecular growth example.

Molecules are directed onto a clean substrate surface. The molecule in the given example is adsorbed (energy gain E_{ad}) on the surface at a specific site. The molecules migrate and rotate in two dimensions (thermally activated processes associated with energy barriers E_m and E_{rot}, respectively). From the point of view of thermodynamics, molecules on the surface try to assemble in order to achieve minimum free enthalpy. Non-covalent-bond formation between functional groups (energy gain E_{as}) allows molecules to adopt low-energy positions that govern the molecular suprastructure. In addition, the indirect substrate-mediated interactions (maximum energy cost E_s) also influence the molecular self-assembly process. The addition of all these processes leads to the self-assembly of molecules into complex molecular architectures

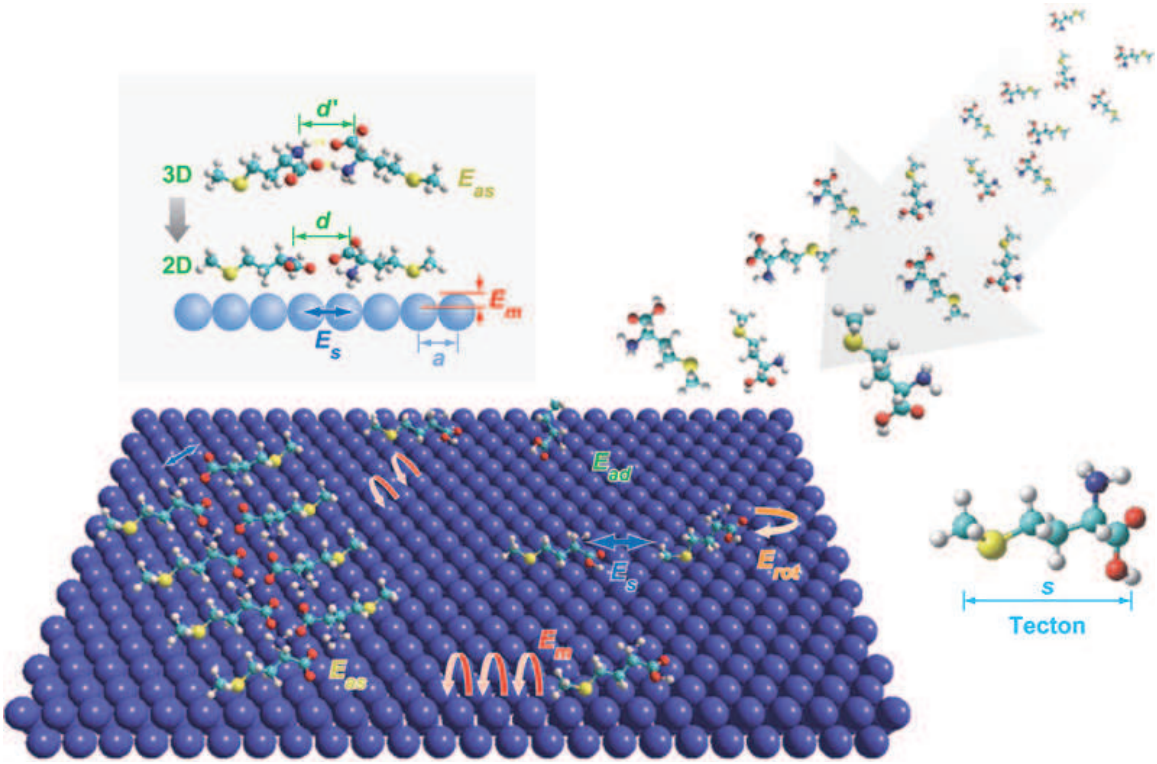

Figure 1.1: Supra-molecular self-assembly process on a surface: a molecular beam is directed onto a solid substrate. The adsorption (energy E_{ad}), thermal migration and rotational motions (barriers E_m and E_{rot}), and substrate-mediated and direct lateral interactions (energy E_s and E_{as}) are key parameters. A molecule (tecton) self-assembles into the twin chain on the surface. A scheme of how surface atoms (a is the lattice periodicity) can influence the supra molecular characteristics and the non-covalent-bond length d is shown in the inset (from ref [8]).

	Energy range	Distance	Character
Adsorption	$E_d \approx 0.510$ eV	$\approx$ 1-1.3 Å	Directional, selective
Surface migration	$E_m \approx 0.05$-3 eV	$\approx$ 2.5-4 Å	1D/2D
Rotational motion	$E_{rot} \approx \dim(E_m)$	S(molecule length)	2D
Indirect substrate mediated	$E_s \approx 0.001$-0.1 eV	a	Periodicity
Reconstruction mediated	$E_s \approx 1$ eV	short	Covalent
van derWaals	$E_{as} \approx 0.02$-0.1 eV	$< 1nm$	Non-selective
Hydrogen bonding	$E_{as} \approx 0.05$-0.7 eV	$\approx$ 1.5-3.5 Å	Selective, directional
Electrostatic ionic	$E_{as} \approx 0.05$-2.5 eV	Long range	Non-selective
Metal-ligand interactions	$E_{as} \approx 0.5$-2 eV	$\approx$ 1.5-2.5 Å	Selective, directional

Table 1.1: Classification of basic interactions and processes, with associated energy (barrier) and typical distances relevant when functional molecular species are employed to engineer molecular architectures on metal substrates (from ref [8]).

which are energetically stable. Table 1.1 gives an overview of the relevant process and interactions with associated energy ranges and interaction length.

To summarize, the key parameters to control the formation of complex supra molecular networks using self-assembly technique are the molecule-molecule interaction, molecule-substrate interaction, temperature, and molecular concentration ratio.

1.2.1 Molecule-molecule interactions

The weak intermolecular interactions responsible for molecular ordering in self-assembly includes hydrogen bonds, coordination bonds in ligands and complexes, ionic and dipolar interactions, van der Waals forces, and hydrophobic interactions.

- Van der Waals interaction

  The Van der Waals interaction is an attractive force between molecules (or between parts of the same molecule) that depends on the distance of the molecules. Van der Waals forces include attractions and repulsions between atoms, molecules, and surfaces, as well as other intermolecular forces. Van der Waals forces are relatively weak compared with other forces as shown in Table 1.1. The Van de Waals interaction has moderate specificity and directionality. It can exist between the substrate and the deposited molecules or between the molecules on the surfaces.

- Hydrogen bond

A hydrogen bond is the electromagnetic attractive interaction between polar molecules in which hydrogen (H) is bound to a highly electronegative atom, such as nitrogen (N), oxygen (O) or fluorine (F). These hydrogen-bond attractions can occur between molecules (intermolecular) or within different parts of a single molecule (intra-molecular). The most ubiquitous and perhaps simplest example of a hydrogen bond is found between water molecules. In a discrete water molecule, there are two hydrogen atoms and one oxygen atom. Two molecules of water can form a hydrogen bond between them; the simplest case, when only two molecules are present, is called the water dimer and is often used as a model system. The hydrogen bond is stronger than a Van der Waals interaction, but weaker than covalent, or ionic bonds. Hydrogen bonding is highly directional. The selectivity and directionality of hydrogen bonds stabilizes the formation of supra molecular architectures.

- Coulomb repulsion and steric effects

  Other more complex factors in the formation of supra molecular networks are the Coulomb repulsion of equally charged functional groups and steric hindrance. The system will always try to arrange itself in such a way to minimize these effects.

- Metal-Coordination Bonds

  Metal-organic coordination bonds represent a compromise between bond strength and bond reversibility. Generally speaking, a coordination system consists of a coordinating metal atom (or cluster of atoms) with one or more electron rich ligands attached to it. Metal-organic coordination complex (MOCNs) have been realized on well defined metal surface under ultra-high vacuum (UHV) conditions. The binding energies are higher than in the case of hydrogen bonds, ranging from 0.1-3 eV. Based on molecular orbital theory the bonding mechanism of a coordination compounds can be described by the following sequence [41]:

  (a). Removal of electrons from the metal center (i.e. oxidation) in order to provide a cation.

  (b). Hybridization of the metal atomic orbitals which provides a set of equivalent hybrid orbitals directed towards the ligands.

  (c). If necessary, rearrangement of the metal electrons to ensure that the hybrid orbitals are unoccupied.

(d). Formation of covalent σ-bonds between metal center and ligand by the overlap of metal hybrid orbitals with ligand orbitals containing lone-pair electrons.

The ligand field theory (LFT) describes the bonding, orbital arrangement, and other characteristics of coordination complexes [101]. It represents an application of molecular orbital theory to transition metal complexes. A transition metal ion has nine valence atomic orbitals: five nd, one (n+1)s, and three (n+1)p orbitals. These orbitals are of appropriate energy to form bonding interaction with ligands. The LFT analysis is highly dependent on the geometry of the complex. When examining a single transition metal ion, the five d-orbitals have the same energy. When ligands approach the metal ion, some experience more opposition from the d-orbital electrons than others based on the geometric structure of the molecule.
Since ligands approach from different directions, not all d-orbitals interact directly. These interactions, however, create a splitting due to the electrostatic environment. For example, consider a molecule with octahedral geometry (in Figure 1.2 (a)). Ligands approach the metal ion along the x, y, and z axes. Therefore, the electrons in the d_{z^2} and $d_{x^2-y^2}$ orbitals (which lie along these axes) experience greater repulsion. It requires more energy to have an electron in these orbitals than it would to put an electron in one of the other orbitals. This causes a splitting in the energy levels of the d-orbitals. This is known as crystal field splitting. For octahedral complexes, the crystal field splitting is denoted by Δ_0. The energies of the d_{z^2} and $d_{x^2-y^2}$ orbitals increase due to greater interaction with the ligands. The d_{xy}, d_{xz}, and d_{yz} orbitals decrease in energy with respect to the normal energy level and become more stable as shown in the Figure 1.2 (b).

In a square planar complex (in Figure 1.2(c)), there are four ligands. However, the difference is that the electrons of the ligands are only attracted to the xy plane. Any orbital in the xy plane has a higher energy level. There are four different energy levels for the square planar (from the highest energy level to the lowest energy level): $d_{x^2-y^2}$, d_{xy}, d_{z^2}, and both d_{xz} and d_{yz} are shown in Figure 1.2(d) . Crystal field theory qualitatively describes the strength of the metal-ligand bonds. Based on the strength of the metal-ligand bonds, the energy of the system is altered. This may lead to a change in magnetic properties as well as color [121].

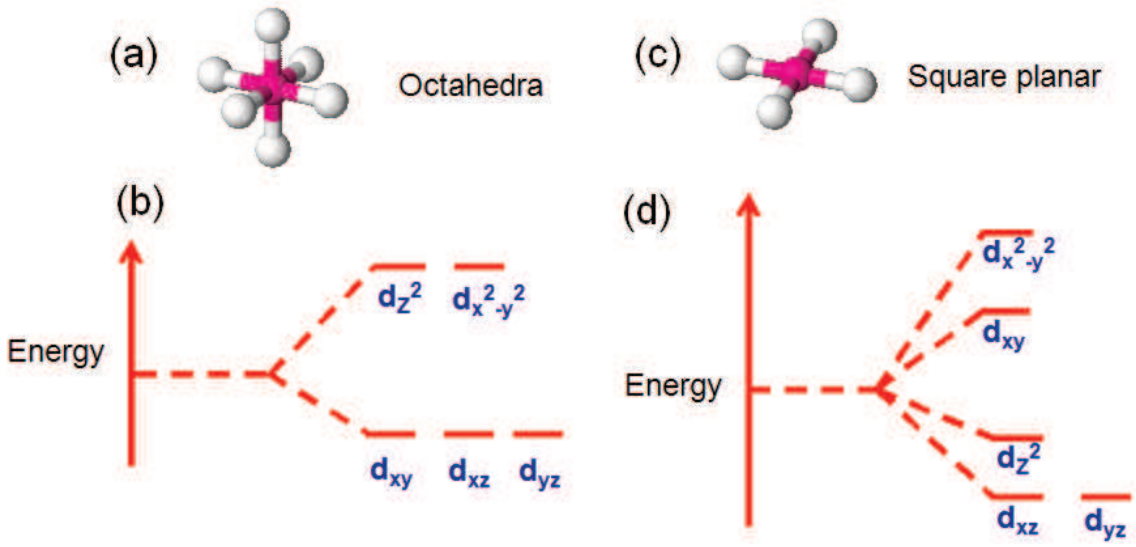

Figure 1.2: (a, b) a schematics of octahedral complex and corresponding crystal field splitting diagram due to the ligand. (c, d) Square planar complexes and corresponding crystal field splitting diagram.

Hence, the formation of metal-coordination complexes and networks is mostly determined by the coordination geometry of the metal center which for transition metals depends on the d-orbital occupation. Under 2D conditions, however, the presence of a metal substrate makes it difficult to predict coordination geometries in comparison to a known 3D analogue. Whereas in 3D the element determines the geometry, in 2D "unusual" motifs can occur. Such deviations can be attributed to charge transfer or substrate screening effects [111] that severely affect the metal to ligand bonding within a 2D network.

1.2.2 Molecule-substrate interaction

Interactions between molecules, with the solid substrate or other templates can also play a non negligible role in two dimensional supra molecular assemblies. Chemisorption and physisorption are the two main effects dominating the molecule-substrate interactions.

Physisorption is a process in which the electronic structure of the atom or molecule is barely perturbed upon adsorption. The fundamental interacting force of physisorption is caused by van der waals force. Even though its interaction energy is very weak, physisorption plays an important role in nature.

Chemisorption is an adsorption process characterized by a strong interaction between an adsorbate and the substrate surface. Covalent and ionic interac-

tions are involved in the chemisorption process, leading to the formation of chemical bonds. In comparison, the physisorption is a process in which there is no mixing of the electronic states of the atom or molecule with those of the substrates and the forces involved are mainly week Van der Waals forces. The physisorption does not involve any chemical bonds. In the case of molecules adsorbed on a surface, non-covalent weak forces dominate the molecule-substrate interaction. The molecular self-assembly results from the combination of intermolecular forces and molecule-substrate interaction, where the crystalline structure of the surface plays a key role [78]. In this regard, molecule-substrate interaction usually determines adsorption geometry (epitaxy) and conformation at low coverage.

Most of the techniques used for measuring the electronic and the magnetic properties of adsorbates, such as x-ray photoelectron spectroscopy (XPS), X-ray magnetic circular dichroism (XMCD) etc, have a limited spatial resolution between 10 and 100 nm and offer only an access to spatially averaged magnetic properties. The advantage of these techniques is that they are element specific but the ensemble averaging over a large area is clearly a disadvantage. In general, the self-assembly of metal atoms and organic ligands on metal surfaces leads to different phases depending on the experimental parameters. Therefore, the local probe techniques are more appropriate to study this kind of systems. Progress in scanning probe microscopy allows a deeper understanding of elementary chemical processes taking place when different species adsorbed on the metal surfaces react with each others. The techniques have been used both, to follow chemical reactions at the atomic scale and to induce the reaction by various STM tip manipulations [23, 24].
Recent studies using cryogenic scanning tunneling microscopy have illustrated the fabrication of various coordination geometries on well defined metal surface. Depending on the types of organic linkers and symmetry of surfaces, different coordination structures are formed such as, honeycomb like structure, window like structures, and chains. Scanning tunneling microscopy not only access the geometry of the coordination structures but also its chemical state and its magnetism. Some of these studies are highlighted in the next section.

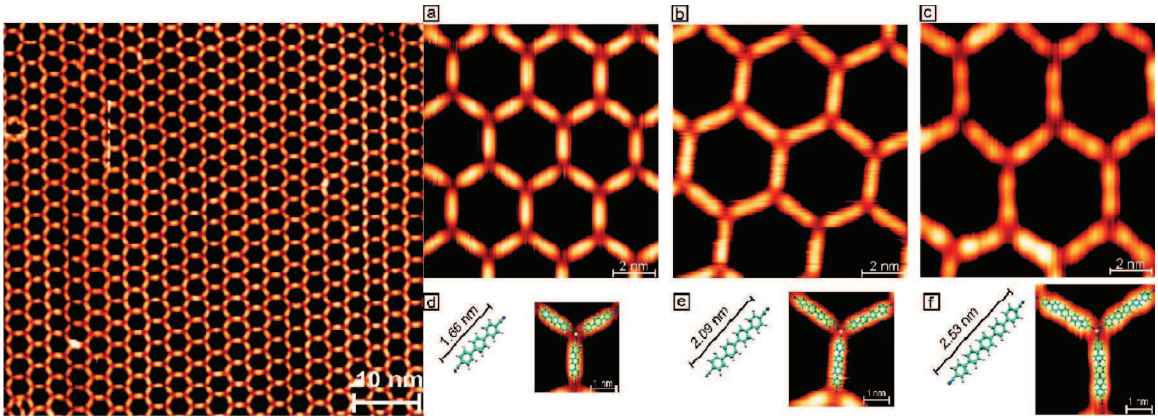

Figure 1.3: (a) STM topographic image of the metal−organic network formed by NC−Ph_3−CN linkers, image size 300 × 300 nm^2 (b) Tuning the cavity size of metal−organic honeycomb networks with designed linkers. The STM images show the result of Co-directed assembly of (a) NC−Ph_3−CN, (b) NC−Ph_4−CN, and (c) NC−Ph_5−CN, respectively. (d-f) Structure of the molecules including their length and models of the threefold Co-carbonitrile coordination motif resolved in (a-c) (yellow, cobalt center; turquoise, carbon; white, hydrogen; blue, nitrogen). The images (a-c) were taken at a tunnel current of I = 0.1 nA and bias voltages of 0.9, 1, and 2 V, respectively (from ref [102]).

1.3 Tuneable metal−organic coordination networks

The experiment performed by U. Schlickum et al. [102] can be regarded as an example of supra molecular chemistry with its unique control of highly organized molecular architecture on metal surfaces. In this experiment, the Ag(111) surface is used to fabricate surface-supported highly regular metal−organic nanomeshes covering μm^2 large areas by exploiting the interaction of carbonitrile groups with Co centers. Figure 1.3 shows an STM topographic image of the metal−organic network formed by NC−Ph−CN linkers. More interestingly, the network size can be tune by changing the length of the linkers from 1.66 nm to 2.53 nm as shown in the Figure 1.3. Additionally , the surface atoms of the substrate play a key role for the stabilization of the threefold coordinated Co centers, in other words it is the strong hybridization between Co and Ag atoms that leads to stable threefold coordinated Co centers.

Fabrication of fourfold coordinated metal-organic networks (window) is also possible by a careful choice of substrate and organic linkers [68] containing a carboxyl group at one end and a pyridine group at the other end. After deposition of a small amount of Fe atoms at room temperature, the window is formed by two Fe-atoms bridge between two carboxylates and the pyridine groups as shown in Figure 1.4. This specific type of coordination network can be used to investigate the nature of the self-assembled structures of a library containing two different bipyridine ligands and three different bis-carboxylic acids (Figure 1.4). The co-deposition of each of

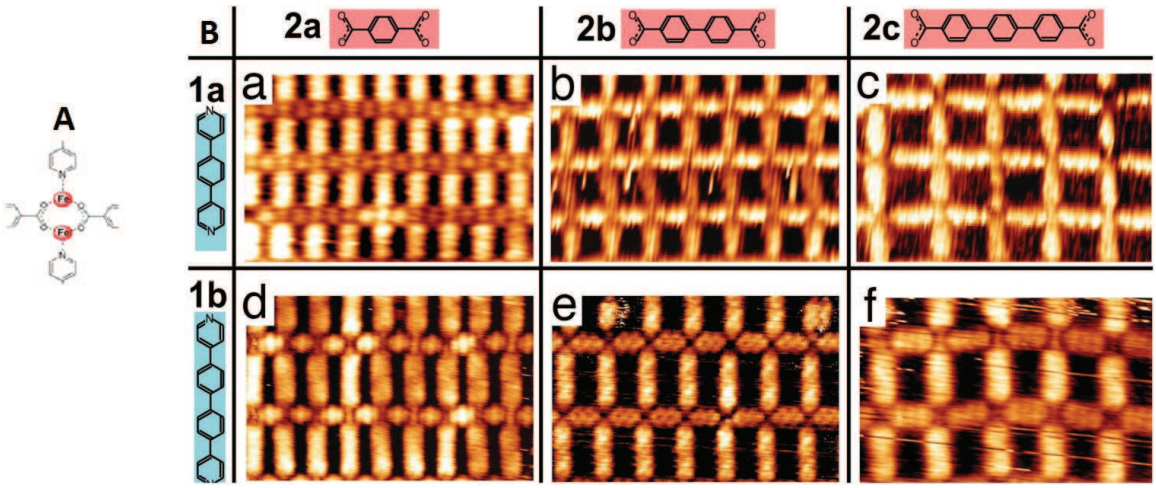

Figure 1.4: (A) The coordination motif in networks composed of Fe-atoms, pyridine and carboxylic acid ligands. (B) UHV STM images ($9.4 \times 6.0\ nm^2$) of networks formed by the co-assembly of Fe-atoms with six possible combinations of bipyridine and bis-carboxylic acid ligands; structure periodicities are (a) $1.1 \times 1.8\ nm^2$, (b) $1.5 \times 1.8\ nm^2$, (c) $1.8 \times 1.8\ nm^2$, (d) $1.1 \times 2.3\ nm^2$, (e) $1.5 \times 2.3\ nm^2$, (f) $1.8 \times 2.3\ nm^2$ (from ref [68]).

the combinations of the ligands together with Fe atoms yields highly regular porous networks with the cavity areas ranging from 1.9 nm^2 to 4.2 nm^2, in which the internal dimensions of the compartments can be tuned by choosing the ligands of the appropriate length. Notably, the horizontal rows all consist of the dicarboxylates, while the vertical pillars are formed by the bipyridines. This type of self-assembly is a promising candidate to study dynamics and self-selective bond nature between the ligands and metal atoms on metal surface. However the magnetic properties of such a network is still an open question, especially the nature of the coupling between closest Fe dimers in the molecular environment.

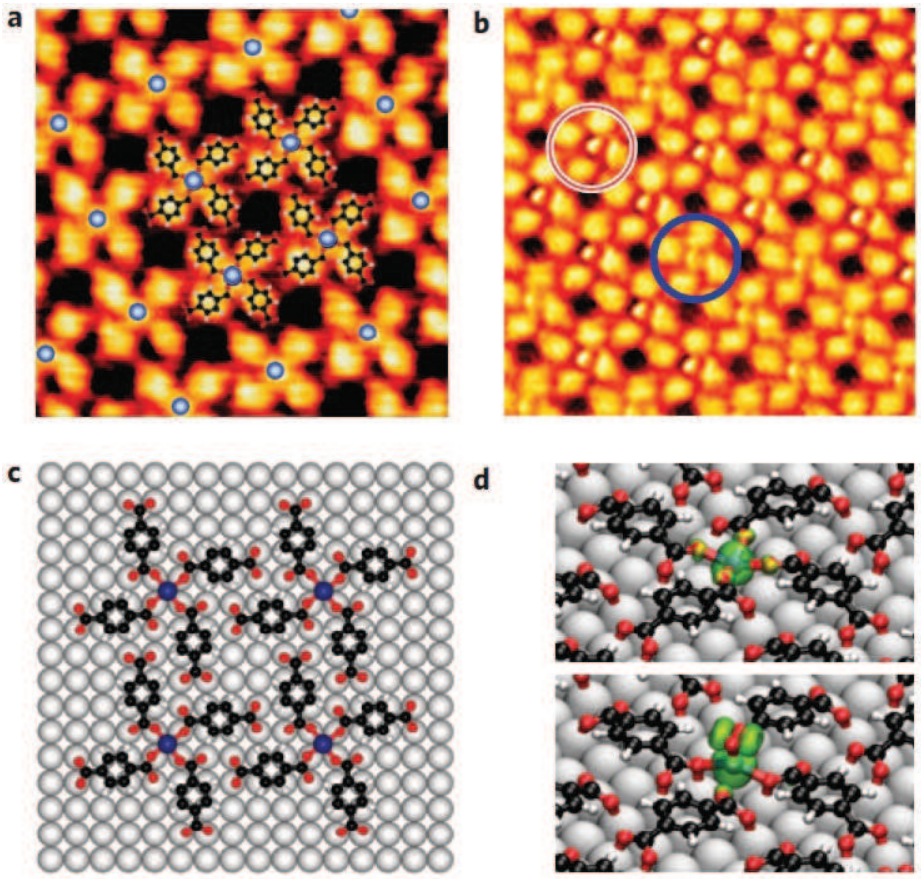

Figure 1.5: Planar supra molecular layers of FeTPA complexes self-assembled on Cu(100). (a) $Fe(TPA)_4$ array; blue dots indicate the position of Fe atoms. Each Fe center is coordinated to four deprotonated oxygen ligands of the surrounding TPA molecules. STM image size 62×62 Å^2. (b) Selective uptake of O_2 by Fe; a change of STM contrast is observed for $O_2Fe(TPA)_4$ (red circle) at the Fe location compared with $Fe(TPA)_4$ (blue circle, 84×84 Å^2). (c) Top−view model of $Fe(TPA)_4$ coordination and supporting Cu(100) substrate. (d) Relaxed $Fe(TPA)_4$ and $O_2Fe(TPA)_4$ supra molecular structures obtained by DFT. Fe (blue), O (red), C (black) and H (white) atoms are shown together with the spin density distribution (green). (from ref [35]).

1.4 Two-dimensional high-spin Fe arrays formed on metal interface

As mentioned above, co-deposition of transition-metal ions and organic ligands on single-crystal surfaces offers the potential to design supra molecular metal-organic grids with programmable structural features. In some case [35] it was possible to control the magnetic properties of the Fe atoms in the molecular network independently from the substrate. For example, the magnetization direction of the Fe centers can be switched by oxygen adsorption, thus opening a way to control the magnetic anisotropy in supra molecular layers. Figure 1.5 shows the supra molecular assembly of Fe and terephthalic acid (TPA) molecules on a Cu(100) surface. Each Fe atom

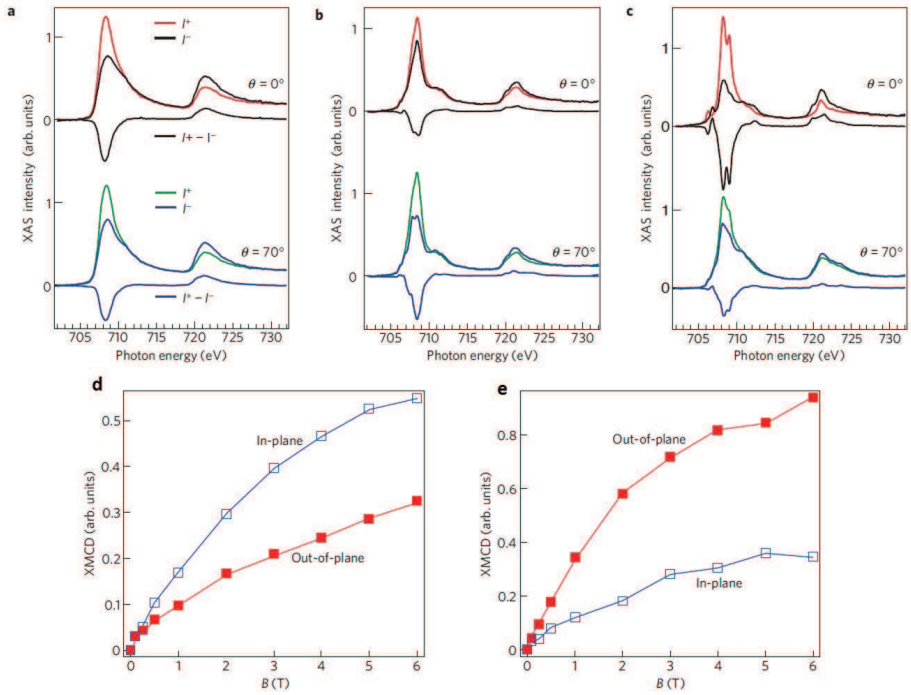

Figure 1.6: Circularly polarized X-ray absorption spectra of Fe/Cu(100)(a), $Fe(TPA)_4$(b), and $O_2Fe(TPA)_4$(c) and corresponding element-selective magnetization curves of the Fe centers $Fe(TPA)_4$(d) and $O_2Fe(TPA)_4$(e)respectively (from ref [35]).

is coordinated to four TPA molecules through Fe-carboxylate bonds, and the supra molecular $Fe(TPA)_4$ units are organized in a square lattice with $15\times$ Å^2 periodicity. STM images indicate that, despite the 4−fold lateral coordination to the carboxylate ligands and the residual interaction with Cu, Fe centers are chemically active, forming an array of open coordination sites that may selectively bind other ligands, for example, O_2 to form pyramidal-like O_2-$Fe(TPA)_4$ complexes. To obtain the bonding and magnetic properties of transition-metal ions, X-ray absorption spectra (XAS) and X-ray magnetic circular dichroism (XMCD) measurements have been performed. Figure 1.6 shows the XAS intensity after Cu background subtraction at low temperature (8 K) with a magnetic field of 6 T applied with different angles 0° and 70° respectively. Comparing different XAS line shapes from (a) to (c) it can be easily seen that Fe/Cu(100) exhibits broad L_3 and L_2 peaks typical of a metal Fe. $Fe(TPA)_4$ on the contrary shows narrowing of the spectral features and a well-defined multiplet fine structure is observed due to the ligand-induced modifications and localization of the Fe d-orbitals. The major finding of this work is to show that the easy magnetization direction of the Fe centers can be switched by oxygen adsorption, thus opening a way to control the magnetic anisotropy in supra molecular layers on the metal surfaces.

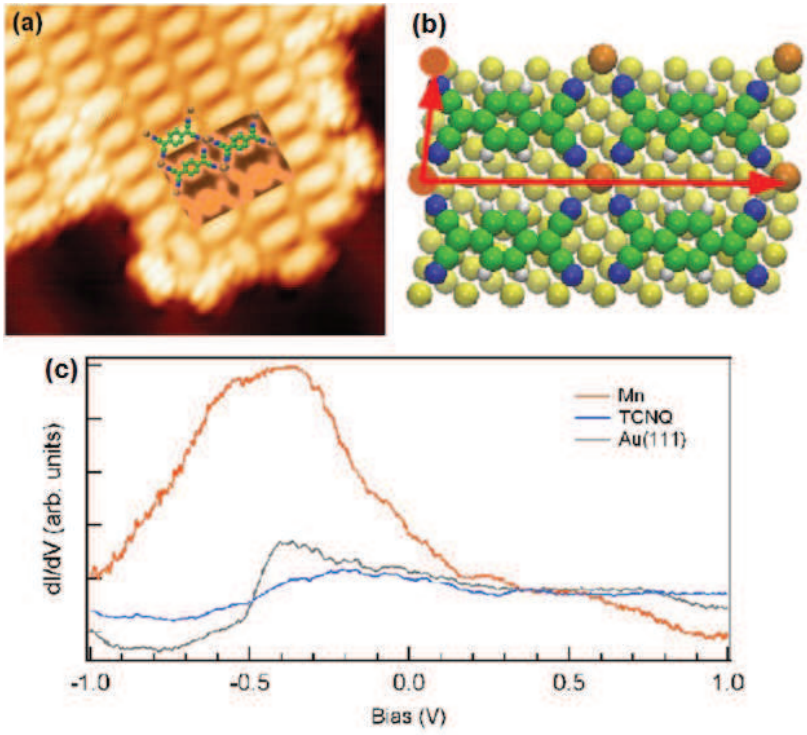

Figure 1.7: (a) STM topographic image of (8 nm 6.6 nm) MnTCNQ on Au(111) (I = 0.17 nA and U = +1.2 V) with an schematic geometrical representation. (b) Optimized structural model based on STM data (unit cell vectors are drawn in red). C, N and H atoms are represented by green, blue, and light gray circles, respectively. The golden circles between TCNQ molecules represent Mn atoms which are coordinated with four CN groups. (from ref [77]).

1.5 Metal-organic coordination networks on Au(111) with strong acceptor molecules

Coordination of transition metal atoms with strong electron acceptor molecules such as TCNE (tetracyanoethylene), TCNQ (7,7,8,8-tetracyanoquinodimethane) or F_4TCNQ (2,3,5,6-tetrafluoro-7,7,8,8- tetracyanoquinodimethane) are expected to induce the localization of spins in the 2D metalorganic networks [118, 117, 104, 77]. Figure 1.7 (a) shows high resolution STM images of the MnTCNQ metalorganic networks on Au(111) surface and Figure 1.7(b) corresponding structural model based on STM data. Each Mn center is coordinated to four TCNQ ligands via the cyano groups, the N-Mn bond length being 2.3 Å . Figure 1.7(c) shows the dI/dV spectra taken at the center of the TCNQ molecule (blue curve) and at the Mn adatom position (red curve). A strong and broad signal is observed in the range of occupied states in the dI/dV spectrum at the Mn adatom position. It has been reported that upon adsorption of TCNQ on Au(111) the surface state is shifted upwards in energy by about 150 mV [56] and a peak appears at +0.8 V that can be ascribed to the LUMO of the neutral TCNQ molecule. Upon coordination with the Mn atoms neither of these two features is observed anymore. Altogether, these observations point toward the existence of a strong hybridization between Mn, TCNQ and the Au(111) substrate, including the quenching of the Au(111) surface state and the mixing between Mn states and the LUMO of the TCNQ molecule.

The magnetic measurements of the networks are made by the TCNQ and Ni atoms on Au (111) surface also been reported [84]. The XMCD results indicate that the magnetic moments of Ni adatom impurities on the surfaces of Au(111) and Ag(100) are quenched due to the strong hybridization with the surface. Upon coordination to TCNQ, the Ni atoms recover their magnetic moments and show a ferromagnetic coupling. The electronic configuration and strength of the magnetic coupling depends crucially on the substrate, with stronger ferromagnetic interaction on the Au compared to the Ag surface. The results suggest a superexchange coupling mechanism via the negatively charged TCNQ ligands. The difference in the coupling strength and the electronic structure is traced back partly to the distinct charge state of TCNQ and charge transfer mechanisms between Ni and ligand molecules on the two surfaces. The results demonstrate the direct synthesis of planar two-dimensional metal-organic magnets on metal surfaces that opens up a new route in the design, fabrication and investigation of low-dimensional magnetic materials at surfaces.

In this chapter we have presented a general introduction of molecular self assembly on the metal surface. The fundamental knowledge on the nature and strength of the intermolecular and molecule-substrate interactions that govern the ordering of molecular adsorbates have been presented. A number of case studies, selected among the recent works, on the self-assembly of metal-organic coordination networks on solid surfaces are discussed. The coordination networks can be synthesized on solid surfaces by codeposition of organic ligands and metallic adatoms. By altering size, geometry, and chemistry it is possible to tailor functionalities in unprecedented ways. As far as the magnetic properties are concerned it looks like the magnetic atoms in the above two examples (honeycomb and window) are too far apart to interact significantly through the superexchange or through conduction electrons by RKKY type of interaction [35, 119]. To overcome this severe limitation, smaller bridging ligands must be used. Among the potential candidates, the TCNQ ligands have shown a remarkable ability to produce spin related phenomena due to the magnetic atoms inside the network. In this thesis we will form a network by the less studied TCNB moiety in combination with the Fe atoms.

Chapter 2

Scanning tunneling microscopy and related techniques

This chapter starts with a detailed description of the apparatus which was designed to operate at low temperatures and in ultra-high vacuum (UHV) environment. Our UHV system consists of a stainless-steel main chamber which houses ports for the equipments used in analyzing, preparing, and manipulating the samples. This chapter also gives a brief introduction of scanning tunneling microscopy (STM) and scanning tunneling spectroscopy (STS) as well as their working principles. The different working modes of STM/STS, such as, constant current topography, $dI/dV(V)$ local spectroscopy as well as constant current $dI/dV(V)$ mapping are presented. An introduction about the origin of the surface states of the noble metal surfaces and localization by atomic impurities is also given. The last section of this chapter gives the technical details of sample and tip preparation and atom/molecular deposition techniques in the ultra high vacuum (UHV).

2.1 Experimental setup

2.1.1 STM in the ultra-high vacuum

Ultra high vacuum(UHV) is often require, for two main reasons: **1**. To enable atomically clean surfaces to be prepared and to keep them in a contamination-free state for the duration of the experiment. **2**. To permit the use of low energy electron and ion-based experimental techniques. For this purpose, the Createc LT-STM system is especially designed for working at atomic scale, low temperature and UHV condition. The so-called Pan slider design ensures a very high stability (dz<1 pm under ideal circumstances) and a small drift. The most important building block of a STM is the piezo tube (Figure 2.1 (a)). A piezo tube is made of piezoelectric crystals that

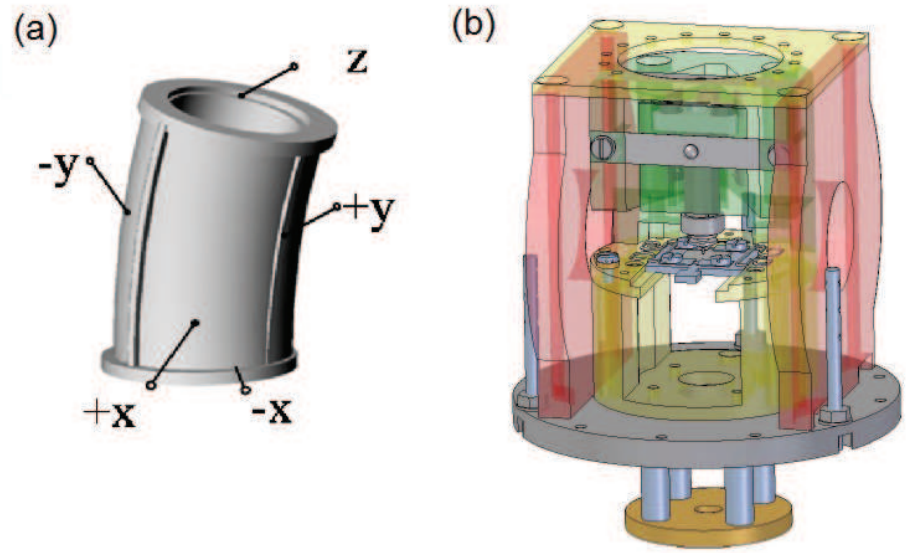

Figure 2.1: (a) XYZ piezo tube. High voltage applied to the six electrodes can make the tip move in all directions, with very high accuracy. (b) Schematic drawing of the pan slider type STM. .

contract or expand if a voltage is applied. The tube has six electrodes that can be addressed separately, thereby enabling piezo movement in three directions x, y and z with very high accuracy. In the slider STM (Figure 2.1 (b)), the design is based on a prism-shaped slider. The Pan design relies on a total of six shear piezoelectric actuators in two rings around the slider. The prism will only move a small distance with each cycle, typically less than 1 μm. Moving a millimeter or more, as will be required after a tip or sample change, will require of the order of 1000 cycles. The STM tip is mounted on a tip holder at the end of the main piezo. The sample lies on a small table with six electrical spring contacts, for applying the bias voltage. This table is mounted on a stainless steel pole that can be pulled up and down to put the sample in measuring or in transfer/cooling position. In the upper position the reference planes of the sample holder touch the bottom side of the base plate, guaranteeing a correct vertical positioning of the sample holder (Figure 2.2).

Numerous wires are connected to the STM body. There is a contact on each piezo electrode, one on the base plate and one on the tip holder to measure the tunnel current. Two cables lead to temperature diodes of which one is attached to the STM and the other to the 4K helium bath.

2.1.2 Cryostat

The STM body is located inside the cryostat. In Figure 2.3 a schematic is displayed. The outer cryostat can hold up to 13.3 L of liquid Nitrogen and has to be refilled

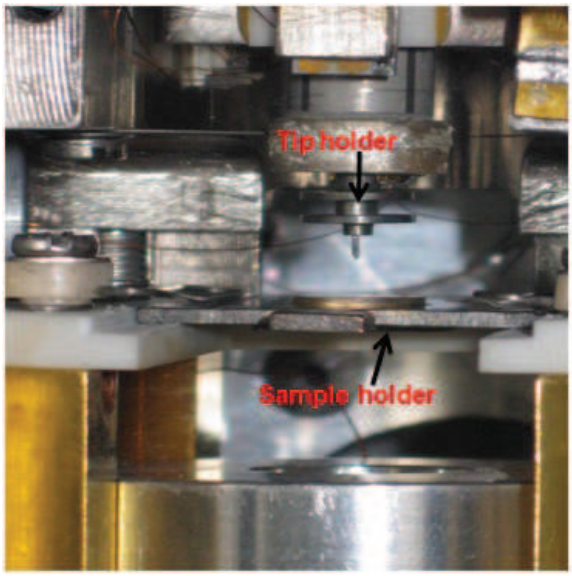

Figure 2.2: Picture of the STM inside the cryostat. The tip is mounted on a tip holder at the end of the main piezo. The sample lies on a small table with six electrical spring contacts, for applying the bias voltage

every 48 hours. Inside, the helium cryostat is suspended from four adjustable screws at the top so that it is isolated from the outer cryostat. The inner cryostat is filled with 4.3 liters of liquid helium and has a stand alone time of at least 60 hours. Two radiation shields are connected to the different cryostats and in the middle the STM body is located. The shields have two small view ports, a door that can be opened for sample transfer and one shutter for in-situ evaporation. In the bottom of the outer radiation shields are magnets that induce eddy currents in a copper plate under the inner shield. This quickly damps any small relative movements of the two cryostats. During measurement the STM body hangs freely from the inner cryostat with three springs, with minimal thermal contact to the bath. It can be pulled onto copper blocks on the bottom of the inner cryostat for sample exchange and cooling. When the STM is released, the cooling only occurs through the springs which have a poor thermal conductivity, but the radiation shields keep the STM from warming up in this position. This design, where the complete STM and the electrical wires are cooled to about 5K, minimizes thermal drift and noise.

2.1.3 Vacuum chambers

A single large vacuum chamber is divided by an integrated gate valve into a preparation chamber which contains the sample cleaning and preparation facilities, such as, an ion gun, and electron beam evaporation sources and a part which contains

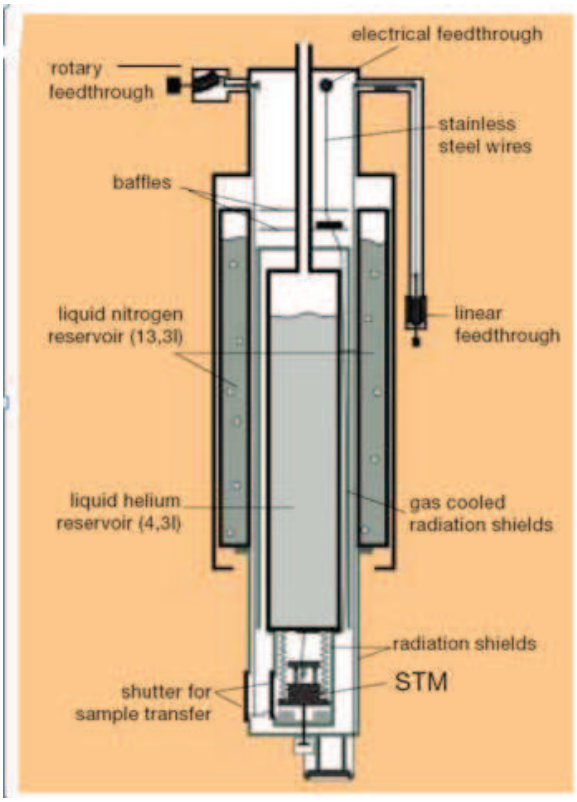

Figure 2.3: Schematic of the cryostat. The STM hangs from the inner cryostat and is surrounded by radiation shield

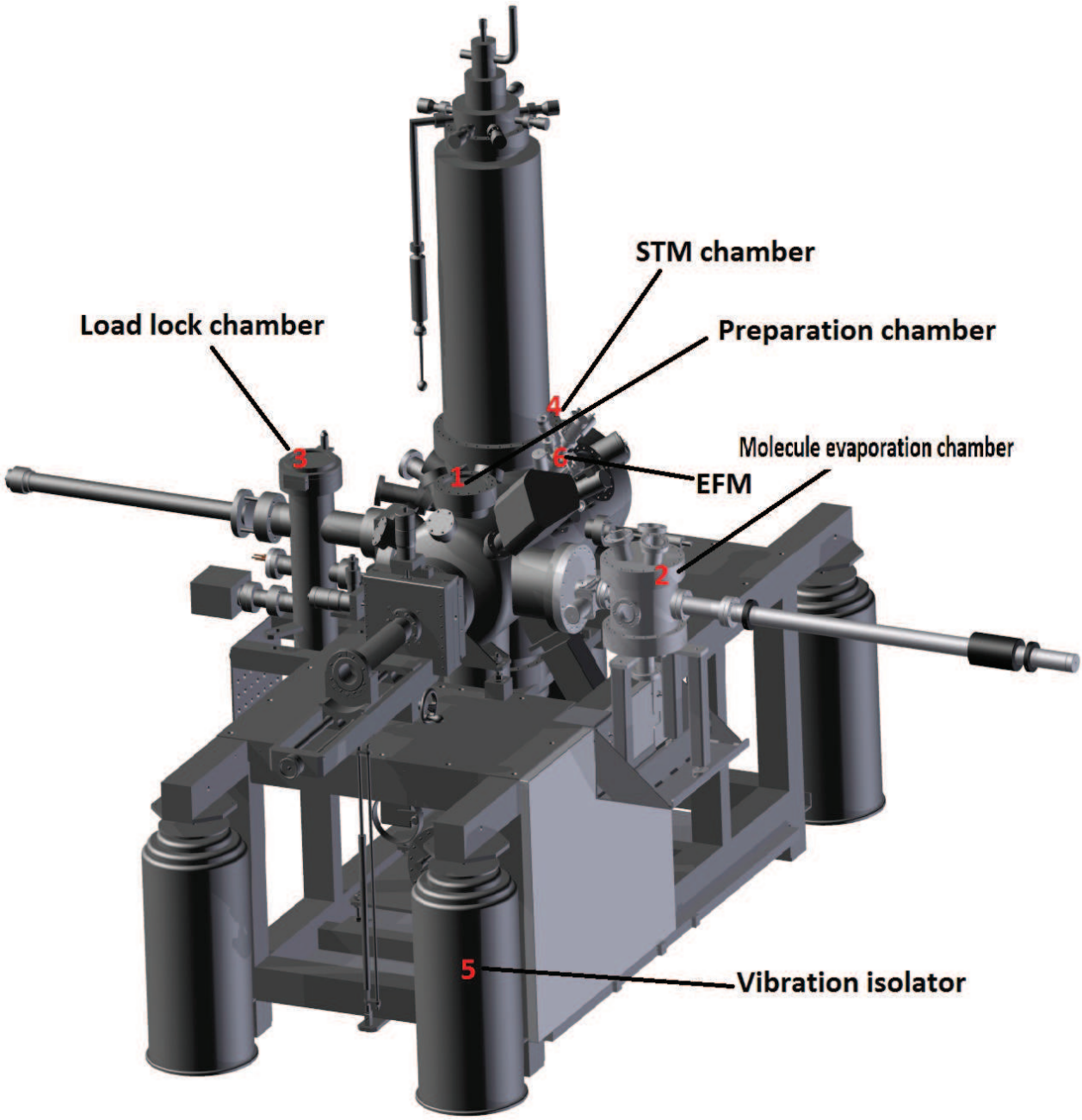

Figure 2.4: Perspective view of the UHV system with its components: (1) preparation chamber, (2) molecule evaporation chamber, (3) lock load chamber and (4) STM chamber (5) Vibration dampers

the STM. A sample can be brought from the load lock into the prep chamber on a transfer rod. There it can be mounted on the manipulator. The load lock chamber also contains a home-built evaporation sources, designed to evaporate molecules (see below). The complete system is supported by Newport active vibration isolation dampers (Figure 2.4). The system is vacuum pumped in several ways. The load lock has a large turbo pump, backed up by a small turbo and a rotary pre-pump. The prep chamber and STM chamber both have a ion getter pump fitted with titanium sublimation filaments. And last but not least; very effective cryopumping occurs on the 4.2 K cryoshield of the STM. When the load-lock is closed and at least one ion-pump is operative the base pressure of the system is around 5×10^{-10} mbar. During measurements usually the turbo pump is shut down to reduce the electronic and vibrational noise.

2.1.4 Electronics

Although the STM itself is very small (< 10 cm^3), a full range of electronics is necessary to perform measurements with atomic precision. First of all the piezos need high voltages up to 200 V with very high accuracy. Secondly, a tunnel current of typically 100 pA is amplified with a 109 A/V amplification factor before it is introduces into the feedback system, while variations in order of 1 pA must be conserved. Thirdly, this needs to be controlled by a data acquisition program on a standard computer. Here follows a short description.

2.1.5 Digital signal processor (DSP)

The digital signal processor DSP (Figure 2.5) board PC32 from Innovative Integration is the heart of the STM measurement electronics. It is controlled by the computer through the AFM-STM program, but also has the electronic feedback loop integrated. The DSP has four 16 bit D/A converters and four 16 bit A/D converters. They have a BNC connection on the front end which are designated as DAC0-3 and ADC0-3. Each has an input/output between -10 to 10 V in 65536 steps. This gives a maximal resolution of 0.306 mV. This corresponds to a 2.25 pm movement of the z-piezo at 5 K.

The sampling rate of the ADC's is 50 kHz (20 μs) and this is also the time between two different output values on the DAC's. The x, y, z movement of the piezos is controlled by DAC2, DAC3 and DAC0 respectively. The bias voltage comes from DAC1 and the tunnel current is measured at ADC0. An external lock-in amplifier

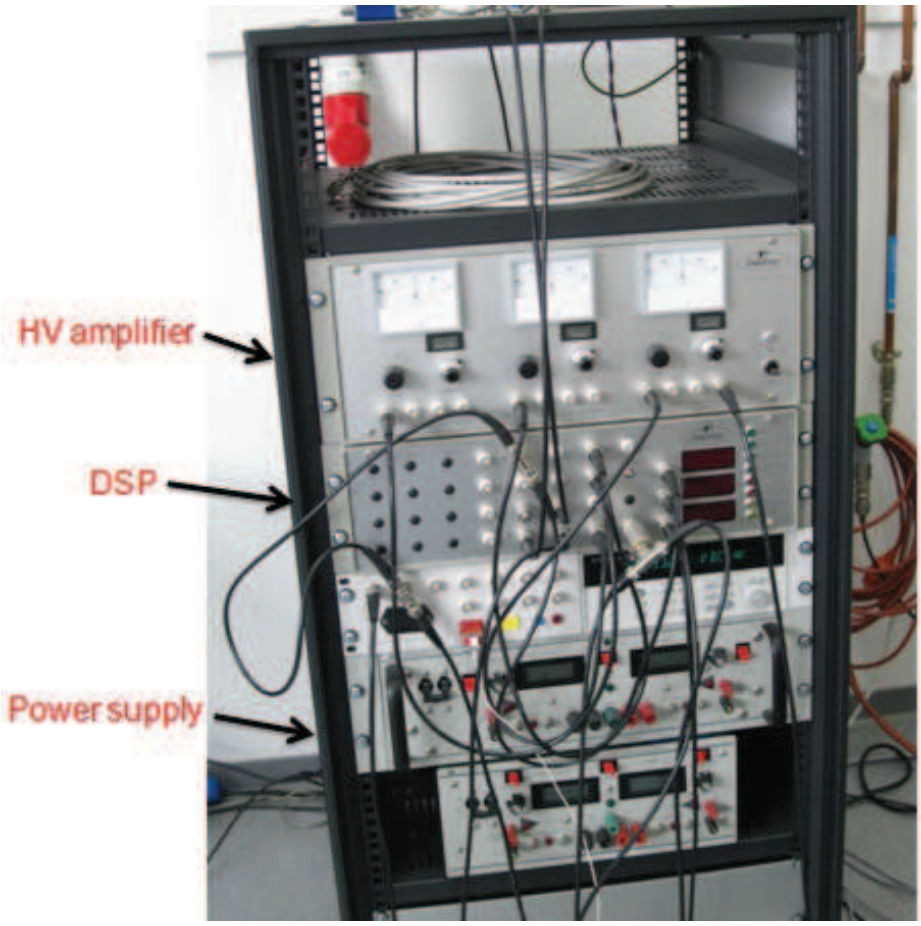

Figure 2.5: The main electronic components of the LT-STM which contains a digital signal processor and a high voltage amplifier.

for spectroscopic measurements can be connected to ADC1. Furthermore, four 10 μA constant current sources, a digital voltmeter, and a mixing amplifier to add a modulation to the bias voltage are located at the frontend of the DSP. On the backside the DSP is connected to the computer and the high voltage amplifier stage of the different components.

The electronic feedback loop is also built into the DSP. During constant current imaging the feedback loop compares the input of ADC0 (the tunnel current) with the current value set by the operator. The difference between these signals is then used to send a signal through DAC0 to the z piezo. The integration time of the feedback loop as well as the sort of response, logarithmic or linear, can be chosen by the operator.

2.1.6 Pre-amplifier

The tunnel current is measured from a direct contact on the tip holder on the main piezo. A single wire ends in a BNC plug on top of the cryostat. A low-noise variable-gain preamplifier (preamp) converts the current into a voltage typically with a 109 V/A amplification before it is lead to the DSP at ADC0. A tunnel current of 1 nA is then measured as 1 V by the DSP. The preamp has two settings. The low-noise setting has a maximum amplification of 109 and a cutoff frequency of 1.2 kHz. All changes in the tunnel current above this frequency will not be transmitted to the DSP thereby limiting the speed of the feedback system.

2.1.7 High voltage amplifier

The high voltages amplifier (Figure 2.5) must deliver voltages up to 200 V that can be ramped within 1 second, but nonetheless with about 1 mV precision to have dz<1 pm. This requires the best high voltage amplifier stage on the market. The amplifier converts the $\pm$10 V of the DAC's into voltages suitable for the piezos. Three separate amplifier chips are controlled by the outputs DAC0(z), DAC2(x) and DAC3(y) of the DSP. Besides that a voltage offset over the full 200 V range can be added by ten-turn potential meters. The amplifier output for xy is fixed, but the z output can be connected to the main or to the coarse piezos manually. The switching between coarse movement and scanning for xy occurs via relay switching inside the amplifier, directly controlled by the computer. A variable gain in step of 1, 3 and 10 can be selected depending on the temperature, because the piezo response to an applied voltage gets smaller for lower temperatures. At room temperature the xy and z piezo constants are about 100 Å/V and 80 Å/V respectively. For helium this is about 20

Å/V and 7.50 Å/V. These are values given by the manufacturer and still have to be calibrated exactly using a well known surface such as Au(111). At He temperature the amplifier must be set to gain 10. The maximum input voltage then results in a 750 Å expansion in the z-direction and about 1600 Å in the xy-direction at 5 K. The total scan range is thus 3200 Å in xy and 1500 Å in z.

Finally, the Createc STM-AFM program controls coarse movement of the tip, STM image acquisition, tunneling spectroscopy, tip forming and noise analysis. It also has built-in options for atomic manipulation and some features for image processing.

2.1.8 Principle of scanning tunneling microscope

The Scanning Tunneling Microscope (STM) was invented in 1981 by G. Binnig and H. Rohrer [11, 89] and within the few years it become the most widely used tool in surface science. STM represents a paradigm shift from seeing in the sense of viewing, to tactile sensing – recording shape by feeling, much like a blind man reading Braille. The operation of a STM is based on a quantum mechanical electron tunneling current, felt by a sharp tip in proximity to a surface at a distance of approximately one nanometer. The tip is mounted on a three dimensional actuator like a finger as shown schematically in Figure 2.6

This sensing is recorded as the tip is mechanically scanned across the surface, producing contours of constant sensing (in the case of STM this requires maintaining a constant tunneling current). The acquired information is then displayed as an image of the surface topography [12]. In the typical working mode of STM (constant-current or topography mode) the tip is scanned line wise over a region of the surface and the tunneling current is kept constant by regulating the tip height (z) through a feedback loop. A map of surface is obtained by assigning to each lateral (x, y) position of the scanned region the tip height $z(x, y)$. In this mode the tip follows roughly the corrugation of the surface, creating a nearly topographic map. However, the STM image is also influenced by electronic effects. More precisely the tip moves on a surface of constant local density of states (LDOS) close to the Fermi energy. In general it is not trivial to distinguish between topographic and electronic effects. Another working mode of STM is called constant height mode. In this mode, the vertical position of the tip is not changed, this is equivalent to a slow or disabled feedback.

The current as a function of lateral position $I(x, y)$ represents the surface image. This mode is only appropriate for atomically flat surfaces as otherwise a tip crash would be inevitable. Createc LT-STM standard scan range of 1.5 μm $\times$ 1.5 μm $\times$ 0.3

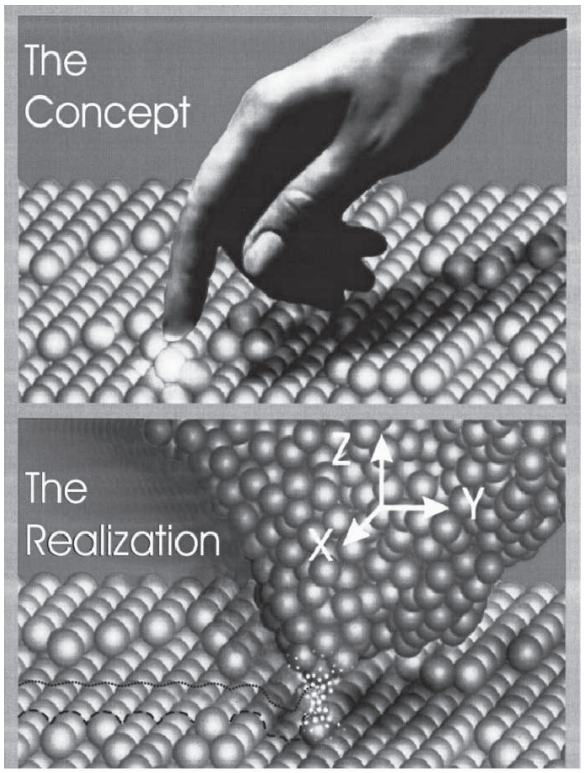

Figure 2.6: Principle of a local probe: The gentle touch of a nanofinger. If the interaction between tip and sample decays sufficiently rapidly on the atomic scale, only the two atoms that are closest to each other are able to feel each other.(from ref [12]).

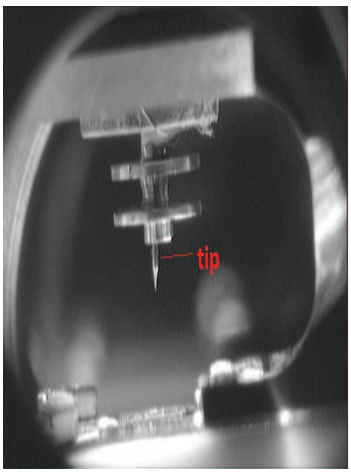

Figure 2.7: Snapshot of control the exact position of the tip with the help of a camera

μm can be adapted to the desired range. The minimum tunneling current is 2 pA. The system provides optical access onto the sample to control the exact position of the tip with the help of a camera (Figure 2.7). The sample transfer can also be done at low temperature.

2.1.9 Theoretical background of STM

The basic mechanism of the STM is the quantum tunneling of electrons, which describes the motion of electrons through a potential barrier of finite height and width. In classical mechanics, particles are completely reflected from the barrier and not allowed to move across it if its energy is lower than the barrier height. However, quantum mechanics allows the particles to penetrate the barrier with non-zero probability as shown schematically in Figure 2.8. The electrons are described by the solution $\psi(x)$ to the Shrödinger equation. Inside the material, the solution of $\psi(x)$ is a complex exponential function describing a wave, but at the surface the electron wave function decays exponentially into the vacuum. For the 1D case:

$$\psi(z) = \psi(0)e^{-2\kappa z}, \tag{2.1}$$

with z perpendicular to the surface the surface corresponding to z = 0 and

$$\kappa = \frac{\sqrt{2m_e(V_0 - E)}}{\hbar}, \tag{2.2}$$

where V_0 is the height of the vacuum barrier, and E is the energy of the electron. The probability density to find the electron in the vacuum is the square of the wave function and therefore non-zero in the vacuum. This tail with exponential decay exists on both "electrodes", the tip and the sample. It is the overlap of the tails that leads to electrons tunneling between the tip and the sample. The overlap of the wave functions is proportional to the current and it can therefore be seen that the current decays exponentially as a function of distance in a tunneling junction. If the applied bias energy eV_{bias} is much smaller than the work function ϕ of the material, then $V_0 - E = \phi$ and a general term for the current I is therefore

$$I(z) = I(0)e^{-2\kappa z}, \tag{2.3}$$

where

$$\kappa = \frac{\sqrt{2m_e\phi}}{\hbar}, \tag{2.4}$$

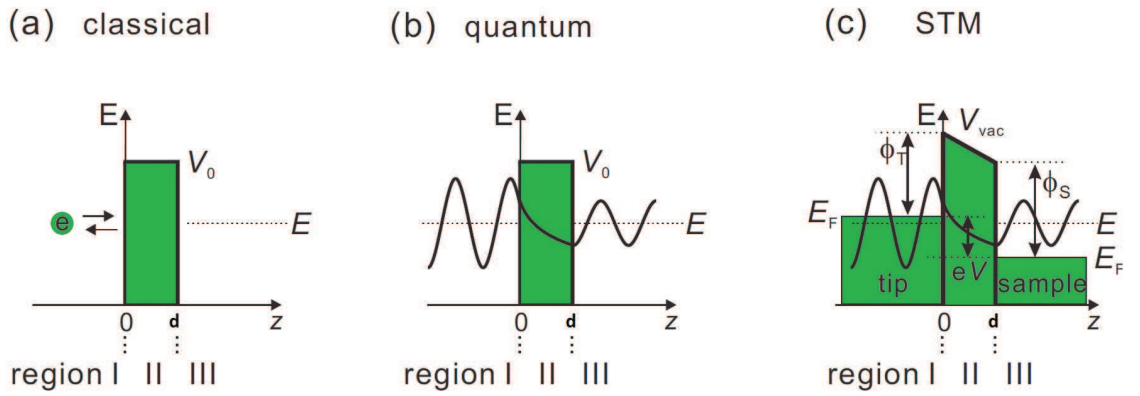

Figure 2.8: 1D Quantum tunneling of electrons. (a) Classical regime, an electron with an energy lower than the height of a potential barrier is forbidden to move across the barrier (b) Quantum regime, an electron has a certain probability to penetrate the barrier and tunnel through (c) Energy level diagram of sample and tip for applied bias voltage.

The current can be used by the feedback loop to measure heights z. However, the equation 2.3 is a simplified expression. According the Tersoff- Hamann model [45, 115], the tunneling current can be written in a more accurate form :

$$I(V) \propto \int_0^{eV} \rho_t(E - eV)\rho_s(E)T(z, E, eV)dE \tag{2.5}$$

where ρ_t , and ρ_s are the densities of states of the tip and sample, respectively, and all energies are taken with respect to E_f. $T(z, E, eV)$ is the transmission coefficient. If we assume a constant or weakly varying LDOS of the tip (ρ_t=constant) then, what is measured is actually a contour of equal Fermi level LDOS of the sample.This means that different materials or atoms will be displayed with different heights according to their LDOS at the Fermi level.

2.1.10 Scanning tunneling spectroscopy

A STM can also be used for spectroscopy to probe the electronic structure of the sample. There are different modes in which spectroscopy can be performed, in this thesis it is mainly done at a single point by placing the tip at the area of interest. Opening the feedback loop to maintain a constant distance between tip and sample, and then sweeping the bias while measuring the current I(V) can yield information about the LDOS at a given energy[26]. The theory of tunneling spectroscopy was developed in the 1960s especially by Bardeen [6]. In Bardeen's approach the Shrödinger equation is solved for each electrode separately. Here we shall assume that one of the electrodes is a sample and the other one is the tip, as implemented by Binnig and

Rohrer and theoretically shown by Tersoff and Hamann [114]. Under the assumption of a constant or weakly varying LDOS of the tip (ρ_t=constant), we obtain from differentiating equation 2.5 with respect to V:

$$\frac{dI(V)}{dV} \propto \rho_t(0)\rho_s(eV)T(z,E,eV) + \int_0^{eV} \rho_t(E-eV)\rho_s(E)\frac{dT(z,E,eV)}{dV}dE, \quad (2.6)$$

The first term shows the proportionality $\frac{dI(V)}{dV} \approx \rho_s(eV)$ while the second term provides a smoothly changing background signal in the case of small bias voltages. When assuming a constant tip DOS equals to the DOS at Fermi level (E_f). If we assume T to be constant in energy close to the Fermi level, the differential conductance $\frac{dI(V)}{dV}$ can be written as:

$$\frac{dI(V)}{dV} \propto \rho_s(eV)T(z), \quad (2.7)$$

This equation is a very important relation in STS. It gives information about the surface LDOS at given energy. Experimentally, the energy-dependent differential conductance is measured by stabilizing the tip above the desired location on the surface at specific feedback loop parameters (I and V). Then the feedback loop is switched off, to keep the tip-sample distance constant. While the bias voltage is ramped from the initial to a final value, the tunneling current is measured. Normally, the $\frac{dI(V)}{dV}$ is measured by either differentiating I(V) curves numerically or by means of a lock-in technique. All the $\frac{dI(V)}{dV}$ spectra shown in this thesis were recorded using a lock-in technique, The lock-in detection consists in adding a small voltage modulation of amplitude V_m and frequency ω to the applied bias voltage. Accurate a spectroscopic data depend crucially on the correct adjustment of the phase between the reference signal input and the signal input. This is done by retracting the tip, i.e. making the tunneling resistance infinitely large, adjusting the phase to maximum output, turning the phase by 90° and approaching the tip again. This procedure results in a maximization of the output of the lock-in signal to the resistive part of $\frac{dI(V)}{dV}$.

Apart from the point spectroscopy, the $\frac{dI(V)}{dV}$ can be carried out at every pixel of a topographic image. The complete set of data provides a stack of spectroscopic layers, often called $dI/dV(V,x,y)$ maps as shown Figure 2.9(a). This approach allows to study the spatial changes of differential conductance with applied bias voltages. That map can be recorded by following the ways: **1**. Opening the feedback loop at each point of the map and recording the full spectrum, however, this process takes more time to achieve. **2**. Recording the $dI/dV(V)$ signal at a well defined bias, often called the point $dI/dV(V,x,y)$ spectra map. In this working mode, the $dI/dV(V)$ map provide the information about spatial distribution of the DOS at a given energy.

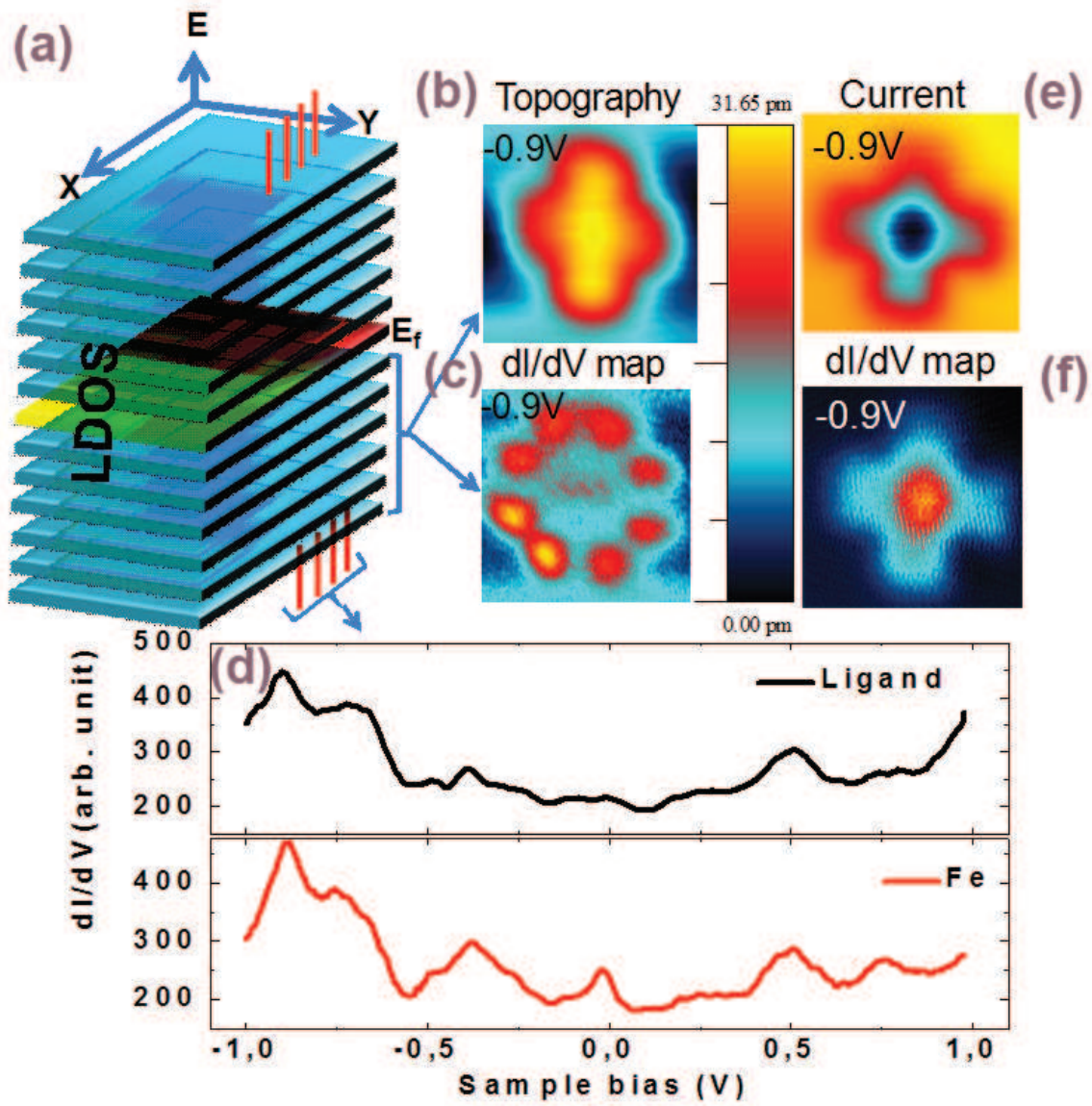

Figure 2.9: (a) STS carried out at every pixel of a topographic image, provides a complete set of "spectroscopic" layers. This 3-dimensional data space (two spatial dimensions (x, y) and energy E) can be explored in different ways.(b) Topography: the tip height Z is adjusted through a feedback loop to maintain a constant current I_{set} at a constant bias voltage V_{set}. Recording the tip height effectively maps out the height of the surface. (c) $dI/dV(V)$ map: the density of states at a fixed energy E is mapped as a function of position (x, y) on the sample surface. The $dI/dV(V)$ map can be done in two different modes: constant current(c) and constant height mode (f) (d)$dI/dV(V)$ spectrum: the density of states as a function of energy is measured at a single point on the sample surface.

This spatial distribution of the DOS includes the molecular orbital (MO) and the symmetry features.

Figure 2.9(d) shows the point spectrum on the iron and ligand of the iron phthalocyanine (FePc) molecule, respectively. From the $dI/dV(V)$ signal we can identify the MO and the corresponding energy. The tip scanned over the adsorbate and simultaneously record the constant current $dI/dV(V)$ map. Figure 2.9(b,c) shows the topography image and constant current $dI/dV(V)$ map of single Iron Phthalocyanine molecule on Au(111) surface. From the $dI/dV(V)$ map we can clearly see the highest occupied molecular orbital (HOMO) at -0.9 V and this relevant feature is also visible as a peak in the point spectrum. Under certain circumstances, it can be of advantages to record the $dI/dV(V)$ map in the constant height mode.To do so, the surface is scanned with an open feedback loop at a constant tip sample distance. The advantage of this method is that the tunneling channels of a chemisorbed molecule can be directly visualized [80]. Figure 2.9(e,c) shows clear differences in the localization of a high conductance region between constant current and constant height maps at -0.9 V. In the constant height map, a better signal to noise ratio is observed compared to the constant current map. The simple reason for that is the feedback loop remain open during the data acquisition.

2.2 Sample and tip preparation

In this study, the Au(111) and Cu(111) single crystals are cleaned in situ under UHV-conditions by repeated cycles of sputtering and subsequent annealing. The samples are sputtered for typically 20 min with 800 eV Ne^+ ions under an incidence angle approximately 50° and flux 3 μA. The annealing is performed at temperatures of 600-800 K depending on the materials. The pressure during the annealing is lower than 6×10^{-9} mbar. The quality of the pure metallic substrate was routinely checked by means of STM. This preparation results in atomically clean and flat samples with terrace widths larger than 100 nm can be obtained. The tips used to obtain the experimental results presented in this thesis were made with a polycrystalline tungsten (W) wires (diameter of 0.3 mm) etched chemically in sodium hydroxide solution (2M NaOH). After fixing the tip in the tip holder it was inserted into the vacuum chamber by a tip carrier plate. To remove the oxide film of the tungsten tip, it was heated to 1000 K for a short time by electron bombardment heating. Sputtering of the tip was subsequently performed by Ne^+ ion bombardment. Once inserted in to the STM, the tip is cleaned by field emission. The tip is retracted slightly from the tunneling range, a high voltage of a few 100 V is applied between the tip and sample until a field emission current is detected. To do so, the relatively high current heats the tip and makes the restructuring easier. After a field emission cleaning of the tip, the surface is dirty and it is necessary to move with the tip to other area of sample. Finally, the beginning of each experiment, the tip is checked to make sure that it is free of double tip features and that it images single atoms as spherical protrusions. Another way to get sharp tip apexes is soft indentation to the clean surface, which is a controlled way to tailor the tip apexes. In this process, the controlled dipping of the tip into the substrate is performed. So that the tungsten tip picks up atoms from the surface (it is coated with substrate material) and the local Joule heating leads to a re-shaping of the tip apex [49].

2.2.1 An example of STM and STS

Figure 2.10(a) shows an example of Au(111) single crystal surface. The Au(111) surfaces show a $22 \times \sqrt{3}$ reconstruction also called the herringbone reconstruction. The surface reconstruction for the Au(111) is driven by the surface energy minimization. The herringbone structure can be identied as the bright superstructure and the bright lines in the inset. It is caused by a non-uniform compression of the surface atoms, resulting in regions of fcc and faulted hexagonally-close-packed (hcp) regions

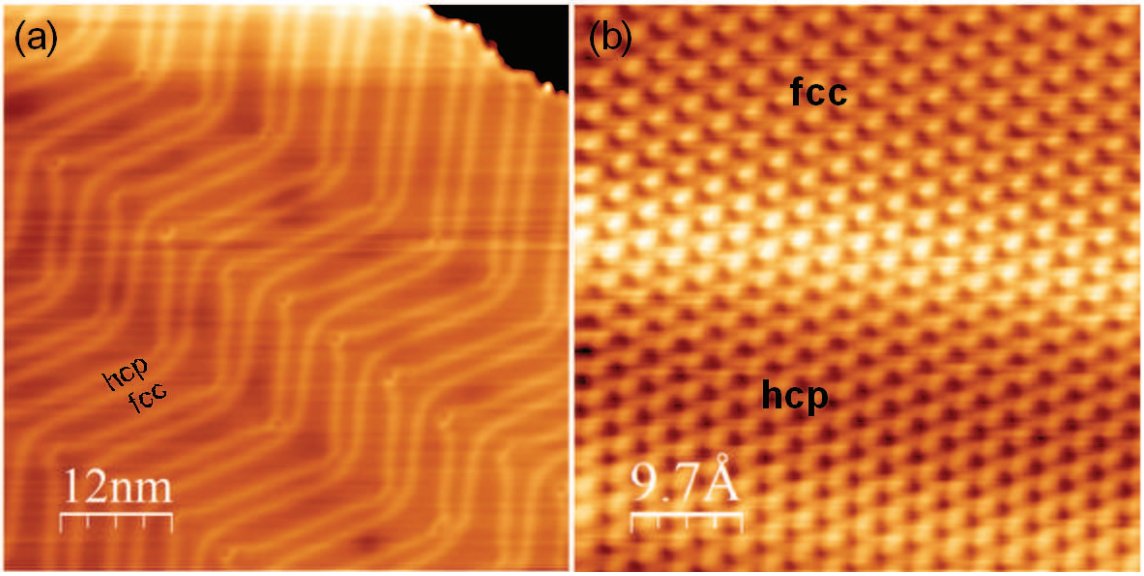

Figure 2.10: (a) The STM topographic image of reconstructed Au(111) surface (b) Atomic resolution over a pair of reconstruction lines of Au(111) surface

separated by the so called domain walls or linear discommensurations [95, 5]. Figure 2.10(b) presents an atomically resolved STM image over a pair of corrugation lines (bright regions) separated by a hcp region.

For the single point spectroscopic measurements, a spectrum is taken on the clean, bare substrate far away from a step edge to see if the surface state is detected correctly in the $\frac{dI}{dV}$ and the spectrum is otherwise featureless in the relevant energy range. Figure 2.11(a,b) shows an example of single point current versus applied sample bias spectrum and corresponding $\frac{dI}{dV}$ spectrum obtained by the lock-in technique. The clean Au(111) surface clearly showing the onset of the surface state close to -0.5 V. In this way, the tip status can be checked before starting any spectroscopic measurements. Otherwise, unexpected tip related signal appears over the energy range of interest. However, the spectrum has to be reproducible in each independent spectrum. Until then the spectroscopic features of the tip should be made acceptable. Indenting the tip into the surface often creates a hole in the surface indicating that the surface material is now attached to the tip. In the following, a novel way to deposit single atoms on metal surface is explored to tailor the tip apex. Another tip preparation method is vertical manipulation, where single atoms are transferred from tip apex to the surface [21]. In this way, the single atoms were deposited on to the substrate at desired locations [70]. Figure 2.12 shows an alternative method using vertical and lateral manipulations with STM tip to create letters 'KAZ'. To do so, the feedback loop was opened above a defect and impurity free areas of Au(111)

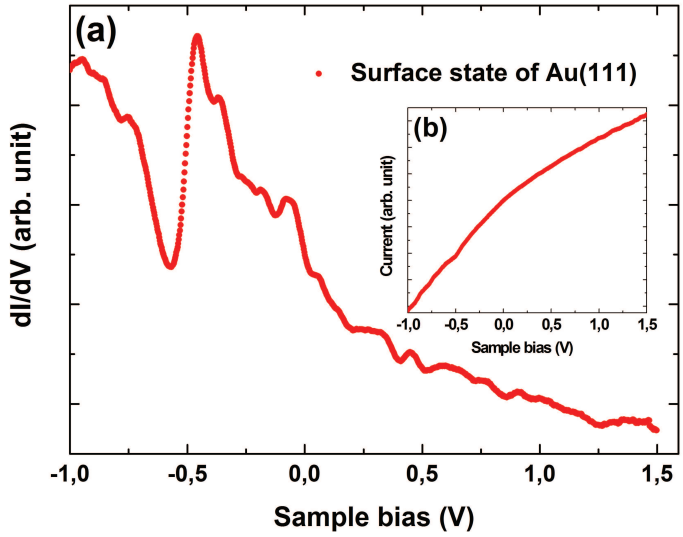

Figure 2.11: $\frac{dI}{dV}$ spectrum of a clean Au(111) surface clearly showing the onset of the surface state at -0.5 V. The remaining part of the spectrum is almost featureless except from a slope. This indicates a clean, metallic tip and metallic surface also.

surface and the tip held at a bias in the 100 to 200 mV range and finally retracted back to the tunneling positions. As a result a single gold atom is found at the contact site indicated by the red arrows in the Figure 2.12 (a,b). The atom by atom nano structure can be constructed by using lateral manipulation techniques [112, 80]. In this approach, The tip is placed on top of the atom to be moved, then the tip-atom interaction is increased by lowering the tip towards the atom. The typical current range to get such desired tip atom interaction is around $1 - 5 \times 10^{-8}$ A. Then the tip moves laterally under close loop condition. The speed of the movement is normally around 6-4 Å per second. Finally, the tip is positioned back to the initial scanning parameters and the outcome of the experiment is verified. However, there is a certain probability to have a single atom or clusters. After each contact the image profile or point spectrum has to be checked in order to identify the single atoms or cluster. Atoms can produce the localization of the two dimensional Shockley surface state at the Au(111) surface and can be identied from the scanning tunneling microscopy spectra. The localization gives rise to a resonance located just below the surface state band edge [74, 87] (see below).

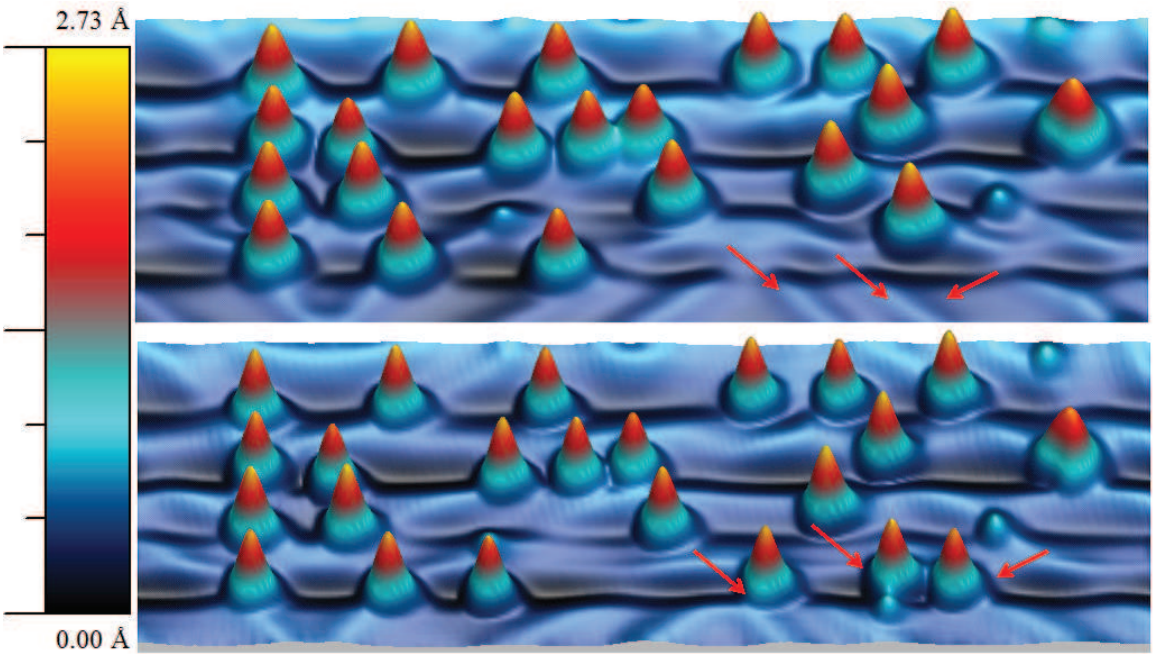

Figure 2.12: Alternative using vertical and lateral manipulations to create letter 'KAZ' by gold atoms on Au(111) surface.

2.3 The origin of Shockley surface states

Surface states are electronic states found at the surface of materials. They are formed due to the sharp transition from solid material that ends with a surface and are found only at the atom layers closest to the surface. The termination of a material with a surface leads to a change of the electronic band structure from the bulk material to the vacuum. In the weakened potential at the surface, new electronic states can be formed, so called surface states [43]. The periodicity of the crystal potential close to the metal surface is interrupted, therefore, the electronic wave functions are different from the Block wave functions of an infinite crystal. At a given potential, there are two qualitatively different types of solutions of Shrödinger equation [20]. The first type of states extends into the crystal and has Bloch character there. These states decay exponentially into the vacuum but extends into the crystal. The second type of states decays exponentially both into the vacuum and the bulk crystal. This type of solutions correspond to states, with wave functions localized close to the crystal surface. Such solutions are called Shockley or Tamm states [103]. These surface states host electrons trapped in the surface region but propagate along the surface, in that sense they form a quasi-two dimensional (2D) electron gas. The occurrence of surface states can be determined by the phase shifts of waves which are reflected by the bulk crystal and vacuum barrier, respectively. The round-trip phase accumulation has ϕ

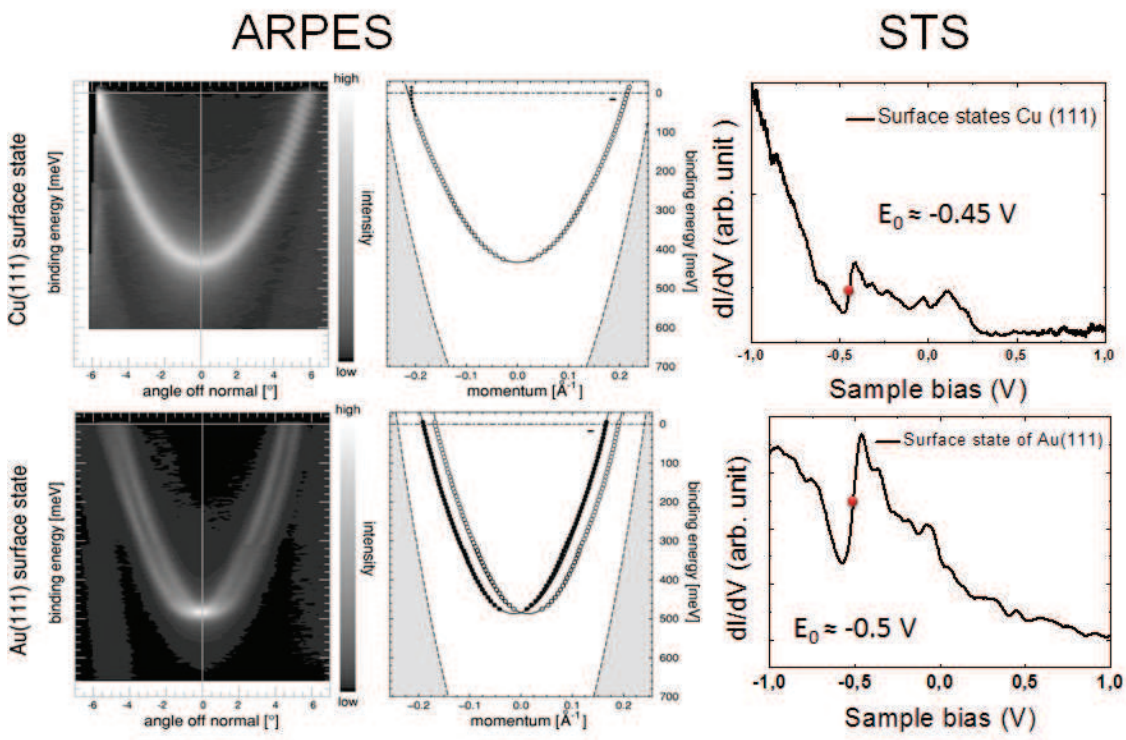

Figure 2.13: The Shockley surface states of the Cu(111) and Au(111) surface (left and middle).(from [91]). Typical dI/dV spectra taken on Cu(111) and Au(111) surfaces (T= 4.6 K).The differential conductance corresponds to the surface states E_0=-0.45 V for the Cu(111) and E_0=-0.5 V for Au(111), respectively (own data).

to be satisfied a Bohr-like quantization condition [107]:

$$\phi \equiv \phi_C + \phi_B = 2\pi nand \tag{2.8}$$

where n is an integer and ϕ_C and ϕ_B are the phase shifts of reflected waves. The single crystal of noble metal surfaces (Cu(111), Ag(111), Au(111)) host a surface state which has been extensively studied by means of angle-resolved photoelectron spectroscopy (ARPES) [60, 37, 91]. Figure 2.13 (left and middle) shows the dispersion of the Cu(111) and Au(111) surface states. The Cu(111) surface states have a parabolic dispersion of s-p character and appear at the $\bar{\Gamma}$ point of the the projected band structure obtained by ARPES [91]. The parabolic relation can be written as:

$$E(E_{||}) = E_0 + \frac{\hbar^2 k_{||}}{2m^*} \tag{2.9}$$

Where the free-electron mass m_e is replaced by an effective mass m^* to take into account the surface electron band structure E_0 is the bottom edge of the parabolic Shockley band. That surface states can also be observed by STS is shown in the Figure 2.13 (right). The step like onset (defined as the middle point of the rise) of the differential conductance corresponds to the surface state E_0=-0.45 V for Cu(111). On the contrary, The k splitting of the Au(111) surface state can be seen directly from the gray-scale plot in Figure 2.13 (lower left). The main reason of the k splitting is due to the spin orbit coupling of the Au(111) surface. The corresponding differential conductance of Au(111) surface state is shown in the Figure 2.13 (lower right). The bottom edge of the parabolic Shockley band surface state located close to -0.5 V, is in agreement with previous STS measurements [62].

2.4 Surface-State Localization by single adatoms

Shockley surface states at noble metal surfaces provide an ideal model system for electrons propagating in two dimensions (2D). An important fundamental effect associated with 2D surface states is the possibility of an adatom-induced localization of the surface state electrons [14]. The localized attractive perturbation of an atom on a 2DEG will always result in the appearance of a bound state [106] that can be investigate by STS. Bound state-related features have been first observed by Kliewer et al. [61], for the case of Mn atom on Ag(111), but only later has the existence of a surface bound state been unambiguously reported [87, 71]. Figure 2.14 (a) shows the STM image of individual Cu atom on Cu(111) surface. The faint wave pattern

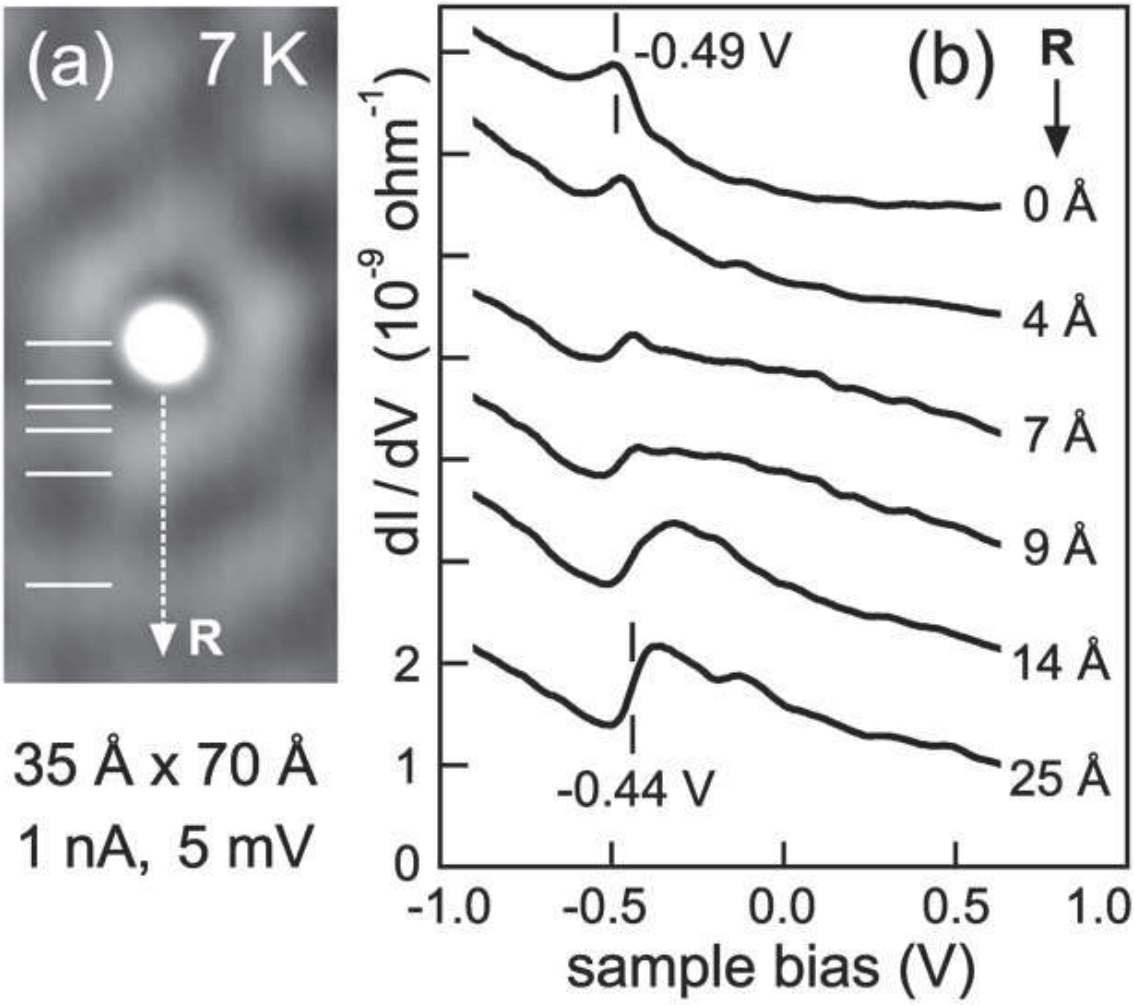

Figure 2.14: Experimental STM image and STS spectra. (a): Constant-current STM image of a single Cu/Cu(111) adatom (35×70 Å^2), the gray scale is enhanced to display the standing wave pattern of the surface state; horizontal white bars mark lateral distances, R, relative to the adatom where the differential tunneling conductance was measured at constant tip height. (b) Corresponding spectra measured with the tip positioned on top of the adatom (topmost curve) and at different lateral distances R as indicated (from ref [87]).

around the adatom arises from standing waves of the surface state. The corresponding spectra measured with the tip positioned on top of the adatom and at different lateral distances R as indicated in Figure 2.14(b). When the tip is moved laterally off the center of the adsorbates, all features continuously decrease in amplitude and vanish 10 Å away from the center. The bound state results from the coupling of the adatoms outermost orbital with the surface-state electrons and is broadened by the interaction with bulk electrons. Since this feature is observed in the same energy range for different atoms on noble metal surfaces. It is also unlikely that this resonance reflects an atomic orbital of the adsorbate, for example, the d state of impurity atoms. It must rather be related to the surface-state electrons of these surfaces, since the resonance occurs slightly below surface states regardless of the adsorbate.

2.5 Evaporation techniques

2.5.1 Molecular Evaporator

In this section we briefly present the molecular evaporator used in this thesis for depositing organic molecules on the metal surfaces. Figure 2.15 shows a home built molecular evaporator used to deposit organic compounds by resistive heating in ultra-high vacuum. The cylindrical ceramic crucible tube is held by a filament made of tantalum wire (thicknesses of 0.2 mm). The tantalum filament can be resistive heated through the two copper power feedthrough thus providing the electrical connection with the power supply. The temperature is varied by applying a current to a tantalum filament wound around the crucible. The temperature versus current calibration has been done using a K type (Chromel-Alumel) thermocouple introduced inside the crucible. The current through the tantalum filament was increased by steps of 0.1 and 0.5 A up to a value of 4.5 A. The temperature increases linearly with the intensity of the current through the filament as shown in Figure 2.16. The above calibration indicates that temperatures between 30°C and 550°C can be reached. During the molecular deposition, the well cleaned crystal is positioned above the resistive heated crucible filled with organic molecule. Monolayer or sub-monolayer deposits can be achieved in this way with typical exposition times of 5 to 20 seconds. The molecular evaporator has been tested by depositing 2,2'-Bipyrimidine on the Au(111) surface. The evaporation temperature of this molecule is close to 80°C. Figure 2.17 shows self-assembled monolayer of 2,2'-Bipyrimidine on the Au(111). A sub-molecular high-resolution STM image acquired at nitrogen temperature (77 K) clearly proves that the 2,2'-Bipyrimidine are flat lying on the surface. Two adjacent

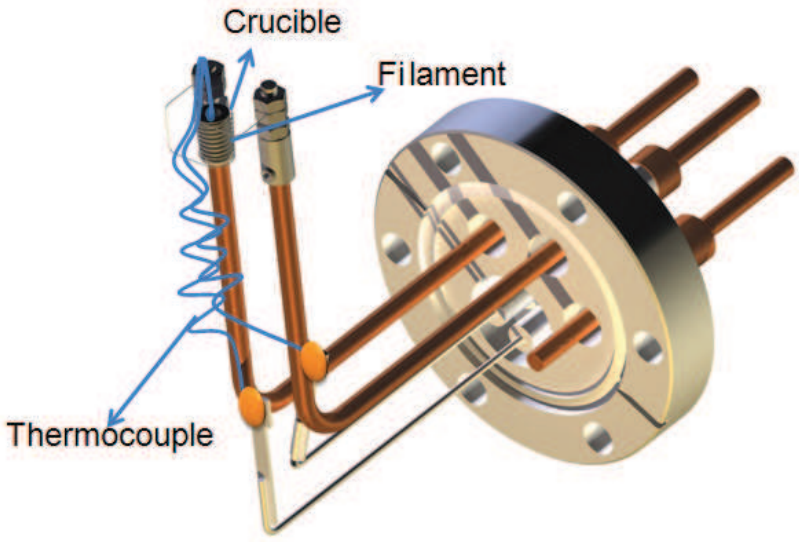

Figure 2.15: Our home built molecular evaporator

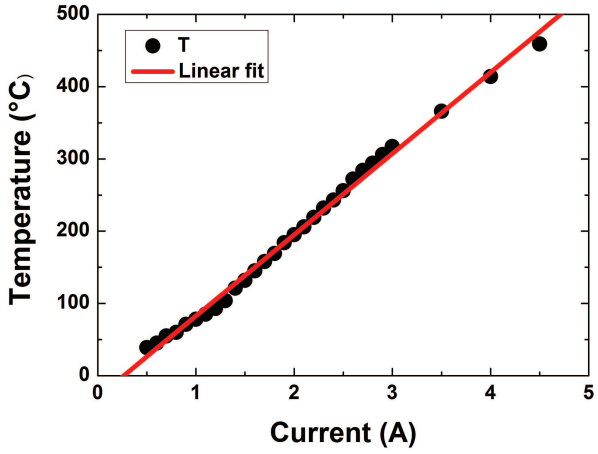

Figure 2.16: The temperature as function of the current intensity through the filament

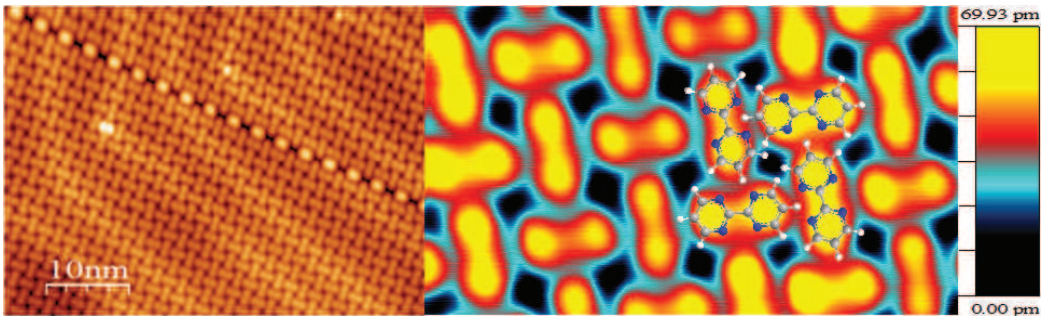

Figure 2.17: STM topographic image of the monolayer of 2,2'-Bipyrimidine molecules on Au(111) recorded at 77 K

2,2'-Bipyrimidine molecules are mis-oriented by $\pm 55°$ with respect to the $11\bar{2}$ crystal direction of Au(111) surface. The separation of two lobes of 2,2'-Bipyrimidine molecules are identical from the STM image correspond to the inter connected two carbon rings. In conclusion our home-built molecular evaporator can be employed in thermal sublimation or evaporation of different compounds with a variety of evaporation temperatures.

2.5.2 Metal Evaporation

In this section we describe the deposition set up used in our laboratory to the deposition of metal on metal surface in vacuum. For large amounts of metal atom, deposition is done by means of the Omicron electron beam heating evaporator (EFM) from a thoroughly outgassed metal rod. The EFM is designed for thin film growth and molecular beam epitaxy. Sub-monolayer and multilayer systems can be produced with evaporation rates varying from 1/10 monolayer per minute to over 1000 monolayers per second. Water-cooling ensures low background pressure (typically in the 10^{-10} mbar range) during evaporation and thus allows the growth of ultra-pure films. The precisely defined evaporant beam allows highly uniform deposition on the sample. The deposition area is determined by the distance from the source to the sample. The material to deposit is in the form of a metal rod, which is heated up by bombarding with an electron beam of typically a few mA at a energy up to 1 keV. This leads to the evaporation of a minute quantities from the top end of the rod. The coverage of metal atom on the surface can be calibrated by the STM. Figure 2.18(a) shows after evaporation of about 0.7 monolayer (ML) of cobalt onto Cu(111) surface at room temperature. The cobalt forms triangular shape nanoislands two-atomic-layers in height relative to the Cu surface, whose lateral sizes vary typically between 5 and 30 nm.

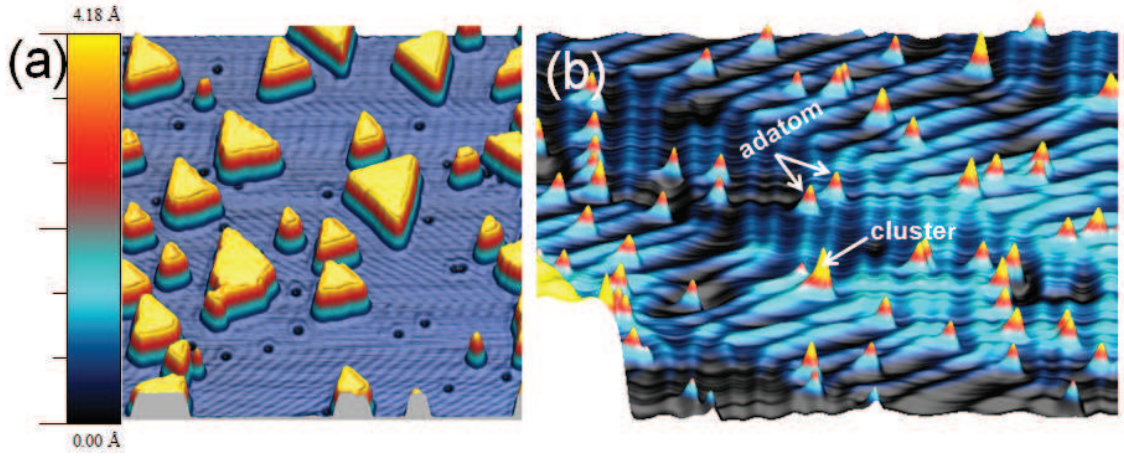

Figure 2.18: (a)STM topographic image of two-atomic-layer high Co nanoislands on Cu(111).(b) Topography of individual Iron atoms on a Au(111) surface at 4.5K,

On the other hand to get individual atoms on metal surfaces, the deposition must be done at a low sample temperature. In this way, the kinetic energy of incoming atoms gets lower and does not sufficient to overcome the diffusion barrier at the surface. Deposition of small amounts of atoms can be done by a home made evaporator. The evaporator is based on the principle of Joule heating. It consists of a wire of the desired elements, for example high purity Fe, Ni, Co, which is wound around a tungsten spiral. The current passing through the tungsten wire heats the points of contact between the wire and tungsten spiral and a small amount of the chosen element is then evaporated. Figure 2.18(b) shows after evaporation a small amount of Fe atoms on the Au(111) surface at low temperature. Most of the Fe is in the form of individual atoms except a few Fe clusters also present in the STM image.

Chapter 3

The adsorption structure and electronic properties of 1,2,4,5-Tetracyanobenzene (TCNB) on Au(111)

3.1 Introduction

Organic molecule based heterostructures display interesting electronic and optical properties making them promising candidates for many technological applications, such as organic light emitting diode (OLED), organic field effect transistor, solar cell and organic magnet [90, 75, 109, 35]. In order to understand the electron transport in hybrid metal-organic devices it is important to address the issue of the contact between a conductor and a molecule which is a decisive factor for the quality of these nanoscale devices since it modifies the properties of the molecule and therefore its functionalities. The performance of these devices depends critically on the energy barriers that control the carrier transport between layers, energy barriers that are determined by the relative alignment of the molecular levels at metal/organic interfaces [98]. However, the underlying metal substrate also plays a key role for the formation of supra molecular organization at surfaces. STM/STS, with its unique capability to image structures with sub-molecular resolution, has offered a great deal of information on the local structure, chiral organization, and clear fingerprint of electronic and magnetic properties of organic molecules on metal surface. In this chapter, the self-assembling of 1,2,4,5-Tetracyanobenzene (TCNB) molecule on the Au(111) surface is discussed. Not only the structural formation but also the electronic properties of TCNB on Au(111), as probed by STM/STS, will be presented.

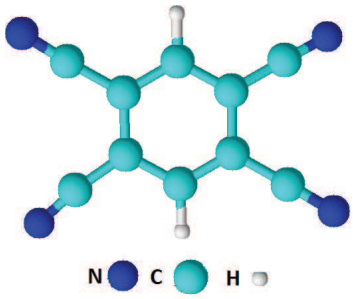

Figure 3.1: The molecular structure of TCNB molecule.

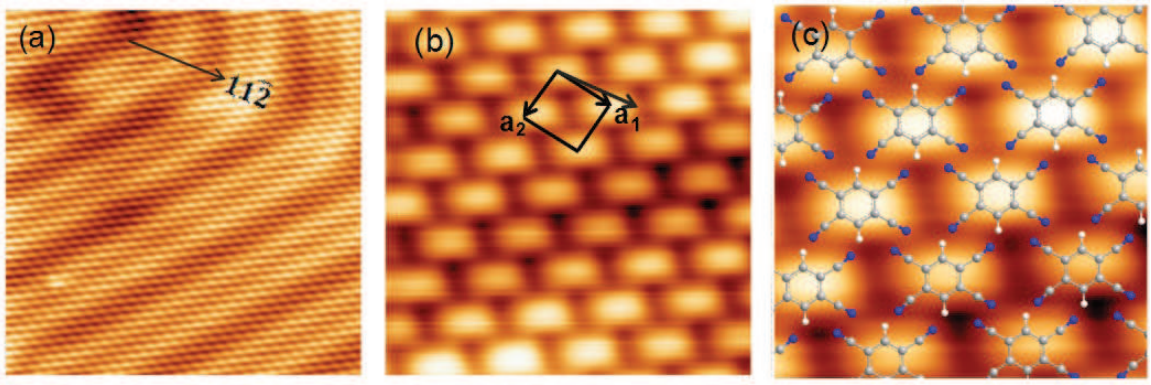

Figure 3.2: (a)STM topographic image of a self-assembled monolayer of TCNB (31×31 nm). The reconstructed Au(111) surface with herringbone pattern is visible through the molecular island. (b) Zoom with intra-molecular resolution in a TCNB (5×5 nm). The unit cell of the self-organized TCNB exhibits a rhombic symmetry. The length of vectors $a_1 \approx a_2 \sim 0.8$ nm, (c) Adsorption model of TCNB on Au(111). The formation of the C≡N–H-C hydrogen bond.(I=0.1 nA, V=-1 V)

3.2 Self-assembling of acceptor TCNB molecules on Au(111)

The TCNB molecule is a well known π acceptor molecule. It is also a basic molecular unit commonly used for the synthesis of phthalocyanine derivatives. The chemical structure of TCNB is outlined in Figure 3.1. The main features that determines the acceptor functionality are the four cyano groups and a central benzene ring. Its electron affinity is 2.20 eV, smaller than for tetracyanoquinodimethane (TCNQ) for which it is found to be 4.2 eV [59]. Thus, TCNB is a weaker electron acceptor than TCNQ.

TCNB was evaporated from an alumina crucible onto the pristine Au(111) surface held at room temperature. Figure 3.2 shows high resolution STM images of the TCNB monolayer. The fact that the zigzag reconstruction is still visible despite the monolayer deposition is indicative of the weak interaction of the TCNB molecules with the substrate. The molecular structure forms a rhombic unit cell with unit vectors

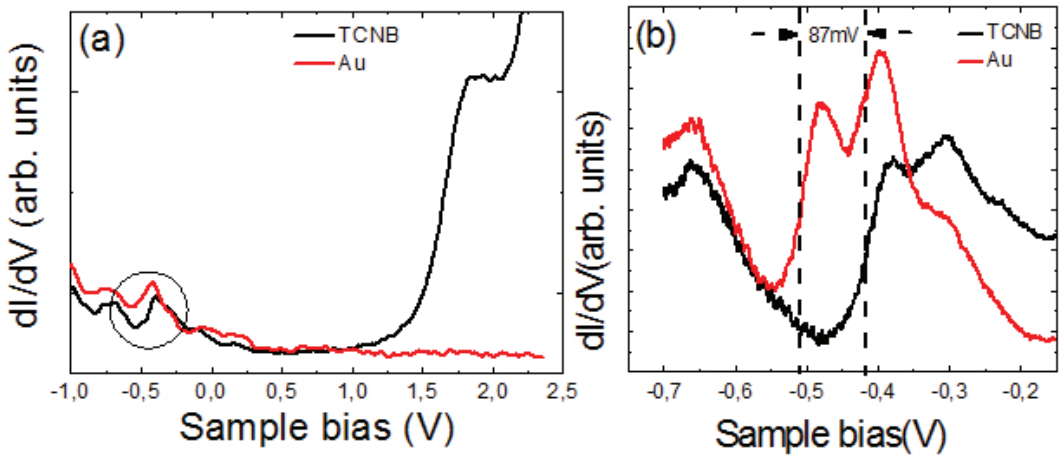

Figure 3.3: (a) large bias range STS spectra taken on clean Au(111) (red curve) and TCNB monolayer (black curve).(b) the shifts of the Au(111) surface state (tunneling parameters prior to opening the feedback loop: V = 0.6 V, I = 0.5 nA, Vrms = 15 mV).

$a_1 \approx a_2 \sim 0.8$ nm, with an angle β between the two vectors $\sim 87°$ (Figure 3.2(b)), vector a_1 runs at angle of $\theta \sim 16°$ with respect to the $[11\bar{2}]$ surface direction. Figure 3.2(c) shows the corresponding structural model of TCNB molecules on Au(111) surface. In this model, nitrogen atoms point towards the hydrogen atoms of the neighboring TCNB molecules. The average distance between the N atoms and the H atoms is ~ 2.5 Å . It is within a typical range of intermolecular hydrogen bonds [66]. The self-assembled structure is stabilized by C≡N–H-C hydrogen bond (Figure 3.2(c)). The other two nitrogen atoms are positioned above the Au atoms of the substrate and keep the TCNB flat on surface.

In order to understand the electronic properties of TCNB monolayer on Au(111) surface, we have performed STS measurements at the TCNB/Au(111) interface. Figure 3.3 (a) shows the differential conductance spectrum measured on top of a TCNB monolayer in comparison with the spectrum taken under the same conditions on the bare Au(111) surface. The TCNB monolayer spectrum shows one pronounced resonance located at 1.8 eV for the lowest unoccupied molecular orbital (LUMO) which is not observed on the spectrum of the pristine Au(111) surface. Furthermore, it is found that the Shockley state of the Au(111) surface is shifted upwards by 87 meV due to the TCNB monolayer as shown in the Figure 3.3 (b). The formation of similar interface states upon adsorption of organic and inorganic species has been reported for various systems and manifests itself by shifts of the metal surface state as large

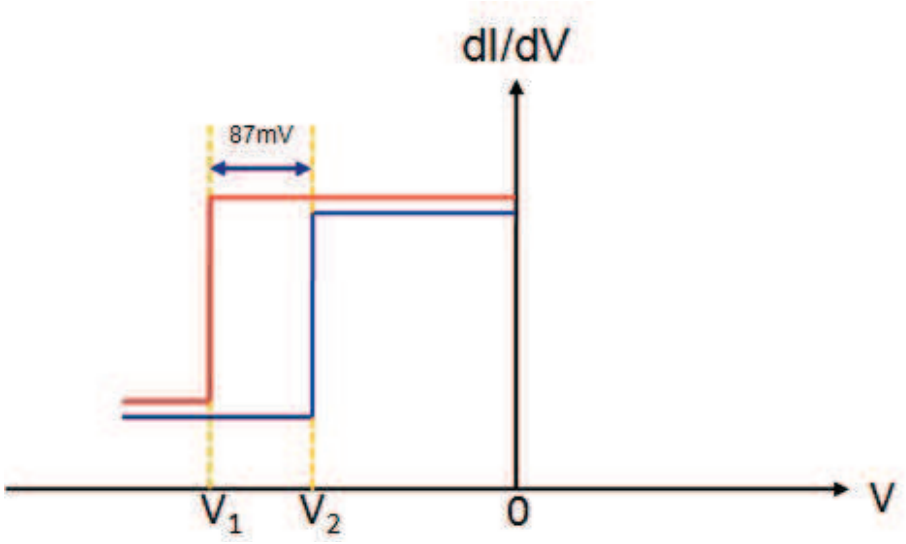

Figure 3.4: The model of density of states of a two-dimensional system (Au(111) surface) and metal/ organic interface, where the V_1 and V_2 are represents the energy position of the surface state of Au(111) and the shift of the surface states due to the TCNB layer

as 600 meV [92, 96, 47]. The shift of the Au(111) surface state upon TCNB adsorption of 87 meV is comparably small and leads to an adsorption energy per surface area similar to that of krypton on Au(111) surface [127]. Experimental physisorption energies on noble metal surfaces can be obtained using the linear relation between the shift of the Shockley surface states and the physisorption energy per surface area [127, 52]:

$$D \approx \delta E_b(ss), \tag{3.1}$$

Where the D is the potential depth at the equilibrium position and the $\delta E_b(ss)$ is the Shockley state binding energy shift. The physisorption energy per surface area according to the equation 3.1 is 9 meV/Å^2. Since the average area per TCNB molecule as obtained from the STM topographic images equals $\sim$ 60 Å^2, the physisorption energy per molecule amounts 0.5 eV. The shift of the Shockley surface state is due to the modifications of the image potential (surface work functions) by the dielectric medium placed on the metal surface [51], or to surface state depopulation [82] due to charge transfer between the surface and the molecular layer. Since TCNB molecules are only physisorbed on the Au(111) surface, we do not expect a charge transfer processes between the surface and the molecular layer. Additional evidence is obtained from the spectra of Figure 3.3 (b).

Lets recall that the noble metal surfaces are an experimental realization of a quasi-two-dimensional electron gas (2DEG). Starting from the fact that the density of states of a 2DEG is constant and equal to dI/dV = $\frac{m^*}{\pi\hbar^2}$ as shown in Figure 3.4.

Name	References	The shift	Charge per molecule	Electron affinity
TCNE	[124]	-	-	2.03 eV
TCNB		87 mV	0.06 e	2.2 eV
TCNQ	[56]	150	0.2 e	4.23 eV
TCNP	[120]	130 mV	0.13 e	4.7 eV

Table 3.1: Different acceptor Cyano families are physisorbed on Au(111) surface.

Since the surface electron effective mass m^* of Au(111) is well known and equal to m^*=0.28 m_e [39], the amount of charge per unit of surface can be obtained by integrating the area below the Fermi level (0 eV). For the Au(111) surface state with a band bottom located at -490 mV (V_1 in the Figure 3.4) a charge of 0.0057 eÅ^{-2} is obtained. The 87 mV shift by the TCNB layer (V_2 in the Figure 3.4), reduces this value to 0.0047 eÅ^{-2}. Since the average area of a TCNB molecule, as obtained from the STM topography equals $\sim$ 60 Å^2, the average charge transferred from the surface to one TCNB molecule is 0.06 e almost negligible. Therefore, we conclude that the TCNB remains nearly neutral on the Au(111) surface. The shifting of the surface state as a result of modified image potential or surface work functions, is also known for other CN ligands on Au(111) surfaces [120, 56]. In all cases, the shift of the surface state is expected to be accompanied by an increase in the electronic effective mass m^*. Further measurements of angle resolved photo-emission spectroscopy would be necessary to provide a final proof of this argument.

Table 3.1 summarizes the results for different acceptor molecules from the TCNX family adsorbed on the Au(111) surface. The table shows that four different molecules with a same CN end-group are physisorbed on Au(111) surface. The average charges transfers from the metal surface to the molecules are small even though it is a strong acceptor character like Tetracyanoquinodimethane (TCNQ). In fact, the TCNB molecules have a weaker acceptor character than the TCNQ and TCNE molecules which are the strongest acceptors in this family. Therefore, the nearly neutrality of the TCNB molecules on the Au(111) surface is a reasonable conclusion.

In order to gain insight into the electronic properties we have performed gas phase calculation of TCNB molecules. The computation has been carried out by Anis Amokrane within a collaboration with Mauro Boero at the Institut de physique et chimie des matériaux de Strasbourg (IPCMS). These calculations were done by first-principle molecular dynamics [15] within the density functional theory (DFT) formulation of quantum mechanics [64] by means of CPMD package. The Beckes exchange functional [10] and the Lee-Yang-Parr one [69] for the correlation (BLYP)

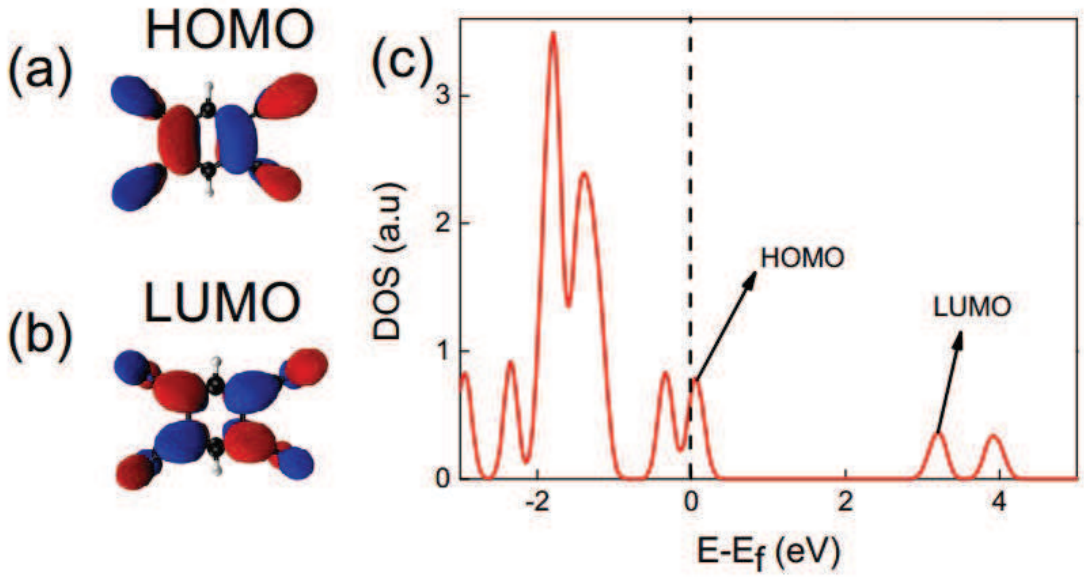

Figure 3.5: (a) HOMO and (b) LUMO for the ground state of TCNB with isovalue 0.03 $e/\mathring{A}^3$. (c) Density of states of the TCNB molecule obtained by gas phase calculation.

was complemented with the Grimmes empirical Van Der Waals corrections [42]. Valence electrons were treated explicitly and expanded in a plane-wave basis set with an energy cut-off of 70 Ry. The valence-core interaction was described in terms of norm-conserving pseudo-potentials [116, 38]. The calculation has been performed for a neutral TCNB molecule since neutrality has been observed experimentally on Au(111). However, DFT does not yield the precise HOMO and LUMO energy location with respect to the Fermi level, but the major trends for the TCNB can be discussed. Figure 3.5 shows the electronic density of states (DOS) on the TCNB molecule as obtained upon diagonalization of the Kohn-Sham Hamiltonian. The HOMO was set at the Fermi level (0 eV), while the LUMO is close to 3 eV. The LUMO main feature corresponds to the shoulder at 1.8 eV in the experimental dI/dV spectra of the TCNB layer on Au(111) and thus, the calculated HOMO-LUMO gap is in good agreement with the 3.3 eV gap measured by STS. The charge density isosurfaces corresponding to LUMO and HOMO obtained from the DFT calculation of the free molecule are in good agreement with previous calculations [17].

3.3 Conclusions

To summarize, we present experimental results on the TCNB/Au(111) interface obtained from STM/STS combined with DFT calculations. Adsorption of the organic

electron acceptor TCNB on a Au(111) surface leads to a weakly physisorbed state, in which the molecules retain their neutral state and the self-assembled structure is stabilized by the formation of the C≡N–H-C hydrogen bond. The calculation also confirms that the HOMO/LUMO gap is comparable with experimental values. The shift of the Au(111) surface state upon adsorption of TCNB might be a result of work-function changes and/or image potential modifications. It is then expected that TCNB still maintains its acceptor character in the adsorbed state, even though the 0.06e charge from the surface is negligible. As will be shown in the next chapter it may become charged upon co-adsorption with transition metal ions that exhibit donor character. For all these reasons, TCNB is a model system to study the metal organic coordination bond formation on the Au(111) surface.

Chapter 4

Steric and electronic selectivity in the formation of Fe-TCNB complexes on Au(111): from geometric confinement to bond formation

4.1 Introduction

The TCNX (X= E, Q, B) series forms a rich variety of structures on the metal surface where each unit can form multiple bonds to metal atoms due to the four cyano-head-groups. The TCNQ molecule is the most studied molecule of this family due to its strong π-acceptor properties. Furthermore, TCNQ can be coordinated with transition metal ions for preparing a supra molecular spin networks on metal surfaces because large local superexchange interactions are expected between the high spin state of the metal ions and organic spin carriers [1, 25, 35]. However, TCNE and TCNB are potentially interesting as well [124, 2] for chain and network formation. Studies of metal-organic coordination at surfaces under UHV conditions, therefore, could offer the advantages of high control over surface composition as well as capabilities for structural determination with atomic/molecular resolution, and determination of magnetic properties. Self-assembly of atoms and molecules is often achieved either sequentially by exposing to metal atoms a previously deposited molecular monolayer or co-deposition of metal atom and organic molecules on the metal surface at room temperature or higher [84, 102]. The surface temperature is then a crucial parameter for growing metal organic complexes on metal surface in the UHV conditions, it allows to large extent the kinetics of complex formation on metal surfaces. In the

kinetic low temperature regime growth may lead to metastable structures i.e. the self assembly process cannot take place since metal organic entities have not sufficient energy to overcome diffusion barriers on the surface. Intermediate structures are particularly important for the metal organic complex formation since they constitute the link between the initial and final states. LT-STM/STS allow us to study in controlled manner the evolutions from the metastable metal-organic complex to the final stable structures. In this chapter, we examine the structural and electronic properties of self-assembled complexes grown sequentially by exposing to Fe atoms a TCNB monolayer deposited on a Au(111) surface. It is found that the Fe atoms and the electron acceptor molecules first form an ordered metastable intermediate. By further activating the reaction, a full rearrangement of the molecules and the Fe atoms finally leads to the formation of ordered magnetic monomer complexes, stabilized by the coordination bonds with the molecules. The electronic properties are examined by STS along the reaction path.

4.2 Early stage of Fe(TCNB)$_4$ formation on Au(111)

Starting from the TCNB monolayer on Au(111), small domains of Fe-(TCNB)$_4$ monomers are obtained by carefully dosing Fe atoms from a filament evaporator. During this operation, the sample was kept at a temperature <100 K on the cold shield of the STM. The new Fe-(TCNB)$_4$ domains are embedded in the TCNB mother-phase and have to comply with strict boundary conditions as shown in the Figure 4.1. It is worth noting that the new Fe-(TCNB)$_4$ phase occupies the same surface area as the mother phase. A cell of 4 TCNB molecules occupies 1.96 nm^2 in both cases. As is shown in Figure 4.1 (c, d), the geometrical confinement also induces the chirality of the Fe-(TCNB)$_4$ entity. Inside such a confined domain, adjacent Fe-(TCNB)$_4$ units possess the same chirality, although mirror-symmetric, clockwise and anticlockwise Fe-(TCNB)$_4$ domains are found on the surface. The small domains of either chirality are slightly miss-oriented by 17° with respect to each others, behaving like rafts embedded in the TCNB mother phase. The STM data yield a unit cell parameter of $\vec{b_1} \approx \vec{b_2} = 1.4 \pm 0.2$ nm with an angle $\beta = 86^o$ and the azimuthal angle θ between vectors $\vec{a_1}$ and $\vec{b_1}$ is close to 20°. Figure 4.1(b) shows the model structures of the Fe-(TCNB)$_4$ metastable intermediates on Au(111) based on the unit cell distances and angles measured in the STM. In this model, we assume that metal centers reside on energetically favorable hollow sites of the Au(111) surface. Four molecules arrange around one Fe atom with their benzene rings adsorbed mainly on bridge sites of the

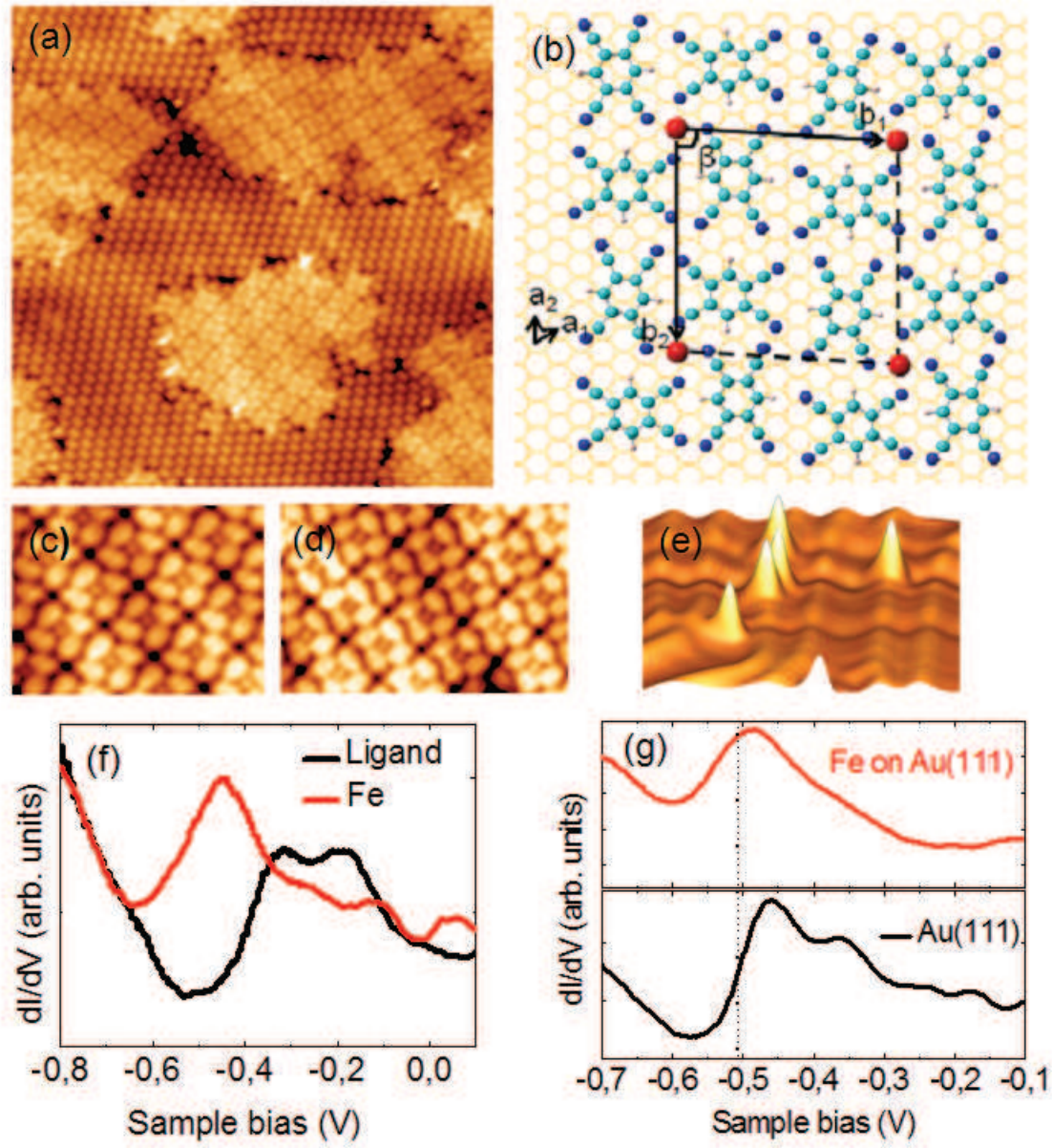

Figure 4.1: (a) STM image of Fe-$(TCNB)_4$ confined phase on Au(111) surface (30×30 nm, I=0.2 nA, V=1 V). Two mirror-symmetric domains mis-oriented by ±17° with respect to each others. (b) The model structure of Fe-$(TCNB)_4$ confined phase on Au(111). The structural model is based on the unit cell distances and angles measured in the STM. (c, d) The magnification of clockwise and anticlockwise Fe-$(TCNB)_4$ domains. (f) dI/dV spectra taken at 4.6 K on the atom and on the ligand. For comparison, (e) the corresponding dI/dV spectra on of isolated Fe atoms on the bare Au(111) surface.

substrate. In this configuration the N-Fe coordination bonds is estimated to 2± 0.1 Å and the Fe-N-C bond-angle is close to 120°. The other two "uncoordinated" cyano groups point towards the underlying Au atoms of the Au(111) surface. The substrate $\vec{a_1}$, $\vec{a_2}$ and over-layer $\vec{b_1}$, $\vec{b_2}$ lattice vectors for a given azimuthal orientation θ are related through a transformation matrix C [50]: $\begin{bmatrix} b_1 \\ b_2 \end{bmatrix} = [C] \begin{bmatrix} a_1 \\ a_2 \end{bmatrix} = \begin{bmatrix} p & q \\ r & s \end{bmatrix} \begin{bmatrix} a_1 \\ a_2 \end{bmatrix}$ where the matrix coefficients are defined by the following relations:

$$p = b_1 sin(\alpha - \theta)/a_1 sin(\alpha) \tag{4.1}$$

$$q = b_1 sin(\theta)/a_2 sin(\alpha) \tag{4.2}$$

$$r = b_2 sin(\alpha - \theta - \beta)/a_1 sin(\alpha) \tag{4.3}$$

$$s = b_2 sin(\theta + \beta)/a_2 sin(\alpha) \tag{4.4}$$

The metastable intermediate Fe-$(TCNB)_4$ complex superstructure can then be expressed by the commensurate matrix: $\begin{bmatrix} 4 & 2 \\ -4 & 6 \end{bmatrix}$

The dimension of the unit cell is unchanged when going from $(TCNB)_4$ to Fe-$(TCNB)_4$. Since there is a surface confinement of the molecules and a repulsive interaction between them (stemming from the uncoordinated CN-CN interactions), the only possible way to accommodate the Fe atoms is by rearranging the TCNB molecules (see Figure 4.1(a)). Trenches form between the Fe-$(TCNB)_4$ units and a hole appears in the middle of the unit cell. According to purely geometrical considerations, this could be an example of side-on coordinated complexes [18] as opposed to the normal end-on coordination (see below). However, the fact that the side-on complex requires higher activation energy than the end-on complex, makes this option unlikely in our case. Substrate mediated electrostatic interaction between molecular structures and distant metal atoms can be excluded as well on the basis of geometrical bond length arguments [126]. The Fe-N bond length about 2.1 Å obtained from the STM image is too short to be of electrostatic origin [67].

To better understand the impact of the geometric confinement on the electronic structure, dI/dV spectroscopy was performed at various positions above the monolayer. Figure 4.1(f) shows, the STS spectra taken above the Fe in the metastable Fe-$(TCNB)_4$ complex, the Fe atom is subject to a so called bound-state arising from the localization of the Au(111) surface state (see chapter 2). On the ligand side, the Shockley state observed above the TCNB molecule shows the same upwards shift as the one observed on the pristine TCNB monolayer (see chapter 3).

In general, if an atom is adsorbed on a surface, three qualitatively different cases of adsorption may occur: ionic, neutral and metallic [93, 4], which follow respectively from a full electron charge transfer, no charge transfer, or a partial charge transfer between the surface and the adatom. For the adsorption of transition metal atoms on a metal surface, we expect a metallic adsorption [48]. As we discussed in the previous chapters, the Au(111) surface is characterized by a 2DEG-like surface states. A metal atom adsorbed on this surface produces a local positive potential leading to a localization of 2DEG called bound state (see chapter 1). Experimentally, the appearance of bound state has been measured in different system by STS [63, 87, 71]. Figure 4.1(e, g) show a high resolution topography of Fe adatoms on the bare Au(111) surface as well as the corresponding dI/dV spectra, showing the typical onset of surface states at -0.5 eV, and the surface state localization on a single Fe atom. The bound state of Fe in Fe-$(TCNB)_4$ intermediates is remarkably similar to the one found above Fe on a bare Au(111) surface. Since the Shockley states are extremely sensitive to charge transfer [127] this result indicates that the TCNB molecules are virtually in the same electronic state as before the Fe adsorption. Therefore, the preservation of the surface state as well as the apparition of a bound state on the Fe atom speaks against Fe participating in metal-organic coordination bonding. Instead, the Fe adatom rather acquires a partial charge through interaction with the substrate. Therefore, the Fe adatom is still in a metallic state.

4.3 The formation of Fe(TCNB)$_4$ coordination structures on Au(111) at room temperature

By increasing the concentration of Fe atoms up to a ratio of 1 Fe atom for 4 TCNB molecules, the whole TCNB domains transform into the new phase. Figure 4.2(a) shows large domain of new Fe(TCNB)$_4$ monomers. The system which was trapped in the original, metastable state has now evolve towards the equilibrium Fe(TCNB)$_4$ complex phase. The full transformation may take an hour. However, the transformation can be stimulate by annealing the sample at 400-450 K. The Fe(TCNB)$_4$ domains are oriented along the shorts Fe-Fe direction approximately 15° from the substrate $[11\bar{2}]$ direction as marked by black arrows. Again, homo-chiral and mirror symmetric Fe(TCNB)$_4$ domains are present on the surface as shown Figure 4.2(c,d). Each individual complex is now occupying more space than in the previous confined phase.

The STM data yield a unit cell parameter of $\vec{a_1} \approx \vec{a_2} = 1.5 \pm 0.2$ nm with an angle β close to 90°. According to the epitaxial relation between the substrate and the adlayer lattice, a commensurate superstructure can be expressed by following matrix: $\begin{bmatrix} 4 & 2 \\ -5 & 6 \end{bmatrix}$ The Fe-N bond is estimated to be 2.0 ±0.1 nm from the model and the STM topography, in good agreement with similar metal-cyano-bonds [117]. The Fe-N-C bond-angle is close to 180°. The formation of the Fe(TCNB)$_4$ monomer has major consequences on the vertical position of the Fe atom as can be seen by comparing the STM topographic line profiles across the Fe atom of metastable Fe-(TCNB)$_4$ and stable Fe(TCNB)$_4$ monomer shown in the Figure 4.3. For the metastable Fe-(TCNB)$_4$, in the absence of bond formation with the surrounding ligands, the Fe atom appears as a deep in the line profile. In the case of the true Fe-(TCNB)$_4$ monomer, after the fourfold coordination with the cyano-groups, the Fe atom appears as a protrusion, due to the partial decoupling of the atom from the substrate. In both cases, the ligands are imaged at approximately the same height and can be used as references. However, we can not exclude the electronic effects in the image, because the contrast in STM is a convolution of geometric contour and lateral variations in the charge density of surface structure, which is directly related to the electronic properise.

Similar fourfold coordinated transition metal windmill complexes [84, 4, 63] are known to induce a large variety of electronic and magnetic properties. For example the Fe-(TPA)$_4$ arrays on Cu(100) have been found to possess high spin and exceptional

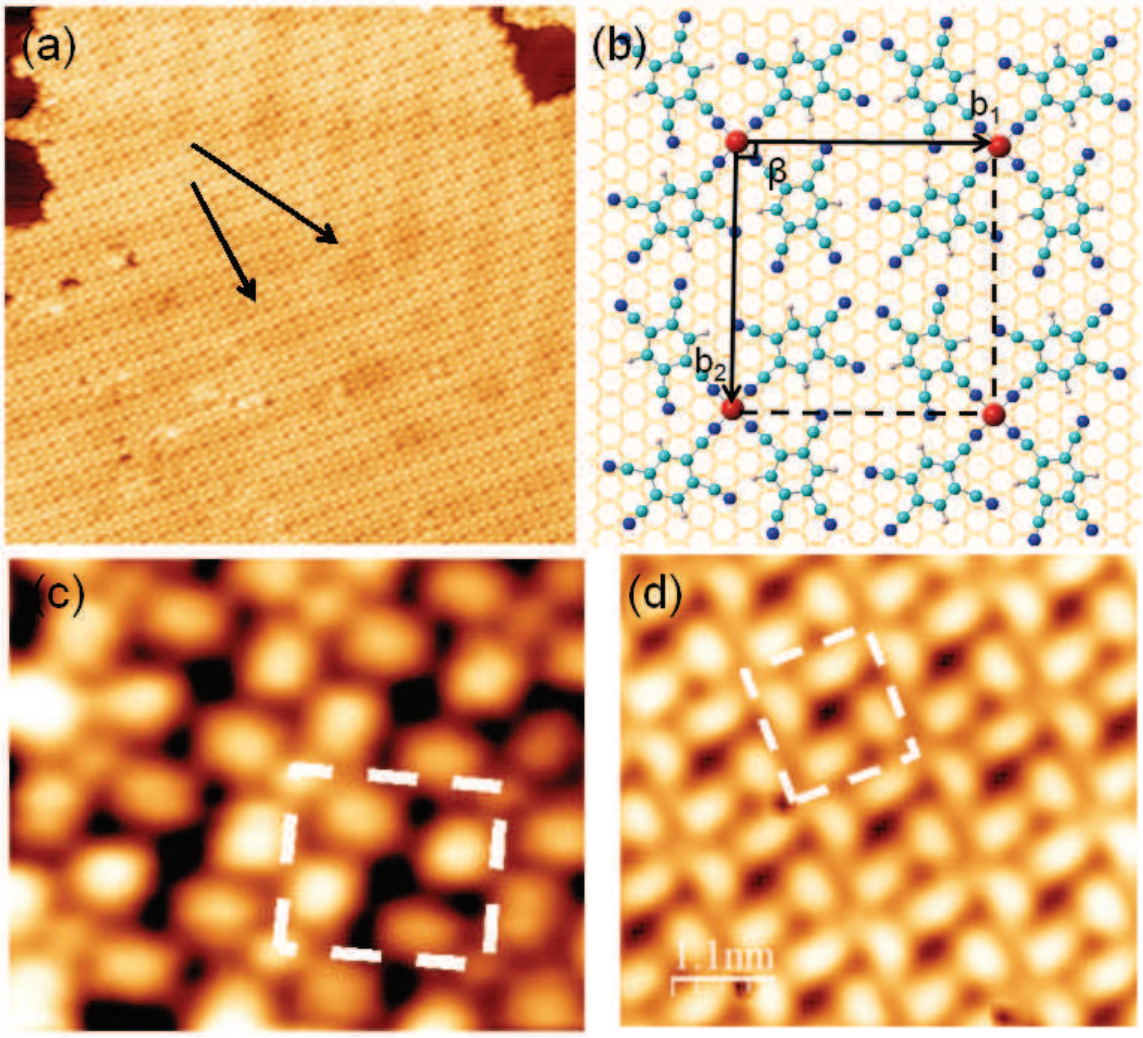

Figure 4.2: (a) The STM image (size 40×40 nm^2, tunneling parameters, V=1.5 V, I=0.2 nA) of Fe(TCNB)$_4$ monomer on Au(111) surface. The Fe(TCNB)$_4$ domain oriented along the shorts Fe-Fe direction approximately 15° from the substrate [11$\bar{2}$] direction as marked by black arrows. (c, d) The high resolution images of homo-chiral and mirror symmetric Fe(TCNB)$_4$ domains. The unit cell parameter of $\vec{a_1} \approx \vec{a_2} = 1.5 \pm 0.2$ nm with an angle β close to 90°. (b) The structural model based on STM images, the N-Fe coordination bonds estimate to be 2 Å and the Fe-N-C bond-angle close to 180°.

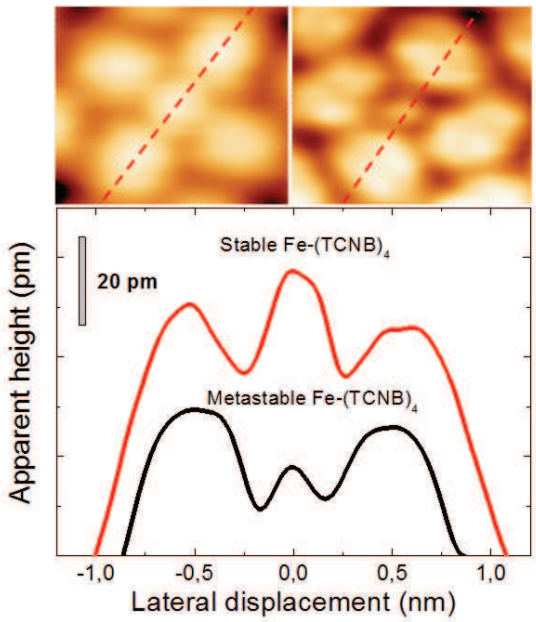

Figure 4.3: Line profiles taken along opposite TCNB ligands at 0.74 V and 150 pA for both, the metastable intermediate and the true molecular complex. For clarity, the profiles are shifted by 10 pm with respect to each other.

magnetic anisotropy [35] while the M-$(TCNQ)_4$ complexes (where M: Ni, Mn and Cs) show a variety of behaviors that crucially depend on charge transfer [63]. Thus, a deeper insight into the electronic properties of $Fe(TCNB)_4$ can only be obtained by thorough STS measurements.

Figure 4.4 shows full dI/dV spectra, between -2.0 eV and +2.0 eV, for both, the Fe-$(TCNB)_4$ complex (Figure 4.4(a)) and the metastable phase (Figure 4.4 (b)). The spectra are recorded by positioning the STM tip on the central Fe-atom (red curve) and on the peripheral ligand (black curve). Aside from the bound state of Fe. Figure 4.4 (b) shows a shoulder at -1.0 V above the iron atom (at -1.5 V above the TCNB). For positive bias, a strong upturn is found above +1.5 V for both, the Fe atom and the TCNB, very much like on the TCNB monolayer on bare Au(111) (see chapter 3). These characteristics show again that the TCNB remains unperturbed in the confined Fe-$(TCNB)_4$ phase. The dI/dV above the $Fe(TCNB)_4$ complex shows new features. There is a clear shifts of the LUMO and HOMO (Highest Occupied Molecular Orbital) orbitals between the precursor of Fe-$(TCNB)_4$ compared to the final stage $Fe(TCNB)_4$ complex. The LUMO is shifted downward by 0.8 V (No. 4 at +1 V), while the HOMO is shifted upwards by 0.5 V. As can be observed, the HOMO-LUMO gap is considerably reduced from 3.0 eV in the precursor system to 2.0 eV in the Fe-$(TCNB)_4$. Similar systematic tendencies of gap reduction have been

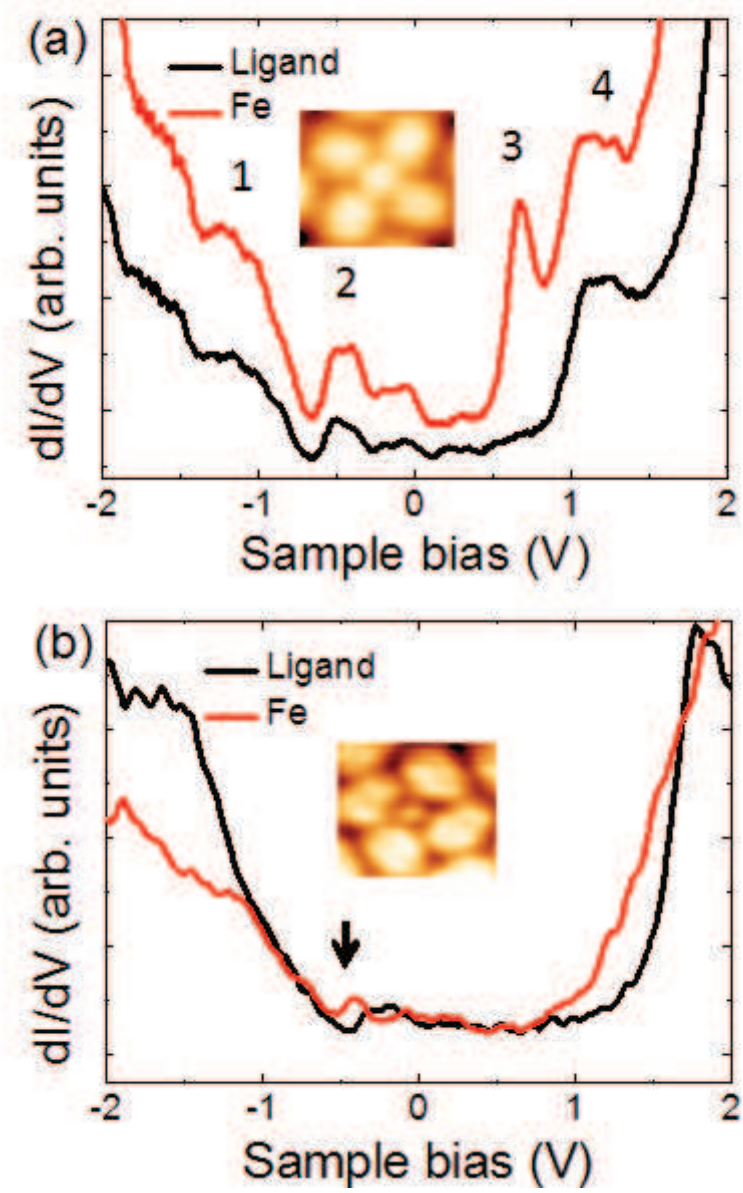

Figure 4.4: STS of (a) $Fe(TCNB)_4$ complex with 180 Fe-N-C bond angle and (b) for comparison the Fe-$(TCNB)_4$-unit in the metastable confined phase. The dI/dV show the closing of the gap when the true $Fe(TCNB)_4$ complex is formed (peak 1 and 4 correspond to HOMO and LUMO respectively) as well as the apparition of additional new features (resonances No 2 and 3) as the fingerprint of bond formation

	Before		After	
	Mayer bond	Distance	Mayer bond	Distance
C-N	2.72	1.16	2.42	1.17
Fe-N	-	-	0.32 - 0.38	1.86
N-H	-	-	0.014 - 0.054	2.2 - 2.5

Table 4.1: Equilibrium geometrical parameters, before (only TCNB molecule) and after the formation of the $Fe(TCNB)_4$ complex.

observed upon lateral coordination of a molecule with metal atoms on a surface [123].

Additionally, the most striking signature of the complex formation is the appearance of a series of new resonances, at -0.5 V and above, corresponding to feature No. 2 in Figure 4.4, very different from the bound state of the confined phase, and a sharp peak, No. 3 in Figure 4.4, localized at +0.7 V. Both of these features refer to molecular orbitals with out-of-plane d-contributions, which are preferentially measured by STM. The fact that the peak at +0.7 V only appears above the Fe atom, and not above the ligand, strongly speaks in favor of a $d_z{}^2$ contribution localized on the Fe atom since this orbital does not form lateral bonds in the x-y plane. Due to the near square planar geometry (with C_4v symmetry), it is anticipated that A_{1g} ($d_z{}^2$) and E_g (d_{xz}, d_{yz}) terms must be nearly degenerate. From the calculation however (see below), the features below the Fermi energy, are identified to be strongly spin polarized d_{xz} and d_{yz} contributions at -0.5 V and -1.0 V respectively.

The boundary conditions involved in the metastable Fe-$(TCNB)_4$ intermediate makes the DFT calculation difficult to handle in this case. Therefore, only DFT calculation for the stable $Fe(TCNB)_4$ monomer complex were performed here. Although the interaction between the metal-organic complexes and the substrate is an important issue in the self-assembly process, the effect of the substrate is not taken into account explicitly here owing to the very demanding calculation this would necessitate. The initial structure of Fe-$(TCNB)_4$ was generated with the ChemSketch software [81]. The system was placed in an isolated orthorhombic simulation cell of $30\times30\times20$ Å ^{3}. To equilibrate and relax efficiently the $Fe(TCNB)_4$, an initial heating to 100 K was done then the system was cooled down to 5 K.

Table 4.1 shows the equilibrium geometrical parameters of the $Fe(TCNB)_4$ complex. The Fe-N distance is 1.86 Å which corresponds to a typical coordination bond length. Table 4.1 also shows evidence for N-H hydrogen-bond between adjacent TCNB moieties inside the $Fe(TCNB)_4$ complex. This interaction confers stability to the structure in a way similar to that evidenced in bio-molecular systems [30].

	Before		After	
Element	Mulliken	Valence	Mulliken	Valence
Fe	1.958	0	3.063	2.094
N	-0.095	2.897	-0.379	2.938
C	0.158	3.838	0.171	3.79
C^1	0.064	3.904	0.044	3.858

Table 4.2: The Mulliken charge distribution and the valence of the main sites of the TCNB and $Fe(TCNB)_4$ complex. Before and after the formation of the coordination bound. The N is correspond to the nearest neighbor Nitrogen atoms of Fe in the complex. The C and C^1 are the nearest neighbor and next neighbor Carbon atoms of Fe atom in the complex

From Table 4.2 it can be seen that the valence is unchanged upon complex formation except for Fe, where a remarkable change from 0 to 2 occurs. The origin of this change is the newly formed coordination of Fe with the four TCNB ligands. From the valence change, we see that the Fe donates 2 electrons and formally becomes Fe^{2+}. The charge transfer occurring between the Fe and the four neighboring N atoms is found to be close to 1 $|e|$. Table 4.2 shows the Mulliken charge and valence analysis of the system before and after the formation of the $Fe(TCNB)_4$ complex. The charge becomes rather delocalized and redistributed among all the TCNB ligands. This is confirmed by a comparative analysis of the difference in the Mulliken charges of the N atoms next nearest neighbors of the Fe ion; about -0.28 $|e|$ per N atom.

The spin density distribution is helpful and informative in the description of the spin coupling mechanism between magnetic center and ligand. In particular, the positive spin at the paramagnetic center (in this case the Fe atom) may induce some spin density at the ligand [22]. The local spin distribution of the $Fe(TCNB)_4$ complex is shown in Figure 4.5. The spin density is well localized on specific regions of the $Fe(TCNB)_4$, in particular, the spin-up amplitude is localized on the Fe ion, whereas the spin-down amplitude is spread on the four TCNB ligands. This spin polarization mechanism is the result of the exchange term introduced by the Pauli principle, that favors the probability of finding two electrons of identical spin in the same region of space. Therefore, the spin of a bonding electron pair is polarized, in such a way that the positive spin is concentrated close to the atom that has an unpaired electron, whereas a concentration of negative spin density is favored around the atoms bonded to it. This effect propagates through the molecule away from the paramagnetic center, thus generating spin densities of alternating sign at rather long distances. The spin distribution on top of the Fe center has $d_z{}^2$ character as confirmed by projecting the Kohn-Sham orbitals onto atomic wave-functions. More specifically, we see that the HOMO levels are the ones contributing mainly to this $d_z{}^2$ orbital; as a consequence,

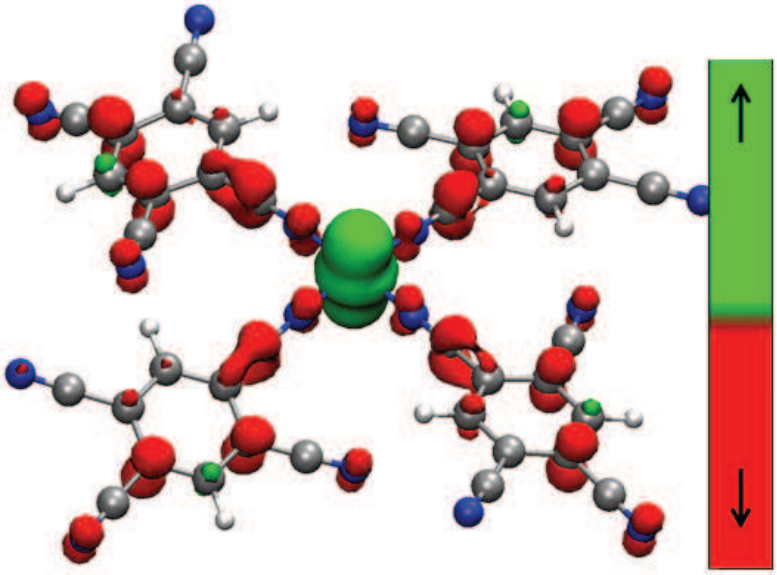

Figure 4.5: Spin density of the Fe(TCNB)$_4$. The green color indicates the spins up, while the red color indicates spin down contributions with isovalue 0.005 e/Å ^{3} .

they do not participate to the planar bonds Fe-N-R and account for the spin sign of the metal.

Figure 4.6 (a, b) shows the projected density of states (PDOS) on the Fe d_{xy}, d_{xz}, d_{yz}, $d_z{}^2$, $d_{x^2-y^2}$ orbitals as well as on the nearest-neighbors N atoms. The PDOS on Fe shows a strong spin polarized contribution from the $d_z{}^2$ state at -2.7 eV. Two spin-polarized peaks of the d_{yz} and d_{xz} type are also found at -0.9 eV and -0.7 eV respectively. Nitrogen does not participate in the spin polarization as shown by identical PDOS for spin-up and spin-down contributions. Finally, the PDOS shows two peaks at 1.3 eV and 3 eV. They are mainly contributions of the Fe $d_z{}^2$ and ligand p orbital of N and are also found in STS measurement where they appear in the form of two remarkable peaks (No.3 and No.4 in the figure 4.4 (a)) above the Fermi level.

The residual interaction with the surface may alter this picture. Our experiment however shows that the Fe-Au hybridization is drastically weakened by square planar coordination to the cyano-groups. As discussed before, the fourfold coordination with the ligands, leads to a lifting of the Fe atom from the gold substrate, thus to a partial decoupling of the Fe atom from it, and as shown experimentally (see chapter 1), to a localization of Fe d-orbitals with E_g symmetry in the HOMO-LUMO gap of the ligands. We therefore may consider that the Fe d-orbitals are only weakly perturbed by the gold substrate, thus conserving most probably the Fe^{2+} character with the d^6 configuration. The splitting of the d-orbital in the ligand field can be analyzed in terms of crystal field stabilization energy (CFSE). This stability results from the fact

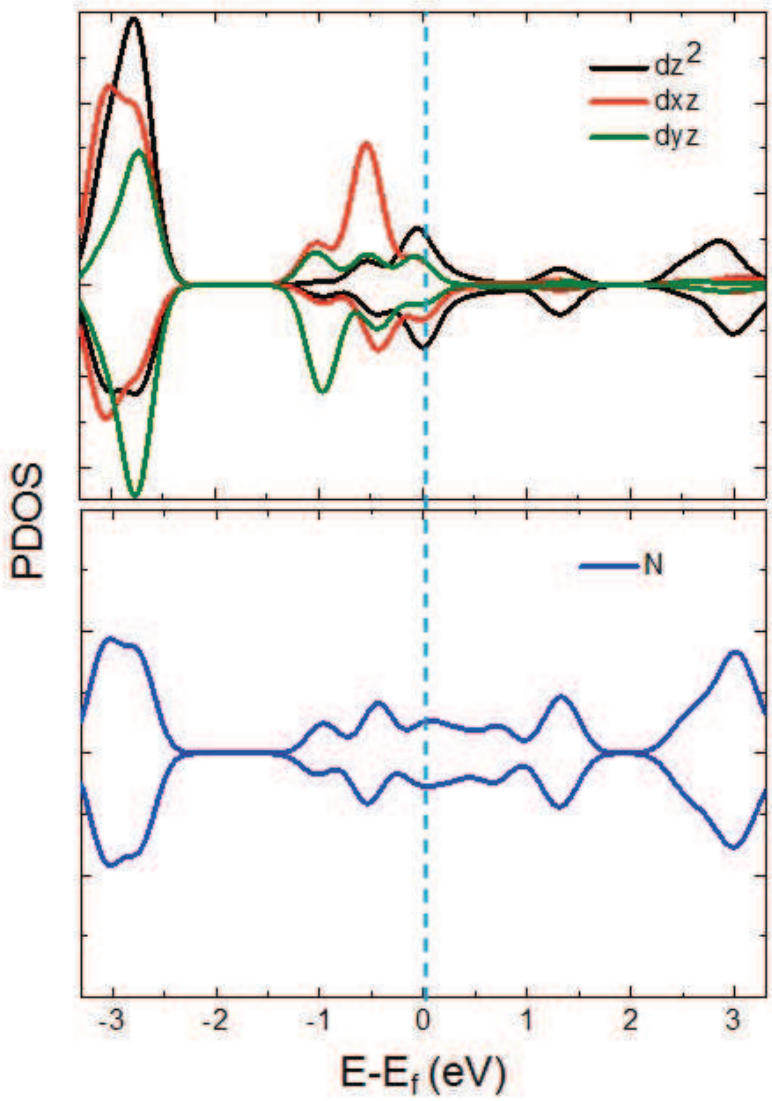

Figure 4.6: Spin-resolved PDOS (a) projected onto the d-orbitals of Fe. (b) on the neighboring N atom. Where the E_F (Fe-$(TCNB)_4$)= -4.77 eV and E_F (N)= -5.03 eV.

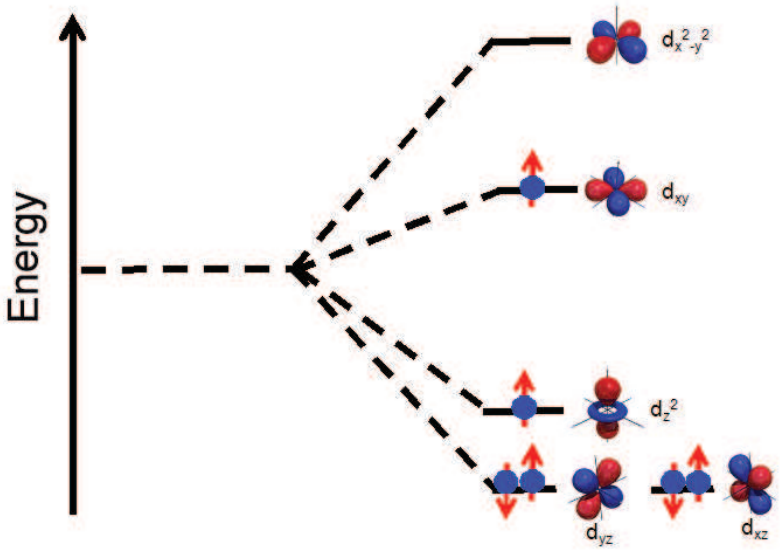

Figure 4.7: Qualitative molecular orbital diagram and d-electron population of the Fe in the square planar complex.

that when the d-orbitals are split in a ligand field, some of them become lower in energy than before (see chapter 1). This is what happens in the near square planar complex (C_{4v} symmetry) under investigation here.i.e the orbital lays at a lower energy than in the more symmetric octahedral complex with degenerate d-levels. Figure 4.7 shows the qualitative analysis of the populations of d-orbitals of Fe as predicted from the ligand-field theory for the square planar complex. The above discussion is in accordance with the PDOS calculation (Figure 4.6 (a)) which shows that the $d_{x^2-y^2}$ contribution has a negligible intensity compared to the d_{xy} , d_{xz}, d_{yz}, $d_z{}^2$ orbitals which are occupied. Moreover, these unoccupied orbitals appears above the Fermi level. We therefore, assumed that the $d_{x^2-y^2}$ orbital of Fe is empty. Considering most probably the Fe^{2+} character with the d^6 configuration, the crystal field energy diagram provides a spin state of S=1 for the Fe, carried by the hybrid in-plane/out-of-plane orbitals d_{xy}, $d_z{}^2$ orbitals, respectively.

4.4 Conclusions

In conclusion, by seeding the TCNB mother phase with Fe atoms, we were in a position to study the self-assembly of Fe-TCNB, through the reaction path from individual objects to the $Fe(TCNB)_4$ complex by STM, STS and with the help of first principle dynamical calculation. Insight was obtained on how the electronic structure of both, atom and ligands are modified by the formation of coordination bonds. Two

ordered $Fe(TCNB)_4$ phases with widely different properties are identified. First, an ordered metastable phase is formed whose HOMO-LUMO gap remains featureless except for a bound state formation on Fe (similar to Fe on a bare metal surface) and a quasi unperturbed dI/dV of the TCNB ligand indicating that no bond has formed between Fe and TCNB. In a subsequent step, when the system is allowed to relax to its equilibrium geometry, a new $Fe(TCNB)_4$ monomer phase is formed that shows a clear signature for metal-organic coordination in the dI/dV data. Our findings, which are related to the atomic scale modification of the electronic structure at metal organic interface, are important to understand the different properties observed between the metastable forms and the final metal-organic complexes.

Chapter 5

The formation of 2D $Fe(TCNB)_2$ coordination network and comparison with Iron-Phthalocyanine molecule

5.1 Two-dimensional Fe-TCNB coordination network on Au(111)

The deposition of TCNB molecules and iron atoms in a proportion of 2:1 and post-annealing up to 450 K leads to a fully reticulated $Fe(TCNB)_2$ network as shown in Figure 5.1(a). The network is formed by Fe atoms interconnected with TCNB molecules different from the $Fe(TCNB)_4$ monomers assembly. The apparent height of the single sheet network is approximately 2 Å above the gold surface as shown in Figure 5.1(b). Domains with a lateral extension of 10-30 nm are formed and separated by domain boundaries. The control on the stoichiometry of the network is crucial for a successful reaction. An excess of metal atoms or molecules can prevent the formation of well-ordered networks and lead to the formation of disordered phases. As an example of point defects, see the Fe vacancies visible from the STM topography marked by red circles in the Figure 5.1(a,c).

A careful analysis of the STM data shows that the network has a square structure with a measured periodicity of $\vec{b_1} \approx \vec{b_2} = 1.15 \pm 0.1$ nm in both directions as shown in Figure 5.1. The azimuthal angle θ between the substrate and adlayer is close to 12°. According to the epitaxial relation, we obtain a commensurate superstructure with the following matrix: $\begin{bmatrix} 3 & 1 \\ -3 & 4 \end{bmatrix}$. The N-Fe coordination bond is estimated to be 1.8

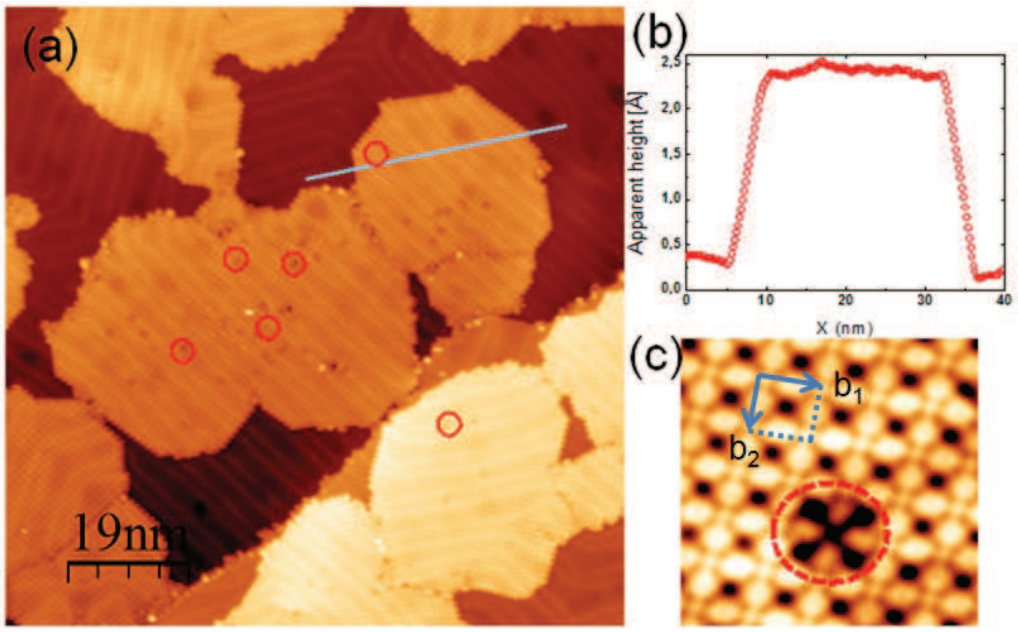

Figure 5.1: (a) STM topography image of the formation of $Fe(TCNB)_2$ network on Au(111)(94 × 94 nm, I=0.2 nA, V=-0.9 V). The missing Fe atoms are marked by the red circles. (b) Line profile of the network, the apparent height is approximately 2 Å above the gold surface (c) High resolution images of $Fe(TCNB)_2$ network with a missing Fe atom.

Å and the Fe-N-C bond-angle is close to 180° similar to the $Fe(TCNB)_4$ assembly.

The networks contain two mirror-symmetric, clockwise and anticlockwise chiral domains as shown in the Figure 5.2. The two domains are separated by grain boundary (blue dashed line in the Figure 5.2 (a)). Furthermore, the mirror-symmetric domains are miss-oriented along the shortest Fe-Fe directions by an angle $\phi \approx 90°$ with respect to the each other (shown by the green arrows). Figure 5.2 (b) shows the corresponding structural model based on the STM images. The coexistence of two mirror-symmetric domains indicates that the two equivalent adsorption configurations of molecules lead to distinct chiral binding motifs upon coordination to Fe atoms. The formation of extended structures suggests that the surface plays a role in guiding the self assembly.

In order to investigate the local electronic structure of the network on Au(111) surface, STS measurements were performed at various positions. Figure 5.3 shows full dI/dV spectra, between -1.5 eV and +1.5 eV, for the $Fe(TCNB)_2$ network. The two dI/dV spectra show six resonances at sample bias -0.97 V, -0.79 V, -0.75 V, -0.37 V, +0.46 V, and 1.5 V, respectively. To gather more information about the STS feature, we have acquired images at biases where resonances occur in the spectra as reported in Figure 5.4. We have chosen six biases: -1.5 V, -0.78 V (close to peak No.2 and

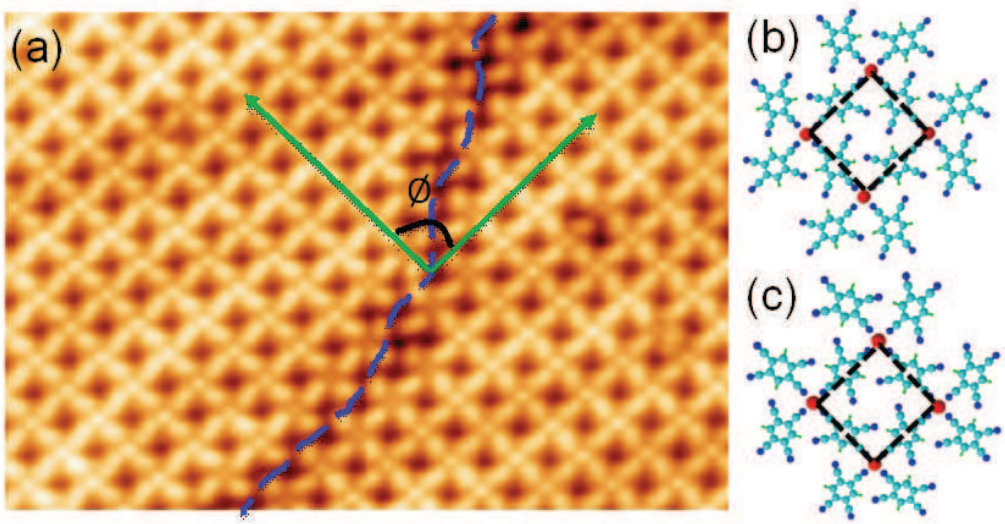

Figure 5.2: (a)Two equivalent chiral domains of $Fe(TCNB)_2$ network are separated by visible grain boundary (blue dashed line on Au(111) (40 × 25 nm, I= 0.23 nA, V= -0.75 V).(b, c) The structural models based on the STM images of the two mirror-symmetric, clockwise and anticlockwise chiral domains.

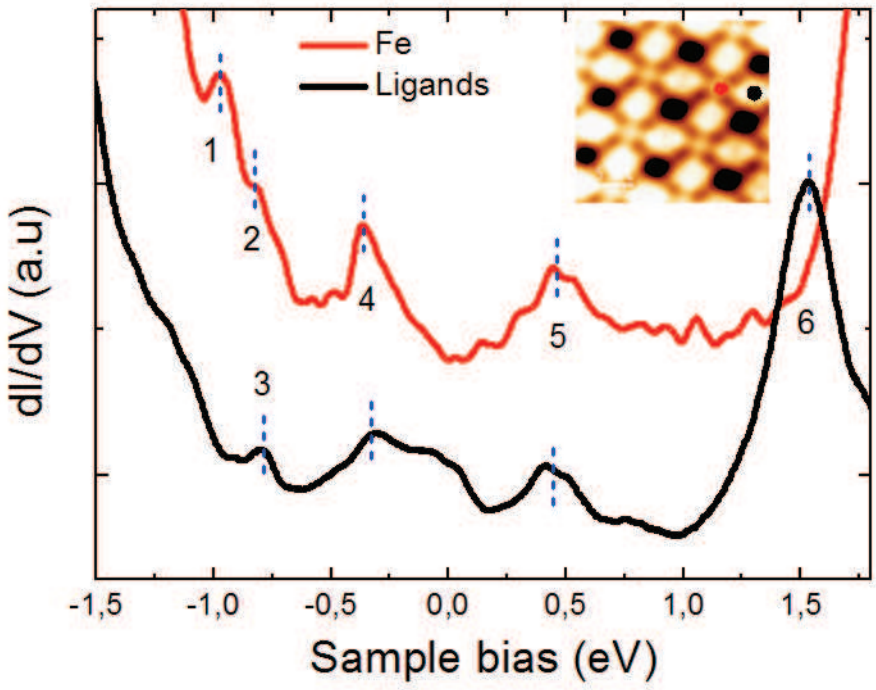

Figure 5.3: STS of $Fe(TCNB)_2$ network for both, on the Fe in the $Fe(TCNB)_2$ network and with same condition on the ligand (Feedback loop opened at V = -0.7 V, I = 0.2 nA).

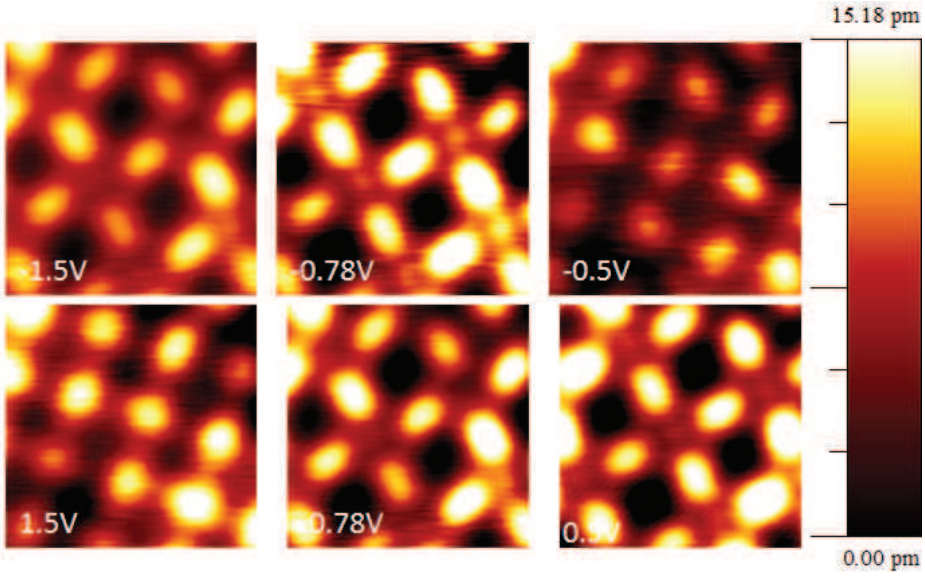

Figure 5.4: STM topographic image of $Fe(TCNB)_2$ network on Au(111) surface (3×3 nm) at different biases, noted above the images.

No.3), -0.5 V (close to peak No.4), +0.5 V (close to peak No.5), and +1.5 (peak No.6). Figure 5.4 shows STM topographic images taken at different biases. It shows distinct changes in the interval between -1.5 V and +1.5 V. At -1.5 V, the TCNB molecules reveal a rectangular shape typical for the TCNB molecules at similar bias on Au(111) (see Figure 3.2 in chapter 3). Note that at this bias, no contrast corresponding to Fe atoms is visible. Contrasts corresponding to the metal centers appear at -0.78 V. As will be demonstrate in this chapter, such contrast can be associated with the Fe d-states of the $Fe(TCNB)_2$ in the network. At -0.50 V, neither the molecule nor the Fe show significant contrast, in agreement with the dip observed in the spectra of Figure 5.3. Finally, the change of the TCNB contrast at +1.5 V, from rectangular to circular, is most probably associated with the visualization of the benzene rings at this bias.

As it is always difficult to identify STS features without external supports, we choose to compare the dI/dV of the $Fe(TCNB)_2$ network with those of the FePc molecule taken as a reference.

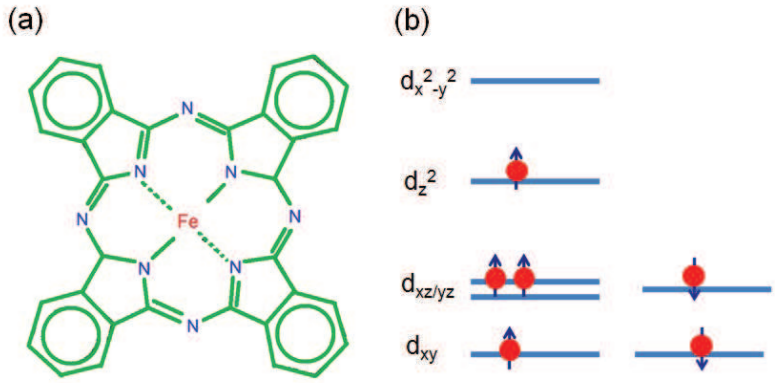

Figure 5.5: (a) The molecular structure of the metal phthalocyanine. The Fe is involved in two covalent and two coordinate bonds with the nitrogen atoms of the pyrrole rings. (b) A schematic representation of the d orbital energy diagram of the FePc molecule [72, 122].

5.2 Study of adsorption of single iron phthalocyanine on Au(111)

The Fe-phthalocyanine (FePc) was chosen as a reference because it shows similarities but also differences compared with the $Fe(TCNB)_2$ network. As shown in Figure 5.5 (a), the molecular structure consists of a central metal ion surrounded by a macrocycle of alternating carbon and nitrogen atoms. The Fe in the FePc is involved in two covalent and two coordination bonds with the nitrogen atoms of the pyrrole rings as shown in the Figure 5.5 (a). The Fe atom of the molecule is in the +2 oxidation state and shows a paramagnetic behavior both, in the gas phase and when adsorbed on Au(111) [72, 122, 100]. It has a d^6 electron configuration and bears two unpaired electrons leading to S=1. Figure 5.5(b) shows the ligand field splitting in the square planar FePc complex resulting in the $d_{x^2-y^2}$ orbital being higher in energy than the d_{xy}, d_{xz}/d_{yz} and $d_z{}^2$ orbitals which are very close in energy. As a consequence the d^6 electrons occupy the lower energy orbitals.

The FePc molecules were evaporated onto Au(111) surfaces by means of a home-made evaporators and the surface coverage was calibrated by STM. Before deposition, the crucible with the FePc was heated overnight just below the evaporation temperatures for purification. The Au(111) surface was kept at room temperature during the deposition. Figure 5.6 (a) shows a typical STM image with a coverage of approximately 0.2 ML of FePc molecules on Au(111). It can be seen that most of FePc molecules are adsorbed on fcc regions of the reconstructed Au(111) surface. Only a few FePc molecules are adsorbed on the elbow of the hcp regions. This preferential adsorption behavior indicates that the adsorption of FePc molecule is more stable on

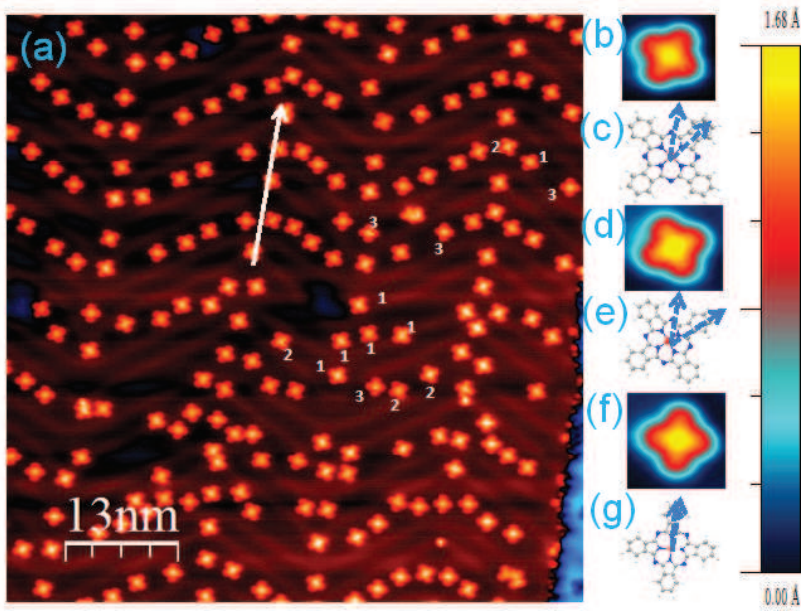

Figure 5.6: (a) STM images (63 × 63 nm) of 0.2 ML FePc molecules on Au(111) surface, I= 0.2 nA, V= -0.34 V. (b-g) There are three different orientations of FePc on Au (111) surface respect to the [11$\bar{2}$] crystallographic direction of gold.

fcc than on the hcp region. The white arrow in image represent the [11$\bar{2}$] directions of the Au(111) substrate. Three different adsorption orientations are identified. For each orientation, enlarged images of representative FePcs are plotted in Figure 5.6 (b, d, f). The FePcs appear with their characteristic four-lobe structure and a bright center. This suggests a planar adsorption structure on Au(111) surface. The molecular axes of configuration 1 are found to be making 28 ° angle with respect to the [11$\bar{2}$] crystallographic direction of gold. The molecular axes of configurations 2 and 3 are rotated by 58° and 5° with respect to the [11$\bar{2}$] direction, respectively. Figure 5.7 shows the relative frequencies of the three molecular distributions. It shows that the

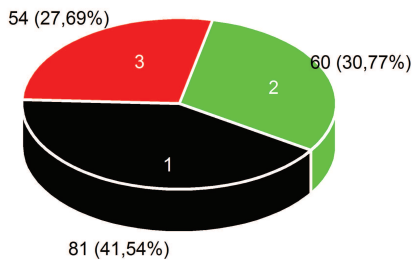

Figure 5.7: The relative frequencies of the FePc with three different adsorption configurations on Au(111).

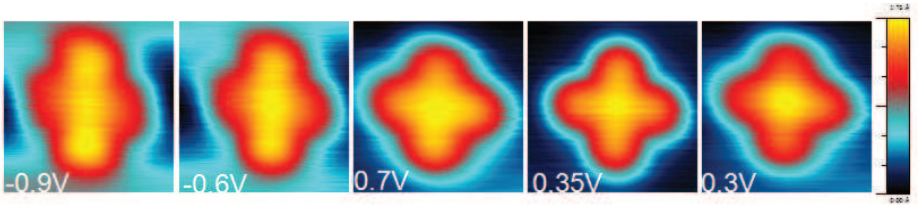

Figure 5.8: STM topographic images of FePc on Au(111) (2.49 × 2.49 nm) at different biases, noted in the images.

configuration 1 (41%) slightly dominates over configuration 2 (27%) and configuration 3 (30%). As reported earlier, the molecules adopt two types of adsorption configurations on the Au(111) surface, i.e., the on-top and bridge configurations [36, 54]. In the on-top (bridge) configuration, the Fe atom is located in the on top (bridge) site with the molecular plane parallel to the surface. While the spectral features of both configurations have been analyzed in great details at the Fermi energy principally in relation with the Kondo behavior [36, 54] no detailed study has been published yet on the full spectroscopic analysis.

It is well known that the appearance of metal phthalocyanine molecules in STM images depends on the molecular states involved in the tunneling process, i.e., on the applied bias voltage as well as on the nature of the transition metal center [73]. The evolution of STM topography above FePc as a function of bias voltages is depicted in the Figure 5.8. The metallic center of the molecule appears as a protrusion in the topography for all bias voltages between -0.9 V to +0.7 V due to the half filled $d_z{}^2$ states of Fe.

In order to investigate the local electronic structure of the individual FePc molecules, STS was performed on different locations above the molecule. The two dI/dV spectra above the Fe atom (red) and on the benzene rings (black) of FePc molecules are presented in Figure 5.9 (a). There are seven main features at sample bias -0.9 V, -0.79 V, -0.72 V, -0.37 V, -0.18 V, +0.5 V, and 0 V, respectively. Since the spectrum recorded on pristine Au(111) surface does not reveal the above features, the peaks were attributed to the molecular structure of FePc adsorbed on the Au(111) surface. The features at positive bias voltages corresponds to the unoccupied states of the FePc molecules on the surfaces. In this energy domain, the spectra are featureless except for a broad signature at +0.5 V (No.7). The fact that the peak at +0.5 V only appears above the ligand, and not above the Fe atoms, strongly speaks in favor of a LUMO contribution of the molecule on Au(111) surface. For negative sample voltages, the dI/dV spectra show well-defined peaks. On the ligand, there is a peak at -0.7 V (No. 2) attributed to the HOMO which agrees well with previous valence-band

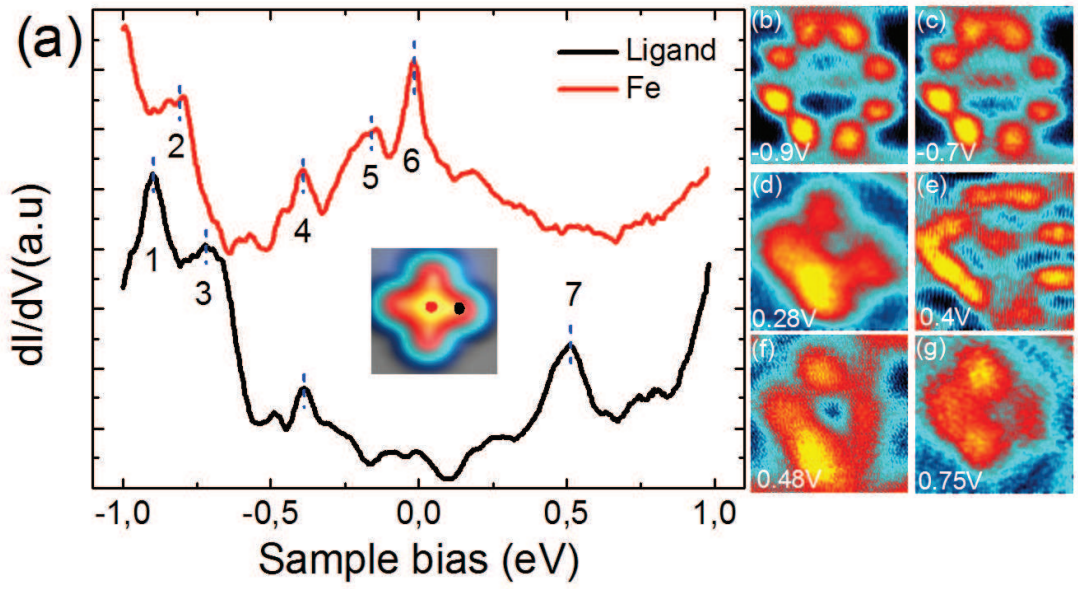

Figure 5.9: STS spectra above Fe in FePc molecules and with same condition on the lobe of FePc (b) The constant current dI/dV (I=0.2 nA, V=0.5 V) maps are recorded at the same voltage as the spectral features on the FePc

photo-emission spectra studies on FePc/Au(111) [99]. A sharp peak denoted as No 1 and located at -0.9 V is then the lower lying occupied molecular orbital (HOMO-1). On the Fe, there is a shoulder at -0.79 V (No. 2), the origin of this feature is mainly due to the $d_{xz/yz}$ orbital of Fe [36]. There is one relatively intense resonance on both spectra at -0.37 V, noted No. 4 resembling the one observed by Gao et al [36]. They have assigned this resonance to adsorption-induced states. More precisely it is thought that this resonance arises from the hybridization between the HOMO of the FePc molecule and the Au(111) electronic surface states.

The spatial distribution of the molecular orbitals at -0.9 V, -0.72 V, -0.37 V, -0.18 V, +0.5 V, can be visualized from the constant current dI/dV maps (Figure 5.9 (b-g)) recorded at close to above voltages. The dI/dV maps acquired at -0.9 V and -0.7 V show a dominant contribution from the four lobes of the molecule as expected for the HOMO and HOMO-1 sates observed at this voltage in the dI/dV spectra. dI/dV maps at positive bias exhibit additional spectral weight due to the LUMO orbitals of the molecules.

To get some additional information on the differential conductance we also recorded constant-height dI/dV maps [46]. Figure 5.10 shows constant-height dI/dV maps at different bias voltages. These maps were recorded by exploring the x-y space at a

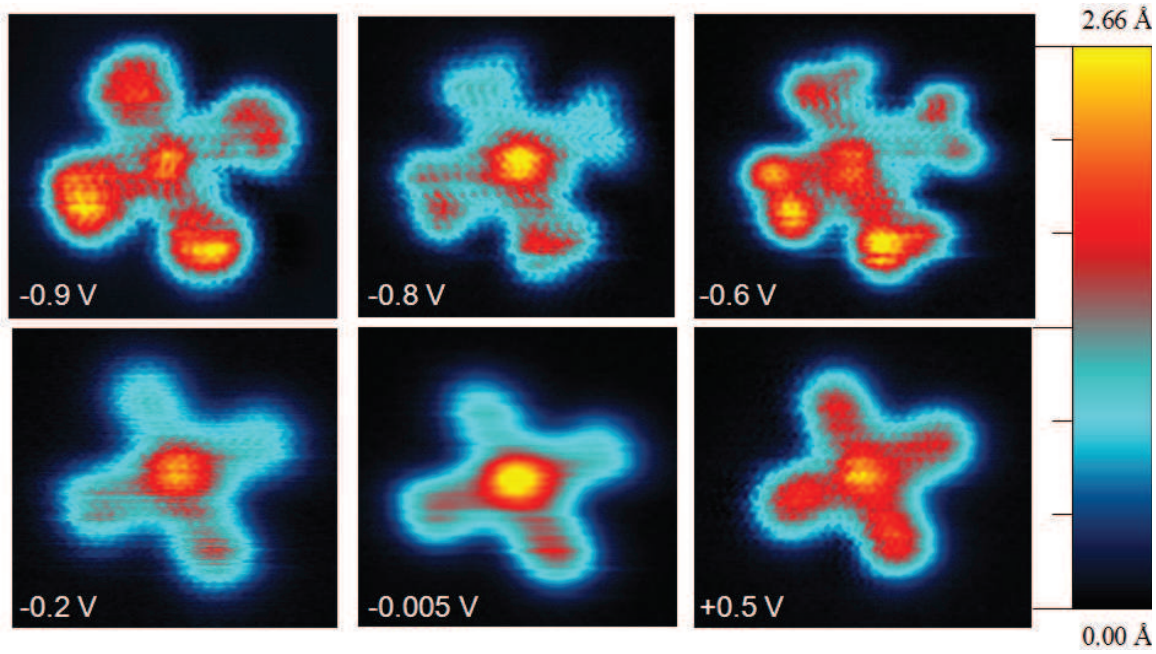

Figure 5.10: The constant height dI/dV maps over the FePc (2×2 nm^2). The feedback loop was opened over the Au(111) surface at 0.01 nA and the bias indicated in each map.

constant tip-height above a single FePc molecule. In this case, a better signal to noise ratio is observed compared to the constant current dI/dV maps, chiefly because in this mode, the feedback loop remains open during the data acquisition.

As can be seen from Figure 5.10 , dominant conduction channels are found over the Fe atom at negative bias, confirming previously reported peaks above the Fe center in the FePc. Interestingly, three strong conductance channels are found over Fe atom at -0.80 V, -0.20 V, and 5 mV, respectively. These energies correspond to d-orbital contributions and a Kondo resonance of Fe in the FePc molecules (see below). Furthermore, in Figure 5.10, there are three dominant conduction channels stemming from the mixed contribution of ligands and metallic centers of FePc at -0.9 V, -0.6 V, and +0.5 V. These energies are the contributions of HOMO-1, HOMO, and LUMO orbitals of the FePc molecules. One should mention that different rotational symmetries produced by a structural distortion of the molecules were observed in constant-height dI/dV maps carried out on CoPc on Cu(111) [46]. Our measurements however do not show clear evidence for different rotational symmetries on FePc on Au(111).

The peak at 0 V, noted No 6 in Figure 5.9, is a well known Kondo signature observed previously in FePc on a Au (111) [36] . The width of the Kondo peak depends on the adsorption site of FePc on the Au(111) surface [54]. Figure 5.11 (a, b)

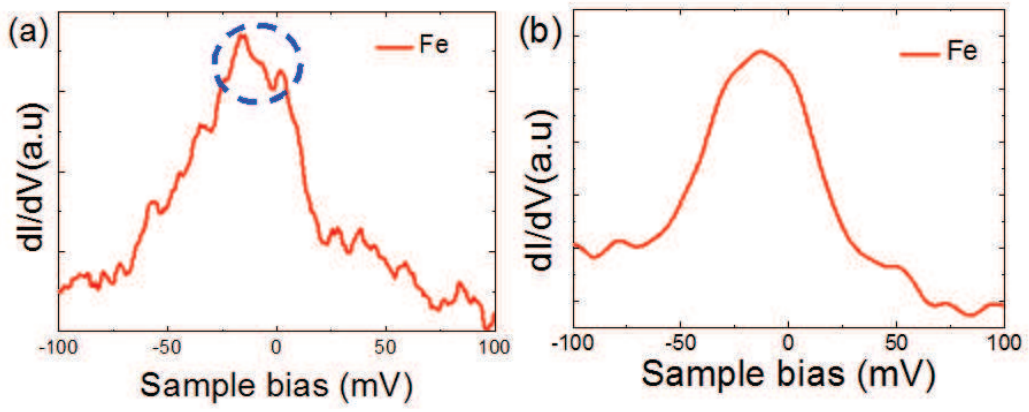

Figure 5.11: The Kondo signature of two different adsorption of FePc on Au(111) surface. (a) the spectrum on top position where the Kondo peak appears as a deep inside the large peak (blue circle) (b) the spectrum on bridge position where the Kondo peak appears as a peak.

shows the characteristic spectral features of FePc on the two different adsorption sites close to the Fermi level. For the on top species, a broad peak appears accompanied by a sharp dip structure "inside" the peak highlighted by blue circle in the Figure 5.11 (a). In contrast, only a broad peak is observed for the bridge species (Figure 5.11 (b)). Minamitani, et al. [54] observed similar features close to E_F and they have identified them as Kondo peaks with different T_K. More precisely it is thought that the two different Kondo peaks appear because of the symmetry of the ligand field through the local coordination to the substrate [54]. For FePc in the on top configuration with fourfold symmetry around the Fe^{2+} ion, the orbital degrees of freedom survives, resulting in the spin and orbital SU(4) Kondo effect. In contrast, the reduced symmetry of the bridge configuration freezes the orbital degrees of freedom, leading to the spin SU(2) Kondo effect.

Finally, just beside the Kondo peak, there is a broad peak located at - 0.18 V (No 5 in Figure 5.9). This features was not reported in previous studies of FePc on Au(111). However, a similar feature has been observed for FePc on Ag(111) [40] and Ag(100) surfaces [83]. The origin of this feature is related to the out of plan d-states $d_z{}^2$ of the Fe atom. In order to clarify this point, we carried out STS measurements above the FePc on different surfaces.

Figure 5.12 (a-d) shows the STM topographic images and the dI/dV spectra of FePc absorbed on the Au(111), Cu(111), and the cobalt nano island. The corresponding dI/dV spectra acquired on the center of the FePc molecule exhibit a shift of the Fe d-state towards to the E_F. The positions of Fe d states are summarized in the Table 5.1 for different surfaces.

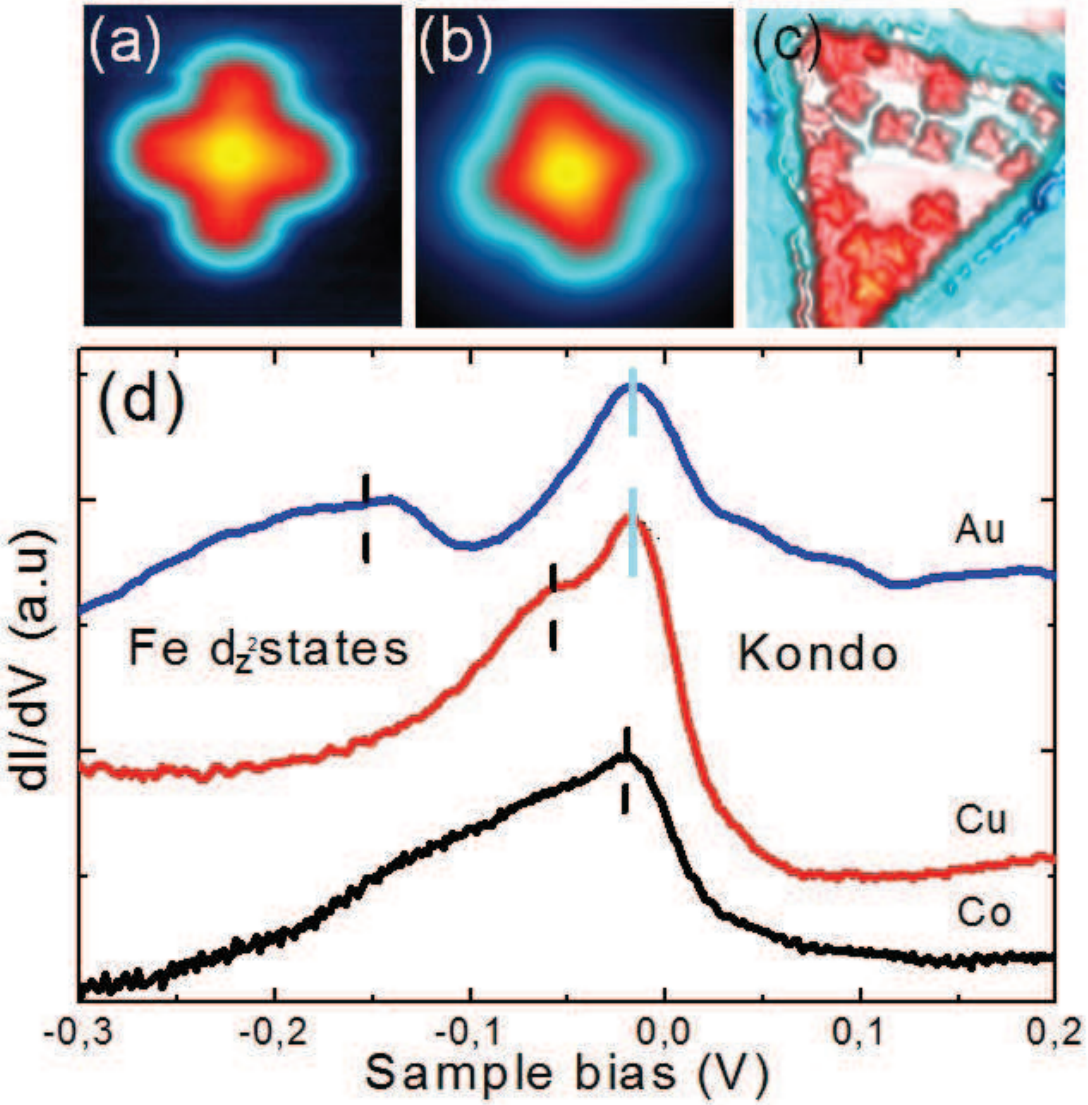

Figure 5.12: STM topographic images of FePc on (a) Au(111) (4×4 nm^2), (b) (4×4 nm^2) Cu(111) and (c) Co nanoisland (24×24 nm^2) (c), respectively. (d) The position of $d_z{}^2$ orbital of Fe changes with different substrate. Feedback opened at 0.4 nA, -0. 3 V (the spectra are vertically shifted for clarity).

	Au(111)	Ag(111)	Ag(100)	Cu(111)	Co island
Peak position (mV)	-150	-250 [40]	-250 [83]	-50	-10

Table 5.1: The position of d_{z^2} orbital of Fe in the FePc molecules of different metal surfaces.

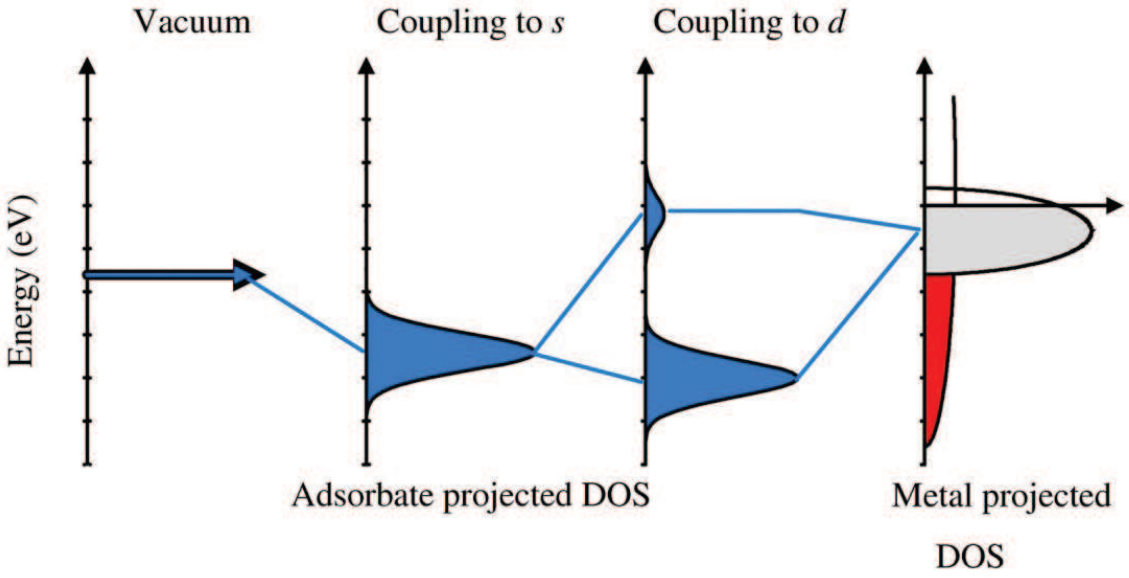

Figure 5.13: The formation of a chemical bond in the interaction between an adsorbate state and the s and d band of a transition metal (from [85]).

To understand the shifting of d-states of Fe on different surfaces, it is useful to introduce the so-called d-band model [86, 44], that accounts for the interaction of adsorbate electrons with the valence states of surface atoms. In the metal, the highly itinerant s and p-band electrons form a broad band of states whereas the d-band electrons form a relatively narrow band owing to the small coupling matrix element between the more localized d orbitals. The coupling mechanism between the adsorbate and the surface can be viewed as a two-step process as described in Figure 5.13. First of all, the adsorbate couples to the broad metal sp-band, leading to a shift and a broadening of the adsorbate states. Second, the re-normalized adsorbate states then couple to the metal d-states. Since d bands are narrow, the interaction of an adsorbate state with the d electrons of a surface often gives rise to bonding and anti-bonding states just as in a simple two-state problem. If the first step coupling to the metal sp-band can be considered to be essentially similar for the transition and noble metals, then, the interaction energy between an adsorbate and a metal surface are governed by the second step which is the coupling to the metal d-band. The key parameter in the d-band model is the position of the d-band center with respect to the Fermi energy, E_d-E_F. The noble metals exhibit a low-lying d-band center,

Element	d-band center (eV)	d-band filling
Fe	-0.92	0.7
Co	-1.17	0.8
Cu	-2.67	1
Au	-3.56	1
Ag	-4.30	1

Table 5.2: The center of the d band is calculated for the most close-packed surface for each of the metals [(111) for fcc, (001) for hcp, and (110) for bcc] [53].

because the d-band is filled with electrons. The d-band center and d-band filling for different metal surfaces are summarized in the Table 5.2. The Table 5.2 shows that the (energy) position of the d-band center obeys the same order Ag<Au<Cu<Co as the d-band shift observed experimentally.

In the case of Ag, where the d-band center is lowest in energy the interaction with virtually any adsorbate gives rise to a large fraction of anti-bonding states, which results in a weaker binding energy of the adsorbate to the surface. On the contrary, the Co surface which has a d-band center close to the Fermi level, a large fraction of the anti-bonding states between the adsorbate and the surface will be pushed above the Fermi level, resulting in a strong bonding character with the surface. Therefore a possible route for modifying the reactivity of the metal surface is to alter the energy of the d-band center relative to the Fermi level. For example, a d-band center close to E_F (cobalt) provides a more reactive surface to adsorbates than a d-band center well below E_F (noble metals). This might then explain the strong shift of d states of Fe in FePc on the cobalt nanoislands. Figure 5.14 shows the relation between the center of d-band and the shift of the d states of Fe in FePc on different surfaces. Interestingly, the d-state shift shows the same trend as the d band shift as we move from Ag to Co surfaces.

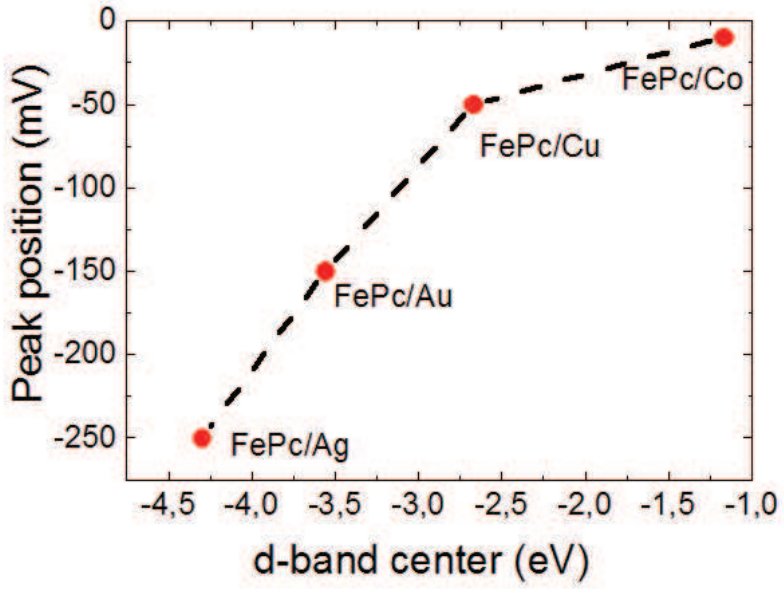

Figure 5.14: The position of $d_z{}^2$ orbital of Fe is shifting towards the Fermi level as a function of d band center (the dashed line is a guide for the eyes).

5.3 Spectroscopic identification of the $Fe(TCNB)_2$ coordination network on Au(111)

As discussed above, the Fe in the FePc is involved in two covalent and two coordination bonds with the nitrogen atoms of the pyrrole rings. Therefore, we expected electronically similar environments for the central metal ions (Fe) in the network and in the FePc. In this section we will use the information gathered from the spectroscopic labeling of FePc to identify some of the resonances of the $Fe(TCNB)_2$ network. The unit cell of the $Fe(TCNB)_2$ network contains eight nitrogen atoms where four nitrogen atoms make a coordination bond with Fe atom shown in the Figure 5.15

For the sake of comparison, Figure 5.16 shows the dI/dV spectra on both, the coordination network and the FePc molecules. We found that there are three similar features on both spectra, two of them on the Fe atom and one on the ligand. In particular, the feature at -0.79 V on the Fe, attributed to the $d_{xz/yz}$ orbitals, is similar in both systems, indicating that the Fe somehow feels a similar environment from the TCNB ligands in the network and in the FePc molecules. Furthermore, STM topographic images also show that at this particular bias, the metallic centers appear as bright spots. It is worth noting that the feature at -0.79 V also resembles the one observed on iron clusters on the Au(111) surface surrounded by the

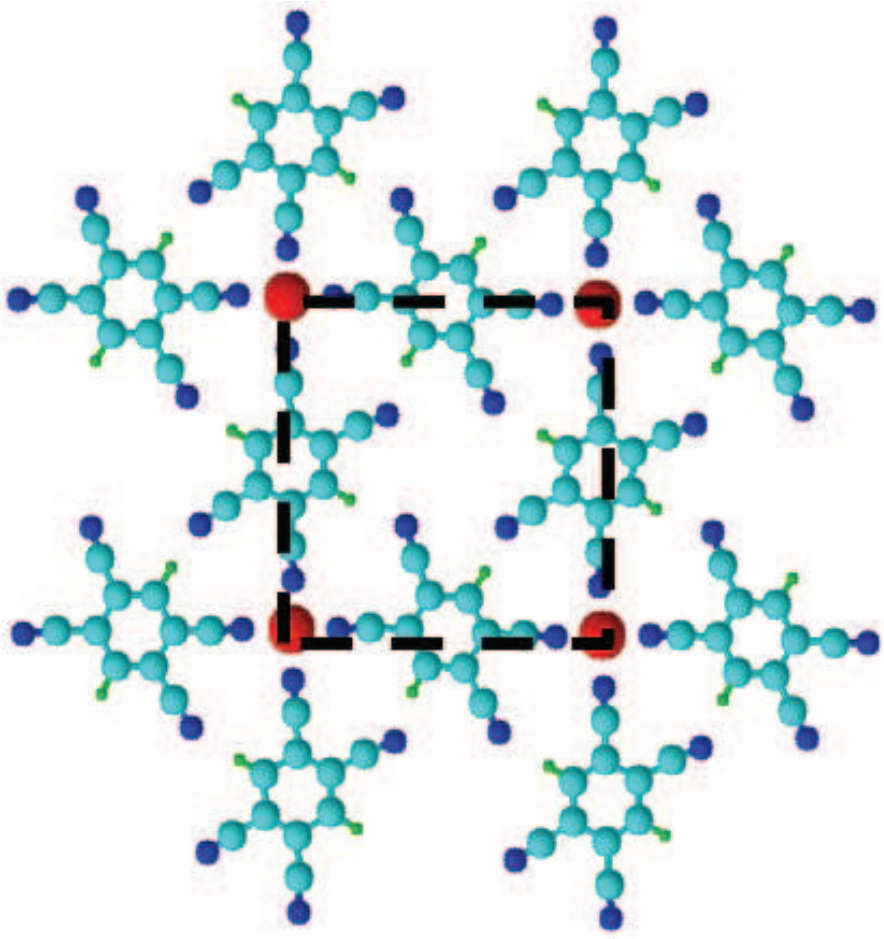

Figure 5.15: The unit cell of the $Fe(TCNB)_2$ network (black dashed line). The unit cell contains 8 nitrogen, 16 carbon, 1 Iron, 4 hydrogen atoms.

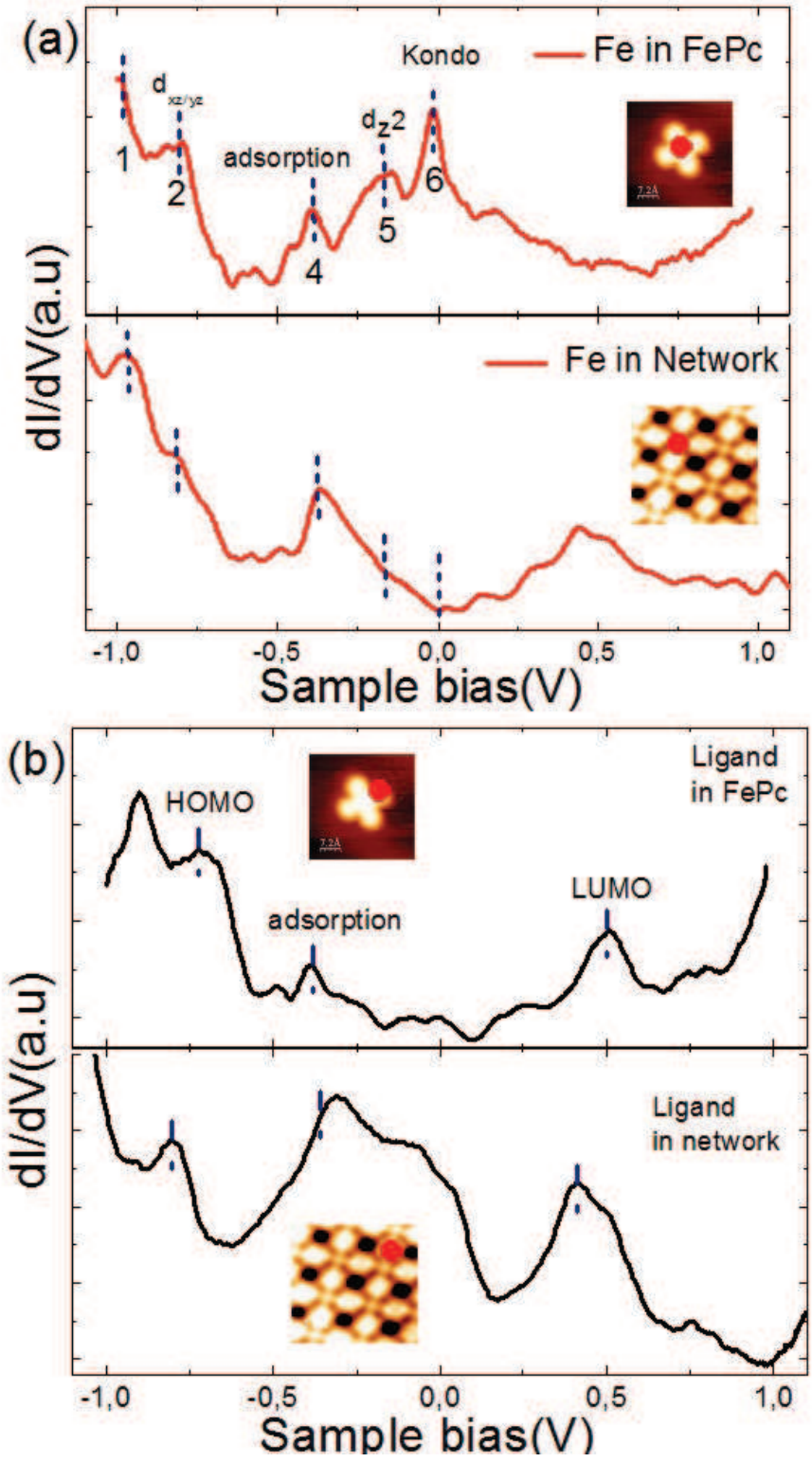

Figure 5.16: The comparison of two dI/dV spectra were taken on the network and on the FePc molecule on Au(111) surface. (a) dI/dV spectra on the Fe in the network and Fe in the FePc, respectively (b) dI/dV spectra on the ligands of $Fe(TCNB)_2$ and the lobs of FePc molecules, respectively.

	FePc	Network
LUMO	0.5 V	0.46 V
HOMO	-0.7 V	-0.75 V
Kondo	0 V	-
dxz/dyz	- 0.79 V	-0.79 V
Surface induced states	-0.37 V	-0.37 V

Table 5.3: A summary of all similar peak positions of the network and FePc on Au(111) surface.

3,4,9,10-perylene-tetracarboxylic-dianhydride (PTCDA) molecules [79]. The second remarkable feature, namely the surface induced state found at -0.37 V on the Fe atom above the FePc is also present in the network.

Finally, the ligand spectra of Figure 5.16 show that the LUMO orbital of the network is located at 0.46 V, close to the LUMO orbital of FePc (0.50 V). On the other hand, the HOMO orbital is located close to -0.75 V again, close to the one of FePc (-0.7 V). This leads to a HOMO-LUMO gap of the network close to 1.2 V. It turns out that this gap is smaller than the gap of 2 V observed for the $Fe(TCNB)_4$ complex. Features that are similar in both, network and FePc are summarized in the Table 5.3. While the covalent bond of FePc leads to a spin state of S=1 and a Kondo temperature in the range of 200 K, we do not expect similar Kondo temperatures for the network. Several reasons may explain the absence of the Kondo peak in the network as for example a different spin state, different coupling with the substrate, a Kondo temperature that is so low that it lies below instrumental resolution.

In the following, we discuss in more detail the origin of the features observed by STS in terms of bond formation. As usual, we focus on the d orbitals close to the Fermi level (E_F), namely the d_{xz}, d_{yz} orbitals that can interact with the p orbitals of the N atoms and the localized d_{z^2}. Those orbitals mainly determine the shape and positions of the experimental peaks most sensitive to the STS measurement. The bonding of metal-ligand complexes can be described in the framework of molecular orbital theory (MOT). The driving force is the overlap of valence metal and ligand orbitals, respectively, leading to the formation of bonding and anti-bonding orbitals. These are the 3d, 4s, and 4p valence orbitals of Fe and σ-like and π-like orbitals of TCNB. The orbital overlap can imply a charge transfer from Fe to the TCNB molecules or vice verse. For example, the overlap of an empty metal Fe s-states with an occupied TCNB σ orbital can lead to a charge transfer to the Fe metal atom. On the other hand, the overlap a Fe occupied d state with an unoccupied TCNB orbital, for example a π^* orbital, can also cause a charge transfer back to the TCNB molecule. The charge transfer from the TCNB back to the Fe metal atom is known as π back

donation [33, 65]. Both can happen simultaneously and in synergy. The transition of a pure ionic to a pure covalent character of the metal-ligand bond is therefore continuous and depends on all charge transfer processes. In general the 3d, 4s, and 4p orbitals of the transition metal atom form hybrid orbitals leading to polyhedral coordination geometries [33].

In the case of the Fe-$(TCNB)_2$ network, the N atoms in the TCNB exhibit lone-pair electrons. The overlap of occupied valence Fe states and empty s orbitals of N presumably triggers the formation of a metal-ligand bond, which can involve a charge transfer from the Fe to the N atoms. The bonding to the N atoms in the TCNB is mainly driven by the s and p orbitals. In the case where d-electrons are also involved in the metal-ligand bond formation, bonding motifs with higher symmetry can be observed [33]. In the presence of an electron donor (Fe atom in this case), we expect TCNB to become negatively charged and to fill the LUMO with electrons from the Fe atoms. The main σ interaction between the Fe and N atoms is involving a $d_{x^2-y^2}$ orbital of Fe and s, p orbitals of the N. In the STS measurement, we only observe the π orbitals, that is the $d_{xz/yz}$ interaction with the p_z orbitals of the N atoms. The d_{z^2} of Fe however, is non-interacting due to the symmetry reason [105].

In FePc, the Fe atom has square-planar coordination with four pyrrolic N atoms. There are four strong σ-orbitals bonding and 21 π-orbitals bonding and non-bonding arising mainly from the phthalocyanine [113]. The metal atoms supply one electron each to the nitrogen atoms of the isoindole groups and these isoindole nitrogen atoms in turn supply an electron to the metal atom, forming a covalent bond. On the contrary, the unshared pairs of electrons in the remaining two isoindole nitrogen atoms presumably form coordination bonds with the metal atoms [97]. The presence of the coordination bonds in both FePc and Fe in the network may explain similar spectral features.

According to the above description, it turns out that contrary to FePc the d_{z^2} orbital of the Fe atom is not involved in the coordination bond of the $Fe(TCNB)_2$ network, where there is a mixing of π and σ bonds due to the benzene rings [3, 76, 94]. This may explain why peak No.5 (d_{z^2}) is observed on FePc but not on the network.

5.4 Conclusions

In conclusion, the growth of the $Fe(TCNB)_2$ network on the Au(111) surface has been investigated. The deposition of TCNB molecules and Fe atoms in a 2:1 stoichiometry and post-annealing up to 450 K enables to form a fully reticulated $Fe(TCNB)_2$ network. The network is composed of a regular arrangement of Fe atoms separated by 1.5 nm forming domains of about 30 nm in lateral extension. The networks are commensurate with the substrate lattice and exhibit organizational chirality due to the four CN groups that can interact equally with the Fe atoms. Clockwise and anticlockwise domains coexist on the surface and are separated by grain boundaries. The regular architecture of the Fe-$(TCNB)_2$ on Au(111) indicates that the network architecture is ruled by the ligand bonds. It has been reported that this network can be grown on Ag(100) and NaCl surfaces [2], further indicating that the interaction with the underlying metal surfaces seems to play only a minor role.

The electronic information is gathered from the dI/dV spectroscopic labeling with FePc to identify some of the resonances of the $Fe(TCNB)_2$ network. First of all, the position of $d_{xz/yz}$ peak at -0.79 V in both system, indicates that the Fe feels a similar environment from the TCNB ligands in the network and in the FePc molecules. Further analysis of this feature have been discussed by means of metal ligand bond formation mechanism. The main reason for the appearance of similar STS features in both systems is due to the formation a common metal organic bond between the metal atom d-orbital and ligand-orbitals. However, the FePc molecule is more complicated in the sense that two different bonding interactions covalent and coordinate bonds coexist in the same molecule. In particularly, the similar $d_{xz/yz}$ peak for both systems is a direct result of coordination bonding between the unshared pairs of electrons in the remaining two isoindole nitrogen atoms and the Fe atom in the FePc. On the contrary, the appearance of d_{z^2} orbital on the FePc and not on $Fe(TCNB)_2$ network is a results of covalent bonding in the FePc molecule. Unfortunately, the spin states of the $Fe(TCNB)_2$ network is still unclear and further studies about the magnetism of the network are necessary.

Chapter 6

Summary and perspectives

In this thesis, 2D supra molecular architectures of TCNB and Fe-TCNB at the Au(111) surface have been studied. First, the principle of self− assembling of organic molecule and organometallic complex on metal surface have been discussed. The hydrogen bond and metal organic coordination bond are the prime factor governing the the self assembly process of the TCNB and Fe-TCNB complex on Au(111) surface, respectively. Controlling the subtle interplay between the adsorbate-adsorbate and adsorbate−substrate interactions by varying the stoichiometry of the Fe atoms and TCNB ligands has led to the synthesis of variety of Fe-TCNB complexes. Second, the electronic properties of the TCNB and Fe-TCNB coordination nanostructures on Au(111) surface have been investigated with a combination of STS and DFT calculations.

The TCNB forms an ordered monolayers with a rhombic unit cell. The self-assembled structure is stabilized by the C≡N−−H−C hydrogen bond. The STS experiment confirms that the Shockley state of the Au(111) surface is shifted upwards by 87 meV due to the TCNB monolayer. Furthermore, it is found that this shift is comparably small and leads to an adsorption energy per surface area similar to that of krypton on Au(111) surface. The TCNB on Au(111) surface shows a negligible charge transfer with the Au(111) substrate and a small adsorption energy of 0.5 eV per TCNB molecules. STS measurement provide a HOMO-LUMO gap of 3 eV in agreement with DFT calculations.

The results in this thesis open perspectives for several future investigations. The self assembling of TCNB on Au(111) surface is a model system to study the interface between organic molecules and metal surface. The interface is a decisive factor for the quality of these nanoscale devices since it modifies the properties of the molecule and therefore its functionalities. Further studies extending these concept into third

dimension should provide a deeper understanding of more realistic system made of thick organic films.

Further structural complexation is achieved by the synthesis of a Fe-TCNB coordination complex. The metal organic coordination is an important strategy in supra molecular chemistry to produce more robust structures. In this study, the Fe adatoms are utilized in the fabrication of Fe-$TCNB_4$ complexes on the Au(111) surface at different substrate temperatures. At low deposition temperature, an ordered metastable intermediate forms first. STM data yield the bond angle between the Fe-N-C is 120°. The scanning tunneling spectroscopy reveals that Fe atoms localize the surface−state electrons similar to what they do on the bare Au(111) surface. This result indicates that the TCNB molecules are virtually in the same electronic state as before the Fe adsorption. Therefore, the preservation of the surface state on the TCNB as well as the apparition of a bound state on the Fe atom strongly suggest that the coordination bond between the Fe atom and the ligands has not yet formed. When the temperature is changed, to room temperature, the original entities slowly transform into the $Fe(TCNB)_4$ monomer complexes with 180° Fe-N-C bond angle. The STS above the $Fe(TCNB)_4$ complex shows new features. First of all, the LUMO-HOMO gap now is considerably reduced from 3.0 eV in the precursor system Fe-$TCNB_4$ to 2.0 eV in the $Fe(TCNB)_4$ complex. Additionally, the most striking signature of the complex formation is the appearance of a series of new resonances, at -0.5 eV and +0.7 eV. Both of these features refer to molecular orbitals with out-of-plane d-contributions, which are preferentially measured by STM. DFT calculations support the conclusions and drawn from experimental studies. The charge redistribution analysis performed after the dynamical relaxation of the free complex gives us some additional hints. Upon fourfold coordination with the TCNB ligands, -2 $|e|$ is transferred from the Fe atom to the neighboring N atoms and redistributed among all the TCNB ligands, the Fe atom thus becomes Fe^{2+}. This is confirmed by a comparative analysis of the difference in the Mulliken charges of the N atoms next neighbors of the Fe site; about -0.28 $|e|$ is transferred to each N atom.

The deposition of TCNB molecules and iron atoms in a proportions of 2:1 and post-annealing up to 450 K leads to a fully reticulated $Fe(TCNB)_2$ network. STM data confirm that the network has a square structure with a measured periodicity of $\vec{b_1} \approx \vec{b_2} = 1.15 \pm 0.1$ nm in both directions. The domain sizes are up to 30 nm in width. The electronic properties of the $Fe(TCNB)_2$ networks were investigated by STS and have been compared to those of FePc molecules. It is found that the position of the dxz/yz peak at -0.79 V of Fe is similar in both system, indicating that

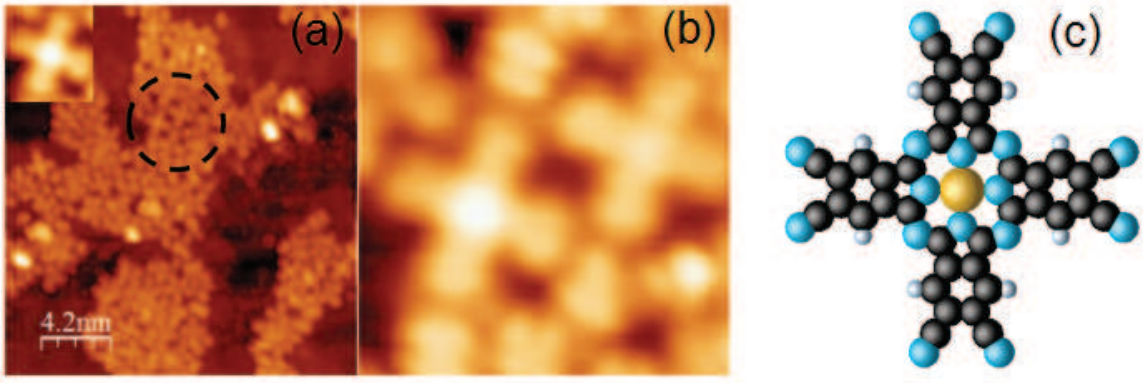

Figure 6.1: (a) STM image of full transformation of Fe-$(TCNB)_4$ monomer to the covalent bond octacyanophthalocyanine after annealing 300 °C. (b, c) high resolution images of octacyanophthalocyanine monomer and structural model.

the Fe somehow feels a similar environment from the TCNB ligands in the network and in the FePc molecule. One of the main reasons for the appearance of similar STS features in the both systems is a common metal-organic bond between the metal atom d-orbital and the ligand orbitals. However, the FePc molecules are involving more complicated bond formation mechanisms. The two different bonding (π and σ) interactions coexist in the formation of FePc. This may explain why some STS features are different in both systems.

A detailed study of the Fe-TCNB coordination structures on the Au(111) surface shows that the substrate temperature is a key parameter to induce the successful chemical reactions between the organic linker and metal atoms on metal surface. We showed that too low deposition temperature prevents the self-assembly process of the metal-organic entities which are subjected to steric hindrance due to topological confinement. In this thesis all the stable Fe-TCNB based nanostructures on Au(111) were obtained at room temperature sometimes with post annealing of the substrate up to 450 K. Further studies are necessary to extend these concepts to high annealing temperature to form real covalent bond metal-organic nanostructures on metal surface.

The initial stage of polymerization is already observed in Figure 6.1 where units of octacyanophthalocyanines, involving covalent bonds, have formed from the Fe-$(TCNB)_2$ network. Unfortunately, by further increasing the substrate temperature, most of the TCNB molecules originally coordinated to the Fe atoms desorb from the surface and are not available anymore to pursue the polymerization process. As can be shown from Figure 6.1, the Fe atoms appear as bright centers confirming the presence of d_{z^2} orbitals of the Fe close to the Fermi level while the organic linking sections

appear as four lobes. Furthermore, the fact that the mirror-symmetric, clockwise and anticlockwise chiralities have disappeared, clearly indicates the full transformation into covalent bonds. Further studies extending these concepts to polymerization of single Poly-FePc sheets should provide an interesting subject, not only from the electronic but also from the magnetic point of view [58]. The ability to control the covalent bond formation on metal surfaces offers the opportunity to prepare grids of metal atoms of potential importance for the scientific studies and technological applications. The regular array of spin centers formed by nanometer spaced magnetic atoms can serve as model systems for fundamental studies of single spin phenomena or spin-spin interactions.

Bibliography

[1] N. Abdurakhmanova, A. Floris, T. C. Tseng, A. Comissoand, S. Stepanow, A. De Vita, and K. Kern. *Nature Commun*, 3:940, 2012.

[2] M. Abel, S. Clair, O. Ourdjini, M. Mossoyan, and L. Porte. *J. Am. Chem. Soc*, 133:1205, 2011.

[3] J. Ahlund, K. Nilson, J. Schiessling, L. Kjeldgaard, S. Berner, N. M artensson, C. Puglia, B. Brena, M. Nyberg M, and Y. Luo. *J Chem Phys*, 21:34709, 206.

[4] J. Alan, Bennett, and L. M. Falicov. *Physical Review*, 151:512, 1966.

[5] C. Bach, M. Giesen, H. Ibach, and T. Einstein. *Phys. Rev. Lett*, 78:4225, 1997.

[6] J. Bardeen. *Phys. Rev. Lett*, 6:57, 1961.

[7] S. M. Barlow and R. Raval. *Surf. Sci. Rep*, 50:201, 2003.

[8] J. V. Barth. *Annu. Rev. Phys. Chem*, 58:375, 2007.

[9] J. V. Barth, J. Wecksser, C. Cai, P. Gulnter, and L. Burgi. *Angew. Chem. Int. Ed. Eng*, 39:1230, 2000.

[10] A. D. Becke. *Phys. Rev. A*, 38:3098, 1988.

[11] G. Binnig and H. Rohrer. *IBM Journal of Research and Development*, 30:4, 1986.

[12] G. Binnig and H. Rohrer. *Rev. Mod. Phys*, 71:S324, 1999.

[13] M. Bode. Spin-polarized scanning tunneling microscopy. *Rep.Prog.Phys*, 66:189, 2007.

[14] A.G. Borisov, A. K. Kazansky, and J. P. Gauyacq. *Phys. Rev. B*, 65:205414, 2002.

[15] R. Car and M. Parrinello. *Phys. Rev. Lett*, 55:2471, 1985.

[16] R. Lloyd Carroll and Christopher B.Gorman. *The genesis of molecular electronics*. Angewandte Chemie International Edition, 2002.

[17] S. Chakraborty and S. Wategaonkar. *Chem. Phys. Lett*, 460:22, 2008.

[18] L. Z. Chen, J. Miller, and M. Can. *J. Chem*, 69:2007, 1991.

[19] C. Clark, A. Hassanien, S. Khan, K. F. Braun, H. Tanaka, and S. W. Hla. *Nat. Nano*, 5:265, 2010.

[20] Feng Duan and Jin Guojin. *Condensed Matter Physics*. World Scientific, 2005.

[21] D. M. Eigler, C. P. Lutz, and W. E. Rudge. *Nature*, 352:600, 1991.

[22] R. Eliseo, C. Jordi, and A. Santiago. *Coord. Chem. Rev*, 249:2660, 2005.

[23] J. Repp et al. *Science*, 312:1196, 2006.

[24] S.W. Hla et al. *Phys. Rev. Lett*, 85:2777, 2000.

[25] M. N. Faraggi, N. Jiang, N. L. Gonzalez, A. Langner, S. Stepanow, and K. Kern. *J. Phys. Chem.C*, 116:24558, 2012.

[26] R. Feenstra, J. A. Stroscio, and A. Fein. *Surface Science*, 181:295, 1987.

[27] I. Ferain, C. A. Colinge, and J. P. Colinge. *Nature*, 479:316, 2011.

[28] I. Fernàndez-Torrente, K. J. Franke, and J. I. Pascual. *Phys. Rev. Lett.*, 101:217203, 2008.

[29] I. Fernàndez-Torrente, D. Kreikemeyer-Lorenzo, A. Strzecka, K. J .Franke, and J . I . Pascual. *Phys. Rev. Lett.*, 108:036801, 2012.

[30] V. Ferretti, L. Pretto, M.A. Tabrizi, and P. Gilli. *Acta Crystallogr. B*, 62:634, 2006.

[31] R. P. Feynman. *Eng. Sci*, 23:2236, 1960.

[32] Richard Feynman. *There's Plenty of Room at the Bottom*, 1959). `http://en.wikipedia.org/wiki/There's_Plenty_of_Room_at_the_Bottom`.

[33] G. Frenking and N. Fröhlich. *Chemical Reviews*, 100:774, 2000.

[34] M. Fuechsle, J. A. Miwa, S. Mahapatra, H. Ryu, S. Lee, O. Warschkow, L. C. Hollenberg, G. Klimeck, and M. Y. Simmons. *Nat. Nano*, 7:246, 2012.

[35] P. Gambardella, S. Stepanow, A. Dmitriev, J. Honolka, M. F. de Groot. Frank, Magalí Lingenfelder, S. Sen Gupta, D. D. Sarma, P. Bencok, S. Stanescu, S. Pons S. Clair, N. Lin, A. P. Seitsonen, H. Brune, J. V. Barth, and K. Kern. *Nature Materials*, 8:189, 2009.

[36] L. Gao, W. Ji, Y. B. Hu, Z. H. Cheng, Z. T. Deng, Q. Liu, N. Jiang, X. Lin, W. Guo, S. X. Du, W. A. Hofer, X. C. Xie, and H.-J. Gao. *Phys. Rev. Lett*, 99:106402, 2007.

[37] K. Giesen, F. Hage, F. J. Himpsel, H. J. Riess, and W. Steinmann. *Phys. Rev. Lett*, 55:300, 1985.

[38] S. Goedecker, M. Teter, and J. Hutter. *Phys. Rev. B*, 54:1703, 1996.

[39] N. Gonzalez-Lakunza, I. Fernandez-Torrente, K.J. Franke, N. Lorente, A. Arnau, and J.I. Pascual. *Phys. Rev. Lett*, 100:156805, 2008.

[40] G. Gopakumar, N. Nëel, J. Kröger, and R. Berndt. *J. Phys. Chem. Lett*, 484:59, 2009.

[41] N. N. Greenwood and A. Earnshaw. *Chemistry of the elements*. Pergamon Press, Oxford Oxfordshire, 1984.

[42] S. Grimme. *J. Comput. Chem*, 25:1463, 2004.

[43] G.Sidney, Davison, and Maria Steslicka. *Basic Theory of Surface States*. 1992.

[44] Y. Hammer, Morikawa, and J. K. Nϕrskov. *Phys. Rev. Lett*, 76:2141, 1996.

[45] P. K. Hansma and J. Tersoff. *Journal of Applied Physics*, 61:R1, 1987.

[46] B. W. Heinrich, C. Iacovita, Th. Brumme, D.-J. Choi, L. Limot, M. V. Rastei, W.A. Hofer, J. Kortus, and J.P. Bucher. *J. Phys. Chem. Lett*, 1:1517, 2010.

[47] B. W. Heinrich, L. Limot, M. V. Rastei, C. Iacovita, J. P. Bucher, D. M. Djimbi, C. Massobrio, and M. Boero. *Phys. Rev. Lett*, 107:216801, 2011.

[48] B.W. Heinrich. *Tunneling spectroscopy of nanoscale objects: from metallic islands to single atoms and molecules*. PhD thesis, University of Strasbourg, 2010.

[49] S. W. Hla, K. F. Braun, V. Iancu, and A. Deshpande. *Nano Lett*, 6:1997, 2004.

[50] D. E. Hooks, T. Fritz, and M. D. Ward. *Adv. Mater*, 13:227, 2001.

[51] A. Hotzel, G. Moos, K. Ishioka, M. Wolf, and G. Ertl. *Applied Physics B*, 68:615, 1999.

[52] C. Hückstadt, S. Schmidt, and S. Hüfner. *Phys. Rev. B*, 73:075409, 2006.

[53] B. Hummer and J. K. Nϕrskov. *Advances in Catalysis*, 45:129, 2000.

[54] M. Emi i, T. Noriyuki, M. Daisuke, K. Yousoo, T. Noriaki, and K. Maki. *Phys. Rev. Lett*, 109:086602, 2012.

[55] C. Iacovita, M.V. Rastei, B.W. Heinrich, T. Brumme, J. Kortus, L. Limot, and J.P. Bucher. *Phys. Rev. Lett*, 101:116602, 2008.

[56] F. T. Isabel, J. K. Katharina, and I. P. Jose. *International Journal of Mass Spectrometry*, 277:273, 2008.

[57] T. Ito and S. Okazaki. *Nature*, 406:1031, 2000.

[58] Z. Jian and S. Qiang. *J. Am. Chem. Soc*, 133:15119, 2011.

[59] K. Kanai, K. Akaike, K. Koyasu, K. Sakai, T. Nishi, Y. Kamizuru, T. Nishi, Y. Ouch, and K. Seki. *Appl Phys A*, 95:313, 2009.

[60] S. D. Kevan. *Phys. Rev. Lett*, 50:526, 1983.

[61] J. Kliewer and R. Berndt. *Phys. Rev. Lett*, 85:4939, 2000.

[62] J. Kliewer, R. Berndt, E. V. Chulkov, V. M. Silkin, P. M. Echenique, and S. Crampin. *science*, 288:5470, 1993.

[63] J. Kliewer, R. Berndt, and S. Crampin. *Phys. Rev. Lett*, 85:4936, 2000.

[64] W. Kohn and L. J. Sham. *Phys. Rev*, 140:A1133, 1965.

[65] J. B. Kortright, D. MLincoln, R. S. Edelstein, and A. J. Epstein. *Phys. Rev. Lett*, 100:257204, 2008.

[66] A. Kühnle. *Science*, 14:157, 2009.

[67] Angelika Kühnle. *Science*, 14:157, 2009.

[68] A. Langner, S. L. Tait, N. Lin, C. Rajadurai, M. Ruben, and K. Kern. *Proc. Natl. Acad. Sci. U. S. A.*, 104:17927, 2007.

[69] C. Lee, W. Yang, and R. G. Parr. *Phys. Rev. B*, 37:785, 1988.

[70] L. Limot, J. Kröger, R. Berndt, A. Garcia-Lekue, and W.A. Hofer. *Phys. Rev. Lett*, 94:126102, 2005.

[71] L. Limot, E. Pehlke, J. Kröger, and R. Berndt. *Phys. Rev. Lett*, 94:036805, 2005.

[72] X. Lu and K. W. Hipps. *J. Phys. Chem. B*, 101:5390, 1997.

[73] X. Lu and K. W. Hipps. *J. Phys. Chem. B*, 101:5396, 1997.

[74] V. Madhavan, W. Chen, T. Jamneala, and M. F. Crommie. *Phys. Rev. B*, 64:165412, 2001.

[75] J. M. Manriquez, G. T. Yee, R. Scott Mclean, A. J. Epstein, and J. S. Miller. *Science*, 252:1415, 1991.

[76] G. B. Maria, G. Pierluigi Gargiani, F. Riccardo, B. Roberto, C. Albano, V. Alberto, F. Luca, and M. Carlo. *J. Phys. Chem. C*, 114:21644, 2010.

[77] N. Marisa, Faraggi, J. Nan, G. L. Nora, L.Alexander, S. Stepanow, K. Kern, and A. Arnau. Bonding and charge transfer in metalorganic coordination networks on au(111) with strong acceptor molecules. *J. Phys. Chem C*, 116:24565, 2012.

[78] S. Mathieu, L. Philippe, D. F. Steven, A. M. Mohamed, D. S. Frans, H. Oliver, and L. Roberto. *J. Phys. Chem. B*, 110:7898, 2006.

[79] J. Ménde, R. Caillard, G. Otero, N. Nicoara, and J.A. Martín-Gago. *Adv. Mater*, 18:2048, 2006.

[80] G. Meyer, S. Zophel, and K. H. Rieder. *Phys. Rev. Lett*, 77:2113, 1996.

[81] N. Mills. *J. Am. Chem. Soc*, 128:13649, 2006.

[82] K. Morgenstern, K.F. Braun, and K.H. Rieder. *Phys. Rev. Lett*, 89:226801, 2002.

[83] A. Mugarza, R. Robles, C. Krull, R. Korytar, N. Lorente, and P. Gambardella. *Phys. Rev. B*, 85:155437, 2012.

[84] N.Abdurakhmanova, T-C. Tseng, A. Langner, C. S. Kley, V. Sessi, S. Stepanow, and K. Kern. *Phys. Rev. Lett*, 110:027202, 2013.

[85] A. Nilsson, L-G. M. Petterson, B. Hammer, T. Bligaard, C. H. Christensen, and J. K. Nϕrskov. *Catal. Lett*, 100:111, 2005.

[86] J. K. Nϕrskov. *Phys. Rev. B*, 26:2875, 1982.

[87] F. E. Olsson, M. Persson, A. G. Borisov, J.-P. Gauyacq, J. Lagoute, and S. Fölsch. *Phys. Rev. Lett*, 93:206803, 2004.

[88] Werner Hofer Peter Grtter and Federico Rosei. *Properties of single organic molecules on crystal surfaces*. Imperial College Press ; Distributed by World Scientific, London Singapore ; Hackensack,, 2006.

[89] Nobel Prize. *Press release for the 1986 Nobel Prize in physics*, 1986). `http://www.nobelprize.org/nobel_prizes/physics/laureates/1986/press.html`.

[90] K. Kabir R. Jain, J. B. Gilroyand K. A. R. Mitchell, K-C Wong, and Robin G. Hicks. *Nature*, 445:291, 2007.

[91] F. Reinert, G. Nicolay, S. Schmith, D. Ehm, and W. Shen. *Phys. Rev. B*, 63:115415, 1990.

[92] J. Repp, G. Meyer, and K. Hiieder. *Phys. Rev. Lett*, 92:036803, 2004.

[93] G. Robert and W. S. Lynn W. *J. Chem. Phys*, 38:1613, 1963.

[94] F. Roth, A. König, R. Kraus, M. Grobosch, T. Kroll, and M. Knupfera. *Eur. Phys. J. B*, 74:344, 2010.

[95] S. Rousset, V. Repain, G. Baudot, Y. Garreau, and J. Lecoeur. *Journal of Physics: Condensed matter*, 15:S3363, 2003.

[96] R.Temirov, S. Soubatch, A. Luican, and F. S. Tautz. *Nature*, 444:350, 2006.

[97] Harikumap. S. *Electrochemical studies on metal phthalocyanines*. Doctoral Thesis, department of applied chimistry cochin university of science and technology cochin - 682022.

[98] W. R. Salanek and S. Stafstromand J. L. Bredas. *Conjugated Polymer Surfaces and Interfaces: Electronic and Chemical Structure of Interfaces for Polymer LEDs*. Cambridge University Press, 1996.

[99] A. Sareh, M. N. Shariati, Y. Shun, and G. Mats. *J. Chem. Phys*, 137:084705, 2012.

[100] A. M. Schaffer, M. Gouterman, and E. R. Davidson. *Theoret. Chim. Acta*, 30:9, 1973.

[101] Schläfer and G. H. L.; Gliemann. *Basic Principles of Ligand Field Theory*. Wiley Interscience, 1969.

[102] U. Schlickum, R. Decker, F. Klappenberger, G. Zoppellaro, S. Klyatskaya, M. Ruben, I. Silanes, A. Arnau, K. Kern, H. Brune, and J. V. Barth. Metalorganic honeycomb nanomeshes with tunable cavity size. *Nano Letter*, 7:3813–3817, 2007.

[103] W. Schockley. *Phys. Rev. Lett*, 56:317, 1939.

[104] X. C. Shi, C. Lin, C. Minot, T. C. Tseng.and S. L. Tait, N. Lin, R. Q.Zhang, K.Kern, J. I.Cerda, and M. A.Van Hove. Structural analysis and electronic properties of negatively charged tcnq: 2d networks of (tcnq)2mn assembled on cu(100). *J. Phys. Chem C*, 114:17197, 2010.

[105] X. Q. Shi, C. S. Lin, C. Minot, Tzu-Chun Tseng, Steven L. Tait, N. Lin, R. Q. Zhang, Kl. Kern, O J. I. Cerdá, and M. A. Van Hove. *J. Phys. Chem. C*, 114:17204, 2010.

[106] B. Simon. *Ann. Phys. (N.Y.)*, 97:279, 1976.

[107] N. V. Smith. *Phys. Rev. B*, 32:3549, 1985.

[108] H. Song, Y. Kim, Y. H. Jang, H. Jeong, M. A. Reed, and T. Lee. *Nature*, 462:1043, 2009.

[109] S.R.Forrest. *Nature*, 428:911, 2004.

[110] S. Stepanow, N. Lin, D. Payer, U. Schlickum, F. Klappenberger, G. Zoppellaro, M. Ruben, H. Brune, J. V. Barth, and K. Kern. *Angew. Chem., Int. Ed*, 46:713, 2007.

[111] S. Stepanow, N. Lin, D. Payerand U. Schlickum, F. Klappenberger, G. Zoppellaro, M. Ruben, H. Brune, J. V. Barth, and K. Kern. *Angewandte Chemie-International Edition,*, 46:710, 2007.

[112] J. A. Stroscio and D. M. Eigler. *Science*, 254:1319, 1991.

[113] R. Taube. *Pure App Chem*, 38:438, 1974.

[114] J. Tersoff and D. R. Hamann. *Phys. Rev. Lett*, 50:1998, 1983.

[115] J. Tersoff and D. R. Hamann. *Phys. Rev. B*, 31:805, 1985.

[116] N. Troullier and J. L. Martins. *Phys. Rev. B*, 43:1993, 1991.

[117] T. C. Tseng, N. Abdurakhmanova, S. Stepanow, and K. Kern. Hierarchical assembly and reticulation of two-dimensional mn and ni tcnqx (x = 1,2,4) coordination structures on a metal surface. *J. Phys. Chem C*, 115:10211, 2011.

[118] T. C. Tseng, Ch. Lin, X. Shi, S. L. Tait, X. Liu, U. Starke, N. Lin, R. Zhang, Ch. Minot, M. A. Van Hove, and et al. Two dimensional metalorganic coordination networks of mn-7,7,8,8- tetracyanoquinodimethane assembled on cu(100): Structural, electronic, and magnetic properties. *Phys. Rev. B*, 80:155458, 2009.

[119] N. Tsukahara, S. Shiraki, S. Itou, N. Ohta, N. Takagi, and M. Kawai. *Phys.Rev.Letter*, 106:187201, 2011.

[120] T. R. Umbach, I. Fernandez-Torrente, J. N. Ladenthin, J. I. Pascual, and K. J. Franke. *J. Phys.: Condens. Matter*, 20:354003, 2012.

[121] J. H. Van Vleck. Theory of the variations in paramagnetic anisotropy among different salts of the iron group. *Phys. Rev*, 41:215, 1932.

[122] B. Wang. *Electronic structure of monolayer graphene and biomimetic molecules on metal surfaces*. Doctoral Thesis, Ecole normale suprieure de Lyon, 2010.

[123] W. Wang, X. Shi, S. Wang, J. Liu, M. A. Van Hove, P. N. Liu, R. Q. Zhang, and N.Lin. *Phys. Rev. Lett*, 110:046802, 2013.

[124] D. Wegner, R. Yamachika, Y. Wang, W. B. Victor, M. B. Bar, R. L. Jeffrey, and M. F. Crommie. *Nano Lett*, 8:135, 2008.

[125] G. M. Whitesides, J. P. Mathias, and C. T. Seto. *science*, 254:1312, 1991.

[126] M. Yu, W. Xu, N. Kalashnyk, Y. Benjalal, S. Nagarajan, F. Masini, E. Lgsgaard, M. Hliwa, X. Bouju, A. Gourdon, C. Joachim, F. Besenbacher, and T. R. Linderoth. *Nano Research*, 8:189, 2009.

[127] J. Ziroff, P. Gold, A. Bendounan, F. Forster, and F. Reinert. *Surf. Sci*, 603:354, 2009.